Distribution Agreement

In presenting this thesis as a partial fulfillment of the requirements for a degree from Emory University, I hereby grant to Emory University and its agents the non-exclusive license to archive, make accessible, and display my thesis in whole or in part in all forms of media, now or hereafter now, including display on the World Wide Web. I understand that I may select some access restrictions as part of the online submission of this thesis. I retain all ownership rights to the copyright of the thesis. I also retain the right to use in future works (such as articles or books) all or part of this thesis.

Justin Bier   April 7, 2020

Discovery of Substructure in Nearby Reverberation-Mapped Active Disk Galaxies with *DiskFit*

by

Justin Bier

Dr. Merida Batiste and Dr. Alissa Bans
Advisers

Department of Physics

Dr. Merida Batiste

Adviser

Dr. Alissa Bans

Adviser

Dr. Erin Bonning

Committee Member

Dr. Gary Waters

Committee Member

2020

Discovery of Substructure in Nearby Reverberation-Mapped Active Disk Galaxies with *DiskFit*

By

Justin Bier

Dr. Merida Batiste and Dr. Alissa Bans

Advisers

An abstract of
a thesis submitted to the Faculty of Emory College of Arts and Sciences
of Emory University in partial fulfillment
of the requirements of the degree of
Bachelor of Science with Honors

Department of Physics

2020

Abstract

Discovery of Substructure in Nearby Reverberation-Mapped Active Disk Galaxies with *DiskFit*
By Justin Bier

We use the kinematic and photometric modeling algorithm *DiskFit* for a sample of three nearby active disk galaxies with well determined M_{BH} estimates via reverberation mapping. We use spatially resolved velocity maps from Integral Field Spectroscopy (IFS) in conjunction with high resolution photometry to identify and determine quantitative estimates of the geometry and strength of distinct morphological components. This research aims to use both branches of *DiskFit* modeling to gain insight into the kinematics of our sample galaxies and analyze the contribution from each distinct component using trends with the first four Gauss-Hermite moments for the line-of-sight velocity distribution. Future work will attempt to isolate the kinematics of the bulge for calibration of the M_{BH}-σ_* relationship, which is foundational to reverberation mapping, and to understand the effects of morphological components on bulge stellar velocity dispersion, σ_*. In this paper we present kinematic models consisting of disk, bar, and radial flow components (K-D-B-RF) for NGC 3516, NGC 4151, and NGC 5548. We show the presence of distinct disk, bar, and bulge components (P-D-B-Blg) well represented by photometric *DiskFit* models for NGC 3516. We confirm the presence of a barlens in NGC 4151, first suggested by observations, from comparison of the *DiskFit* bar component kinematics and simulations at similar nearly face-on inclinations. However, we show inaccuracies in the photometric models for NGC 4151 stemming from the weak bar and a known degeneracy occurring when the position angle of the bar is within ~10° of either the major or minor axis of the disk component. We find non-circular motion within NGC 5548 likely attributed to the aftermath of a major merger event.

Discovery of Substructure in Nearby Reverberation-Mapped Active Disk Galaxies with *DiskFit*

By

Justin Bier

Dr. Merida Batiste and Dr. Alissa Bans

Advisers

A thesis submitted to the Faculty of Emory College of Arts and Sciences
of Emory University in partial fulfillment
of the requirements of the degree of
Bachelor of Science with Honors

Department of Physics

2020

Acknowledgements

I am deeply grateful for the support, knowledge, and inspiration from Dr. Merida Batiste, much needed throughout completion of this project. I too, would like to extend my gratitude to Dr. Alissa Bans, Dr. Erin Bonning, and Dr. Garrett Waters for being excellent professors and continuing to assist my journey through college and life. I am appreciative of the Emory College Honors Program for facilitating this endeavor. I am forever indebted to my family and friends for their continuous motivation, love, and laughter.

Table of Contents

Tables and Figures

1. Introduction

Extensive research conducted in recent decades aims to unravel the mysteries surrounding black holes, and to assess their correlation with the nature of the evolving universe. Observations of the elliptical orbits of stars and gas within the central region of the Milky Way galaxy indicate an enormous, and incredibly compact, central mass. The only explanation for this enormous compact mass is a supermassive black hole on the order of one million solar masses (Reid & Brunthaler 2004). Recently, the existence of supermassive black holes has been confirmed through direct imaging of the event horizon of the supermassive black hole (SMBH) of M87 (Event Horizon Telescope Collaboration et al. 2019). See Table A1 for a list of all abbreviations employed throughout this paper. Other studies indicate most galaxies, if not all, contain a SMBH at its center (Ferrarese & Ford 2005). Thus, it is believed that the nature of galaxies and their SMBH are tied together and relate heavily to their shared evolution. An active galaxy, as opposed to a quiescent galaxy, contains an incredibly luminous central region caused by an accretion disk of infalling material into the actively feeding SMBH. The tremendous luminosities of active galaxies are attributed to matter releasing light as it quickly loses potential energy falling into the SMBH event horizon (Fanidakis et al. 2011). Active galaxies contain an active galactic nucleus (AGN) displaying tremendous luminosities and significant flux variations (Bentz 2016; Fanidakis et al. 2011). It is currently thought that the AGN represents a particular stage of the evolution of a galaxy (Fanidakis et al. 2011; Heckman & Best 2015). The symbiosis of the SMBH and its host galaxy is exemplified by numerous, well researched (Bentz & Manne-Nicholas 2018; Bentz & Denney 2013), scaling relationships between the mass of the SMBH, or M_{BH}, and physical properties of the host galaxy. The tightest observed correlation is between

M_{BH} and the stellar velocity dispersion of the bulge component, σ_*, known as the M_{BH}-σ_* relationship (Bentz & Manne-Nicholas 2018).

To accurately calculate the relationship between properties of the galaxy and M_{BH}, obtaining the best evaluation for M_{BH} from independent methods is crucial. The most common method for determining M_{BH} is stellar, or gas, dynamical modeling; this method maps the trajectory of stars, or gas, within the SMBH gravitational sphere of influence and uses Kepler's law of planetary motion to deduce M_{BH} (Onken et al. 2014; Reid & Brunthaler 2004). Stellar and gas dynamical modeling is, in almost all cases, limited to quiescent galaxies for two reasons: due to the incredibly bright AGN obscuring the motion of matter and secondly quiescent galaxies are much more abundant than AGN in the universe, meaning there are far fewer AGN close enough to resolve the SMBH sphere of influence than quiescent galaxies. This type of dynamical modeling requires incredibly high spatial resolution, in order to resolve the gravitational sphere of influence of the SMBH, and thus is limited to galaxies in the local universe.

As opposed to quiescent galaxies, we can exploit the flux variability of broad line AGN to determine M_{BH} through reverberation mapping (Bentz 2016). Flux variations originate in the accretion disk and are followed by corresponding flux variations in the broad line region (referred to as reverberations or echoes), which can be used to determine the radius of the broad line region. Reverberation mapping determines M_{BH} from the Virial Theorem, an association between the geometry of the broad line region, the width of the broad lines, and the gravitational constant. It is increasingly difficult to observe quiescent galaxies over increasing cosmological distances, corresponding to younger universe, and accordingly the majority of observed distant galaxies are AGN host galaxies. While dynamical modeling is limited by spatial resolution, reverberation mapping requires long observation time to discover corresponding flux variations

and is thus limited by available observation time. However, reverberation mapping can theoretically be applied to AGN at any distance because it does not require spatial resolution. Calculations of M_{BH} from reverberation mapping require a dimensionless scale factor f to account for the unknown nature and geometry of the broad line region. Accurate determination of the M_{BH}-σ_* relationship is imperative to reverberation mapping, since it is typically impossible to deduce f observationally. Instead, the scale factor f is calculated by the offset needed for active and quiescent galaxies to follow the same M_{BH}-σ_* trend (Batiste et al. 2017).

Since the M_{BH}-σ_* relationship is fundamental to the scaling of all M_{BH} obtained through reverberation mapping, it is clear this relationship needs to be more tightly constrained. As M_{BH} measurements from both dynamical modeling and reverberation mapping have been improved, Batiste et al. (2017), hereafter Ba17b, explains the necessity to also improve velocity dispersion measurements. It is therefore necessary to determine what defines σ_* and what phenomena can affect measured σ_*. Ba17b discuss the tremendous discrepancies in the radius in which σ_* is measured; bulge effective radius r_e (the radius containing one half of the total light from the bulge), $r_e / 8$, and even the half-light radius of the whole galaxy are all used across literature. Since σ_* is the measured stellar velocity dispersion in the bulge, measurements of r_e will significantly affect the values of σ_* produced (Ba17b). Additionally, there is no accepted best method for measuring σ_*; even the position angle used in long-slit spectroscopy causes measurement error in σ_* measured values (see Ba17b and references within). Other observations show galactic morphologic components playing a role in the pattern of velocity dispersion across the galaxy or trends innate to either quiescent or AGN host galaxies (Barbosa et al. 2006). In summary, neither r_e or σ_* are consistently measured or presented in literature.

The importance of accounting for the effects of morphologically distinct components, such as spiral arms, bar, or disk, on σ_* is highlighted when noting that roughly two thirds of spiral galaxies contain a bar component (Holmes et al. 2015; Iannuzzi & Athanassoula 2015). Of these, nearly 30% contain strong photometric bars, an additional 20% include weak bars within the visual light spectrum. The remaining barred galaxies have bars observed in NIR images which are photometrically undetectable in the visible, due to obscuring dust (Holmes et al. 2015). Bars cause deviations from normal circular rotation and have the capability of redistributing matter and angular momentum into other galactic components, including the bulge and disk (Díaz-García et al. 2016). Observations and simulations show that bars lengthen and gain strength over time, while decreasing in rotational speed (Díaz-García et al. 2016). As galaxies evolve over time, the bulge and bar components therefore change symbiotically. This confirms the need to account for the effect of morphological features on the M_{BH}-σ_* relationship.

The inability to detect a bar with visible light in some galaxies motivates a detailed study into the kinematic effects of galaxy substructure. Rather than searching for a bar photometrically, kinematic analysis of galaxy motion may reveal deviations from axisymmetric rotation, or normal disk circular rotation, in the galaxy plane (Spekkens & Sellwood 2007). Integral Field Spectroscopy, or IFS, uses a spectrometer containing multiple components, or fibers, allowing us to spatially resolve various areas of the galaxy viewed on the sky, from spectra produced by each fiber. The kinematics are determined from each spectrum by fitting the line-of-sight velocity distribution as a Gauss-Hermite series (Marel & Franx 1993). The first four Gauss-Hermite moments produced from kinematic analysis represent recessional velocity V, velocity dispersion σ, asymmetric skew h_3, and symmetric skew h_4, respectively. IFS allows us to quantify non-circular motion and other features derived from the four Gauss-Hermite moments and also

represent the shape and strengths of morphological components graphically. As bright AGN typically obscures direct observation of the morphology of its host galaxy, IFS is free of photometric contamination and proves quite for viewing structure within active galaxies (Barbosa et al. 2006).

The goal of this project is to create models based on kinematics and photometry of low-inclination AGN disk galaxies, specifically well-studied galaxies with well constrained M_{BH} estimates, in order to decompose and analyze distinct structure. Furthermore, this project aims to investigate the effect of morphological components on observed line-of-sight kinematics, particularly within the bulge region. Photometric models will decompose the galaxy structure and deliver quantitative estimates for the parameters associated with each component. The use of kinematic models will indicate the existence of a bar or non-circular motions, even for weak bars or bars only visible in the near infrared which can be undetected or poorly fit in photometric modeling. Modeling both kinematics and photometry will therefore provide a more robust understanding of the underlying structure of each galaxy.

There are several popular modeling algorithms used in literature able to produce either kinematic or photometric galaxy models. *Galfit*[1] is one of the most widely used photometric modeling algorithm and *Rotcur*[2] for kinematics. *Galfit* uses a parametric algorithm to decompose the photometry into complex models which can include a disk, bar, bulge as well as spiral arm and ring structures. *Galfit* can account for an AGN by fitting a point spread function to match the AGN emission (Bentz et al. 2009; Lewis & Spekkens 2018). *Rotcur* is another parametric algorithm that fits concentric rings to kinematic velocity fields to quantify non-circular motions

---

[1] Peng, Chien. 2020. "Galfit Home Page." Accessed March 6.
https://users.obs.carnegiescience.edu/peng/work/galfit/galfit.html.

[2] Begeman, K. G. 1987. "HI Rotation Curves of Spiral Galaxies." *Ph.D. thesis, Kapteyn Institute*.

(Spekkens & Sellwood 2007). *Galfit* and *Rotcur* fundamentally model different types of data, that may or may not physically correspond, and implement different minimization algorithms so it is not immediately clear how well results from the two algorithms, for the same galaxy, can be directly compared.

For this research, we utilize a newer algorithm called *DiskFit*[3] for its ability to model both kinematic and photometric data. Although the modeling is not done simultaneously, the same minimization algorithm is employed for both modeling types (Barnes & Sellwood 2003). In contrast to *Galfit* and *Rotcur*, *DiskFit* is a non-parametric minimization algorithm, allowing a theoretically infinite number of input parameters (Reese et al. 2007); it is considered superior to *Galfit* since its non-parametric approach finds light profiles independent of specified functional forms, and superior to *Rotcur* as *DiskFit* fits a single model to the whole velocity map rather than individual tilted rings (Kuzio De Naray et al. 2012). Additionally, *DiskFit* differs from other models by providing realistic uncertainties for the modeled parameters (Sellwood & Spekkens 2015). As a versatile program, *DiskFit* can be applied to galaxies of any morphology, it can be used for AGN or quiescent galaxies, and is reliable at disk inclinations ranging from ~10° to ~80°, where 0° and 90° inclination represents the face-on and edge-on galaxy viewing profiles respectively (Peters & Kuzio De Naray 2017; Riffel et al. 2017). The use of *DiskFit* is ideal for modeling galaxy substructure because it uses the same flexible, non-parametric minimization algorithm for both photometry and kinematics.

This research aims to utilize *DiskFit* and compare output values from kinematics and photometry to each other and results from literature. We want to know how *DiskFit* photometric modeling results compares to *Galfit* models for the same galaxy. The consistency between

---

[3] "A Code for Modeling Asymmetries in Disk Galaxies." 2019. *DiskFit*. Queen's University. Accessed June 3. https://www.physics.queensu.ca/Astro/people/Kristine_Spekkens/diskfit/.

kinematic and photometric results will be an important test. This project will search for kinematically distinct substructure within AGN host galaxies with the eventual goal of isolating the kinematics of the bulge component, which has been shown above to be essential for constraining the M_{BH}-σ_* relationship and used in reverberation mapping. Finally, we want to see what information *DiskFit* can provide about the structure and properties of the non-axisymmetric motions and how, or if, the presence of a bar or bar-like flow correlates to structure in σ_* maps.

Section 2 describes the disk galaxy sample modeled with *DiskFit*. Section 3 analyzes the quality of the input data used and Section 4 discusses the specific abilities of *DiskFit* and outlines the modeling process used. Section 5 presents the results from kinematic and photometric *DiskFit* models and determines the best-fit model, while Section 6 analyzes the trends and reliability of the results. Section 7 summarizes the major conclusions of the work found in this project. Section 8 shows the work that should be done in the future to further calibrate the M_{BH}-σ_* relationship and determine its dependency on galaxy morphology.

2. Sample

The sample for this research was chosen from a set of galaxies with published velocity maps and σ_* estimates from Batiste et al. (2017). We note this paper was published earlier in the year than Ba17b, and thus denote the paper presenting σ_* estimates as Ba17a. Our sample contain all nearly face-on active galaxies with well constrained M_{BH} measurements from reverberation mapping. To produce the most robust models, this research aims for high spatial resolution and a large number of data points for both kinematic and photometric modeling types. As such, we selected galaxies from Ba17a that achieved sufficient signal to noise ratios in most of the available fibers. Three galaxies were selected for their range in morphological classifications. We wanted diverse structural complexities to test the limits of the *DiskFit*

modeling capability using one galaxy with simple apparent morphology, one with visibly more complex structure, and lastly one galaxy we expect to have very complex structure due to evidence of recent interactions. The best candidates for examination were NGC 3516 (simple), NGC 4151 (intermediate), and NGC 5548 (advanced); see Table 1 for a description of the sample characteristics obtained from the NASA/IPAC Extragalactic Database[4] (NED). The galaxies will be presented in order of increasing morphological complexity throughout this paper to illuminate some limitations of *DiskFit*.

Images of NGC 3516 (see Figure 1) show it is a lenticular galaxy with an obvious disk, bar, and bulge components and distinct spiral structure (Arribas et al. 1997; Cherepashchuk et al. 2010). Its classification, given in Table 1, denotes a ring structure (R), S-shaped spiral arms (s), and in transition between early and late type lenticular (0^0) (Vaucouleurs 1963).

NGC 4151 (see Figure 2) immediately appears more complicated, with a large pseudo-ring outer structure (R'). It has two faint spiral arms that stem from either end of the bar, and a clear bulge component (Mundell et al. 1999). The classification of NGC 4151, given in Table 1, indicates a "mixed", or photometrically weak, bar (AB), mixed spiral arms (rs) and a moderate sized bulge (Vaucouleurs 1963). Furthermore, the bar of NGC 4151 may be a 'barlens' which is a thick oval-like bar structure (Onken et al. 2014).

NGC 5548 (see Figure 3) contains a visible disk and bulge component but also has two tidal components providing strong evidence of a recent gravitational interaction (Li et al. 2016). This galaxy contains pseudo-rings (R'), is unbarred (A), and lenticular (S0), with S-shaped spiral arms (s), but in transition from S0 to Sa (denoted by 0/a) (Vaucouleurs 1963). The disk component has rings or ripples, providing strong evidence of a major merger event hypothesized

---

[4] "NASA/IPAC Extragalactic Database." 2020. NASA/IPAC. Accessed March 6.
    https://ned.ipac.caltech.edu/.

Sample Characteristics				
Galaxy	z	Classification	V_{sys}	Diameter (")
NGC 3516	0.00884	(R)SB(s)0^0	2648.967 ± 6.895	126
NGC 4151	0.00332	(R')SAB(rs)ab	995.011 ± 2.998	420
NGC 5548	0.01717	(R')SA(s)0/a	5148.936 ± 6.895	108

Table 1: Characteristics of the sample galaxies obtained from NED. Values are shown for galaxies at a redshift z, traveling away from Earth with a systematic recessional velocity V_{sys} (NED/IPAC 2019).

to be on the order of one billion years ago. Simulations of the evolution of galaxies containing a binary SMBH system suggest NGC 5548 hosts a pair of SMBH as a result of this violent merger (Li et al. 2016).

These three galaxies have been extensively studied, (see citations above and results drawn from literature in Section 6.3) (Arribas et al. 1997; Bentz et al. 2009; Li et al. 2016; Mundell et al. 1999; Onken et al. 2014; Riffel et al. 2017; and more) providing an assessment for the models produced by *DiskFit*. Furthermore, these galaxies have all been photometrically analyzed with *Galfit*, which is used as an additional evaluation for *DiskFit*'s performance and provide initial estimates parameters associated with each morphological component (Bentz et al. 2009).

3. Data

Kinematic data are available for all three galaxies in the sample in Ba17a. Photometric images for NGC 3516 and NGC 4151, from the Hubble Space Telescope (HST), were presented by Bentz et al. (2009), hereafter Be09. No photometric image of NGC 5548 was used for this research.

3.1 Kinematic Data

Spectroscopic data for NGC 3516, NGC 4151, and NGC 5548 are presented in Figures 1 and 2 of Ba17a. Data were obtained using the HexPak Integral-Field Unit (IFU) in April 2015 on the WIYN 3.5m telescope at the Kitt Peak National Observatory. Figure 4 contains a map of the
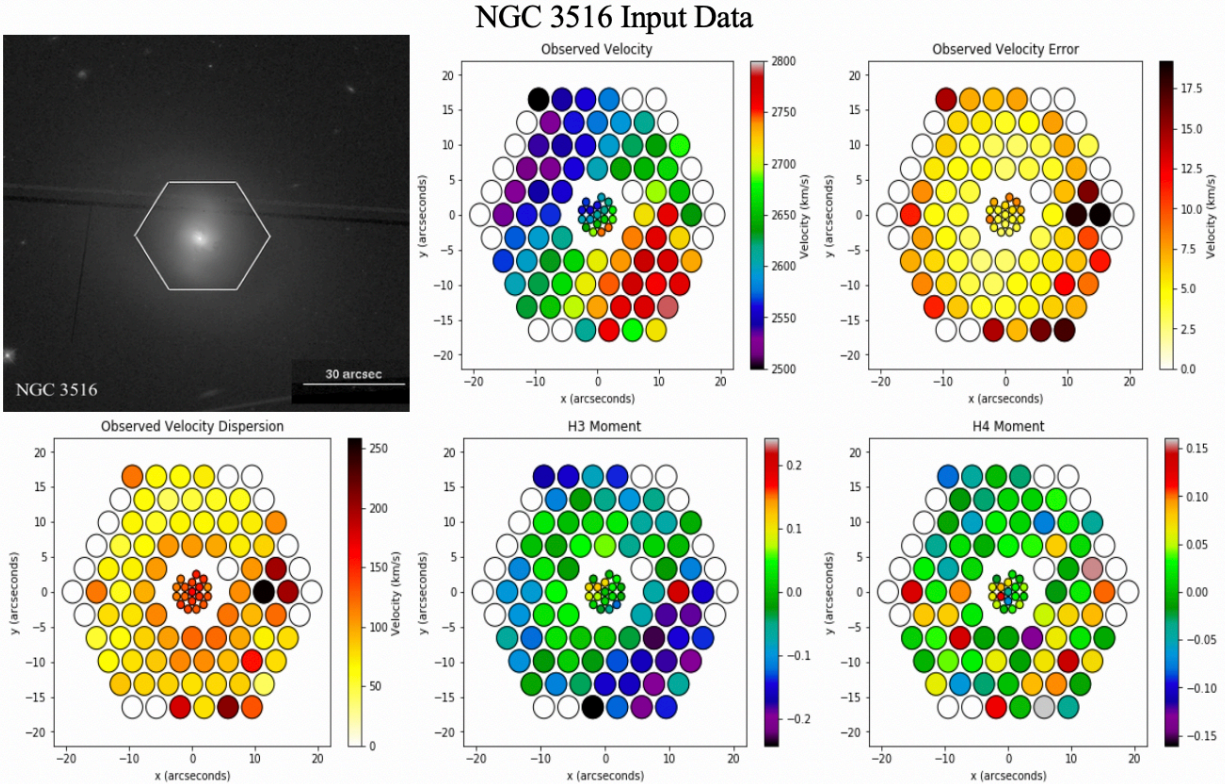
Figure 1: Observed kinematic data for NGC 3516. All images are oriented with North upwards and East to the left. From left to right the top row shows: the HST WFC3 image of NGC 3516 with a hexagonal area to represent the HexPak field of view compared to the physical size of the galaxy; the two-dimensional projection of the recessional velocities for each HexPak fiber (velocity map) in NGC 3516; the error associated with the recessional velocity for each fiber in the HexPak IFU. From left to right the bottom row shows: the velocity dispersion for each fiber in HexPak; the third Gauss-Hermite moment, h_3, for each fiber; the fourth Gauss-Hermite moment, h_4, for each fiber. Data from Figure 1 of Batiste et. al (2017).

HexPak IFU and details of the locations and sizes of each of the fibers. While only ~12.5mm x 11.5mm in size, HexPak provides highly spatially resolved data with 111 total fibers covering roughly a 41" x 36" hexagonal field of view. This IFU contains 18 fibers each 0.937" in size forming a central bundle enclosing ~6" diameter circle and a surrounding bundle of 84 fibers, each 2.812" in size, forming a hexagon. The remaining 9 fibers are sky fibers, which form an L-shape in the perimeter of the IFU located about one arcmin from the center of Hexpak. Data were taken in the 4600-5600Å wavelength range with a spectral resolution of 2.02Å. Each galaxy was observed for between 4-8 hours in order to achieve a target minimum signal to noise ratio of 10-15 for each fiber.
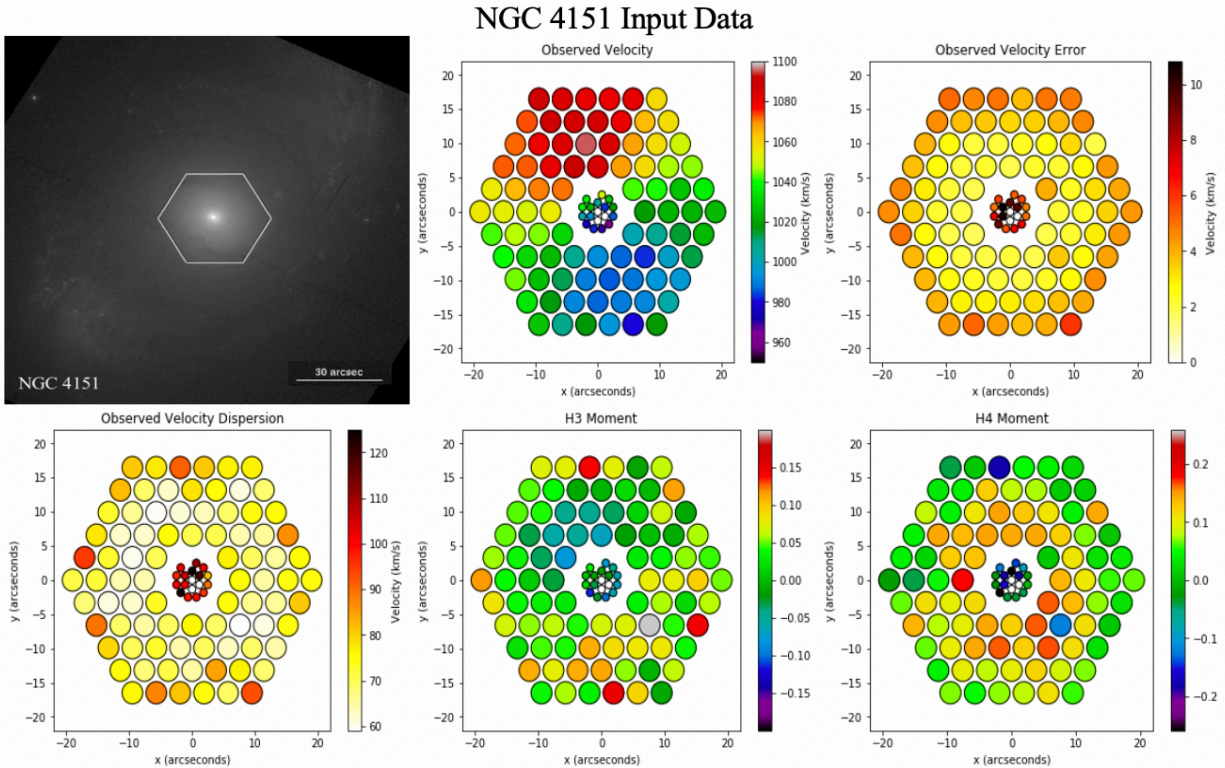
Figure 2: Observed kinematic data for NGC 4151. Refer to Figure 1 for figure description. Data from Figure 1 of Batiste et. al (2017).

The HexPak IFU, designed for nearly face-on galaxies, has sufficient spatial resolution to resolve small non-axisymmetric, or non-circular motions, caused by a bar or a bar-like component. An IFU can spatially resolve a smaller region using smaller fibers, but this reduces the amount of light entering each fiber. Consequently, achieving sufficient signal to noise ratio for smaller fibers requires longer exposure times to allow enough light to enter the aperture. HexPak has high spatial resolution in the central bundle where brightness is not an issue, but in the outer rings HexPak must sacrifice its spatial resolution where the surface brightness is lower, to achieve the desired signal to noise ratio. HexPak is ideal for moderately inclined (not close to face-on or edge-on profiles) and nearby galaxies, since low inclination galaxies provide a clear view of the galaxy kinematics, and nearby galaxies can be more spatially resolved due to their size in the sky. High inclination galaxies obscure observations of kinematic and photometric structure due to overlapping structural components and contamination from dust and light.
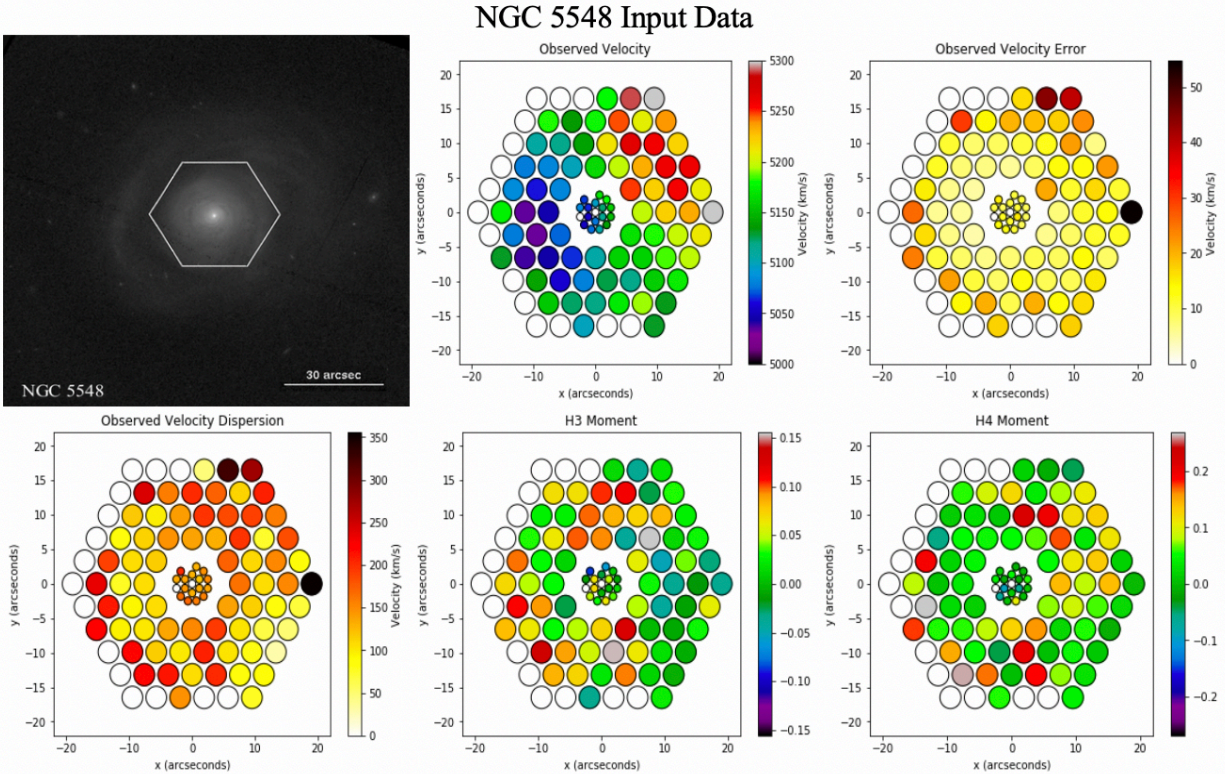
Figure 3: Observed kinematic data for NGC 5548. Refer to Figure 1 for figure description. Data from Figure 2 of Batiste et. al (2017).

This data will, therefore, allow us to model the non-axisymmetric velocities present in velocity maps. NGC 3516, NGC 4151, and NGC 5548 make ideal candidates for a study of kinematically distinct substructure within AGN, as HexPak produces best results for nearby, large, bright, and nearly face-on objects. For this sample, the HexPak field of view extends beyond the effective radius of nearly every galaxy component in the sample. In the case of NGC 4151, the effective radius of the disk extends 10" past the extent of HexPak according to Be09.

Details of the data reduction and analysis processes will not be discussed here at length but can be found in Ba17a. Using the penalized pixel-fitting method (*pPXF*[5]), publicly available from Michele Cappellari, each fiber was fitted with the line-of-sight velocity distribution and attributed four Gauss-Hermite moment values: the first moment is measured recessional velocity,

[5] Cappellari, Michele. 2020. "Michele Cappellari Python and IDL Programs." *Michele Cappellari*. Accessed March 6. https://www-astro.physics.ox.ac.uk/~mxc/software/.
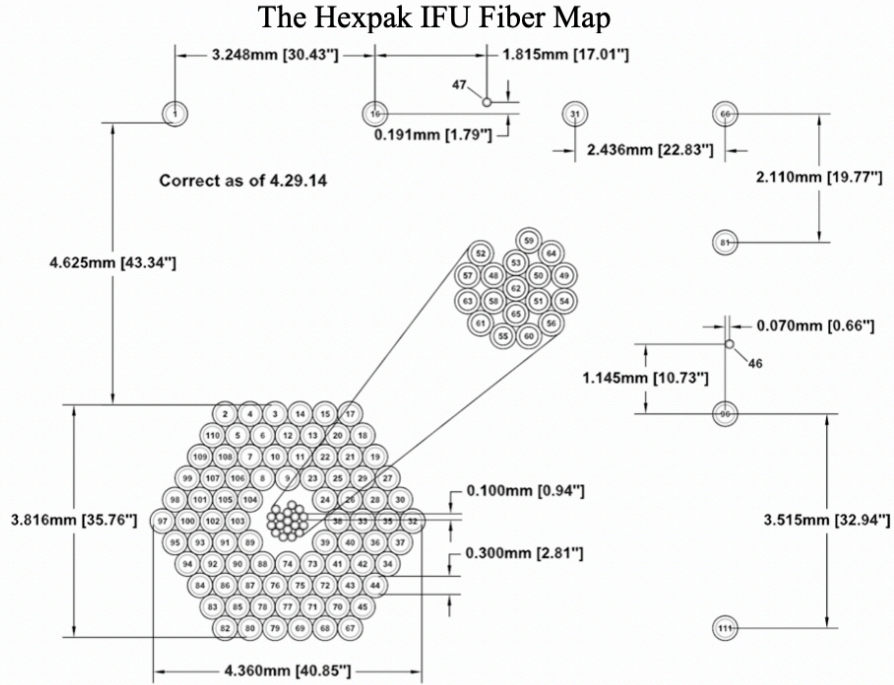
Figure 4: Map of the HexPak IFU fiber positions and sizes (WIYN IFU's 2019).

the second moment is measured velocity dispersion, and the third and fourth moments describe

the asymmetric and symmetric deviations from a Gaussian respectively (Marel & Franx 1993;

Cappellari 2017). Figure 1, Figure 2, and Figure 3 display HexPak maps for each of the four

Gauss-Hermite moments for NGC 3516, NGC 4151, and NGC 5548 respectively. All of the

velocity and error maps are oriented with North pointing up and East to the left. Fibers that are

white did not achieve a sufficient signal to noise ratio to be considered.

3.2 Photometric Data

Reduced HST images of NGC 3516 and NGC 4151 were made available through

private communication courtesy of Professor Misty Bentz. Data were taken using the Hubble

Space Telescope (HST) Wide Field Camera 3 (WFC3) using the UVIS channel and the F547M

filter to achieve a 5122-5772Å wavelength range. Details of the photometric observations can be

found in Bentz et al. (2013) and Be09. The WFC3 UVIS channel produces a 160" x 160" image

with 4096 pixels on each edge, yielding a resolution of 0.04" pixel^{-1}. The large field of view of

HST WFC3, along with its high spatial resolution, provides the opportunity to delve deep into the photometric decomposition of galaxy morphology within the case of our sample. Furthermore, use of a space telescope eliminates atmospheric effects and allows for much higher spatial resolution than can be achieved with seeing-limited ground-based telescopes.

Details of the data reduction and analysis processes can be found in Be09 and Bentz et al. (2013). Photometric modeling requires sky subtracted images must be supplied the mean value of the sky subtracted, the standard deviation of the sky, and the CCD gain, all of which were performed before images were obtained and essential values were provided. These images can be found in the top-left panel of Figures 1, 2, and 3. An HST image of NGC 5548 is provided in the Figure 3 for reference to its visual appearance but has not been photometrically analyzed here. Each of the panels in the of Figures 1, 2, and 3 are oriented with North up and East to the left.

4. Methods

DiskFit was used to model HexPak velocity fields and HST WFC3 images of the galaxies in the sample. The capabilities of *DiskFit* and details of the model it implements can be found in a number of papers by its developers (Barnes & Sellwood 2003; Kuzio De Naray et al. 2012; Reese et al. 2007; Sellwood & Sánchez 2010; Sellwood & Spekkens 2015; Spekkens & Sellwood 2007). As the agreement between the two branches of *DiskFit* modeling is of interest, this research utilizes an approach to modeling both kinematics and photometry presented in Peters & Kuzio De Naray (2017). While Peters & Kuzio De Naray (2017) first model photometry and use the best-fit models as initial guesses for kinematic modeling, we chose to approach the two independently in order to examine the reliability of each modeling branch.

For both types of modeling, it is important to first understand what components *DiskFit* models, as well as the process it uses to deduce parameters. To apply *DiskFit* to data, we

therefore need to consider which components of the galaxy are physically motivated to best understand the results given. Section 4.1 outlines the kinematic modeling procedure for *DiskFit*, and Section 4.2 outlines the same for photometry. The first subsection within both Sections 4.1 and 4.2 will discuss the capabilities of the respective branch of *DiskFit* modeling, some details of the specific algorithm implemented, and assumptions made by the models. The second subsection will detail the process we used to create models for the galaxies in our sample, how we selected initial inputs for *DiskFit* to fit to the data, our method for choosing the best representative model for each galaxy, and the method used for determining errors.

We will employ an abbreviation system to represent the possible component combinations *DiskFit* can model in either branch of its analysis. The first letter of the abbreviation, either K or P, indicates either a kinematic or photometric *DiskFit* model. We use D, B, and RF to represent the distinct kinematic structure of the disk, bar, and radial flow components respectively. Similarly, we use D, B, and Blg to for photometric models of the disk, bar, and bulge components respectively. For example, K-D-RF represents a model produced from *DiskFit* kinematics containing a disk and radial flow components; similarly, P-D-B-Blg denotes a model containing distinct photometric disk, bar, and bulge components. We note that in models from both kinematic and photometric data, the bar component is represented by the letter 'B', and not to be confused with the bulge component (Blg) which is exclusive to the photometric branch of *DiskFit*. Table A1 contains a summary of all the model abbreviations listed above and other abbreviations employed throughout this paper.

4.1 Kinematics

4.1.1 *DiskFit* Kinematic Modeling Abilities

The kinematic branch of *DiskFit* requires an input velocity field to model disk rotation and non-axisymmetric motion caused by a bar or bar-like flow. The model employed assumes a thin and flat inner disk and that the perturbation to circular motion has a fixed principal axis; this assumption for the bar-like flow prevents inclusion of spiral arm features, but the effect of these features is included in the error calculation. Since *DiskFit* attempts to find best-fit parameter values for the whole galaxy, it "averages over" the non-circular motions created by the spiral features when calculating the position and strength of the non-axisymmetric motion.

The simplest case for *DiskFit* is a pure rotation model (K-D), reflecting only motion from a disk component. The user can add a bar, or bar-like flow, modeled by "lopsided" ($m = 1$) or "bisymmetric" ($m = 2$) non-circular motions; this disk and bar model is referred to as a K-D-B model. Equation 1 (Equation 5 of Spekkens & Sellwood 2007) shows the formula used to calculate the model velocity of each point in the velocity map. It can add radially symmetric ($m = 0$) flows using Equation 2 (Equation 7, as above, of Spekkens & Sellwood 2007), and additionally model these radial flows simultaneously with either shape of non-circular motion. This enables the user to produce a K-D-RF model, or a K-D-B-RF if all three components are included. Variables contained in these equations are defined by disk inclination i, harmonic order m, model velocity V_{mod}, systemic recessional velocity V_{sys}, average disk component velocity V_t, average radial flow velocity V_r, the tangential velocity component of the bar-like component $V_{m,t}$, the radial velocity component of the bar-like component $V_{m,r}$, angle between point and disk major axis θ, and an angle between point and bar major axis θ_b.

$$(1)\ V_{mod} = V_{sys} + \sin i \left[V_t \cos\theta - V_{m,t} \cos(m\theta_b)\cos\theta - V_{m,t} \sin(m\theta_b)\sin\theta \right]$$

$$(2)\ V_{mod} = V_{sys} + \sin i [V_t \cos\theta - V_r \sin\theta]$$

Even though *DiskFit* assumes a flat inner disk, it is capable of modeling a warped disk beginning at some radius r_w, at which the position angle and ellipticity of the disk fluctuate quadratically. The warped disk (K-wD) model inherently inhibits a simultaneous search for non-axisymmetric motion or radial flows (Sellwood & Spekkens 2015). Turbulence in the disk, Δ_{ISM}, is accounted for in the velocity error produced by the model; the error for each velocity in the output model is equal to the sum in quadrature of the disk turbulence and the observed measured velocity error for that fiber.

DiskFit asks the user to supply initial guesses for parameters, and proceeds to fit them to the data to produce the most accurate model (see example input file in Figure A1). All models require an estimate for V_{sys}. For the disk component it needs an initial guess for the position angle of the disk major axis PA_{disk}, the disk ellipticity e_{disk}, and the position of the center of rotation in the galaxy. PA_{disk} is defined as degrees Eastwards from North to the receding side of the galaxy, in the sky plane. For the non-axisymmetric component, it requires an initial guess for the position angle of the non-circular motion, PA_{bar}, and the harmonic order of the component ($m = 1$ or $m = 2$). For the K-wD model, we must supply *DiskFit* with guesses for the radius at which the warp begins r_w and the projected change in ellipticity and position angle from r_w to the outer-most ring in the fit.

4.1.2 Kinematic Modeling Procedure

First, we determined which components were physically motivated. Since each of the galaxies in the sample contains an AGN, radial flows are possible. The presence of a bar was indicated by the morphological classification obtained from NED. The K-wD model was of particular interest for NGC 5548 due to its tidal structures. Initial guesses for component ellipticities were obtained from *Galfit* models from Be09 (see Table A2 for available *Galfit*

parameters) and any remaining input values were set to the suggested initial guesses from the *DiskFit* documentation.

We used three main points to deduce the best-fit model: a X^2 value, residual plots, and a comparison between input and output rotation curves. *DiskFit* outputs a reduced X^2 value to represent goodness of fit between the model and the data, a rotation curve, and the model velocities of each component at each point specified in the input velocity map. Values of X^2 greater than one imply a poor fit and values less than one imply the data is being overfit; values closer to one, either larger or smaller, represent a better fit to data. *DiskFit* outputs a model velocity map for the galaxy and a residual plot, subtracting the model velocity from the input velocity for each fiber, to determine if any clear structure remains, possibly indicating need to add a subsequent component. From the input data we can generate a rotation curve by simulating a one-dimensional slit across the kinematic major axis of the velocity field to compare to the rotation curve produced by *DiskFit*. Additionally, we can compare the values output by *DiskFit* to results from literature from either *DiskFit* or other programs to further test accuracy. See Figure A2 for an example output file produced by *DiskFit* kinematic modeling.

We began the modeling process with the K-D model, and systematically added components, finding both the K-D-B and K-D-RF models next, until the most complex, K-D-B-RF model, was reached. All of the initial guesses we could obtain from NED were used. The ellipticities of each component were obtained from Be09 and the disk position angle was estimated through visual placement of the kinematic major axis of rotation from the velocity fields from Ba17a. Any required input values remaining were set to the value suggested in the *DiskFit* documentation. We ran the K-D and modified the center, disk ellipticity, and disk position angle parameters until we found general agreement between the input and output data

through comparing X^2, rotation curves, and residual plots. We then held the center fixed in all subsequent models, similar to the method employed by Peters & Kuzio De Naray (2017). In the K-D-B and K-D-RF models we only adapted the parameters of the component added to the disk (either the bar or radial flow) to find a best-fit model. In the K-D-B-RF model, as well as the K-wD model, we modify the input guesses for all parameters to find the best-fit. This is because models with three components can cause more error from difficulty decomposing overlapping components, so we spend more time ensuring an appropriate fit is found. The radii at which *DiskFit* will evaluate the velocity of the given components were selected from the radii of the rings in the HexPak IFU. Our initial guess for Δ_{ISM} = 10 km/s as per Peters & Kuzio De Naray (2017) but we ensured that changes in Δ_{ISM} or model smoothing parameters, if used, did not affect the determination of best-fit model. After obtaining all possible models from *DiskFit*, one was selected based on X^2, rotation curves, and the residual velocity map and determined to be best-fit ore most accurately representative of the input data.

HexPak velocity maps contain ~100 usable fibers, or spatial resolution elements referred to as spaxels, which are sufficiently small to allow for fast computation time. *DiskFit* generates errors for the output values by generating Bootstrap iterations. For kinematic analysis of velocity maps, we computed 1000 Bootstrap iterations for the uncertainties for every model generated throughout the process. We were able to compute a large number of iterations due to the fast computer run-time. As mentioned earlier, three main tests were used to determine the best-fit model. However, the size of the uncertainties provided an additional test for goodness of fit for two models of the same components if needed.

4.2 Photometry

4.2.1 *DiskFit* Photometric Modeling Abilities

The photometric side of *DiskFit* requires an input image to determine the amount of light coming from each component. As with the kinematic modeling, this model also assumes a flat inner disk and attempts to find a bar component by assuming that it has a fixed position angle that differs from the position angle of the disk. Furthermore, the bar has a different ellipticity than the disk component. The photometric branch cannot model spiral arms and uses the same method as the kinematic branch to average over the influence of the spiral features.

DiskFit can decompose the light for a disk, bar, and a bulge component. The disk and bar have no specified light profiles, while the bulge is assumed to follow the Sérsic function, seen in Equation 3 (Equation 3 of Reese et al. 2007), where r_e is the effective radius, n is the Sérsic index, I_0 is the intensity at the center, and the constant B_n is a function of the Sérsic index. The error associated with each pixel is deduced from the mean value of sky subtracted from the image, the error associated with the sky subtraction mean, and the CCD gain.

$$(3)\ I(r) = I_0 exp\left\{-B_n\left[\left(\frac{r}{r_e}\right)^{1/n} - 1\right]\right\}$$

Initial guesses needed for the photometric modeling are the position angles of the disk and bar, PA_{disk} and PA_{bar}, as well as ellipticities of all three components, e_{disk}, e_{bar}, and e_{bulge}. For photometry, the definition of position angle is degrees Eastwards from North to the first found side of the galaxy in the sky plane. *DiskFit* also asks for an initial guess of the Sérsic index and the effective radius of the bulge. The radii at which the photometric data were extracted were evenly spaced to allow for model smoothing, if necessary. Furthermore, the number of radii were limited due to the processing speed available and the time-intensity for high resolution images.

Outputs for *DiskFit* photometry include best-fit parameters from the model, a X^2 value to represent goodness of fit between the model and the data, and a radial light profile for each component within the fit. In addition to an image including each component in the model,

DiskFit will output an image of each component individually to compare size, orientation, and magnitude. Rather than only depending on the X^2 value to determine the best-fit model, we also utilized the residual photometric images. Photometric *DiskFit* models can then be compared to *Galfit* models of the same galaxies to test the robustness of *DiskFit*.

4.2.2 Photometry Modeling Procedure

Determination of physically motivated components was based on the morphological classification of each galaxy from NED, presented in Table 1. Initial parameter estimates were obtained from NED when available. Values of bulge effective radius, ellipticities of all components from *Galfit* modeling, and bulge Sérsic index were obtained from Be09. We found estimates for the position angles of the disk and bar components from visual inspection of the HST images in Figures 1-3. All remaining parameters began with the default value suggested in the *DiskFit* documentation.

Photometric modeling similarly began with finding the simplest disk-only (P-D) model first. While only adapting the values for the galaxy center and the position angle and ellipticity of the disk, we found the P-D model. We then found the P-D-B and P-D-Blg models by fixing the position of the center and only adapting initial guesses for the parameters for the bar or bulge component respectively. For the three-component (P-D-B-Blg) model, we utilized all parameters to find the best-fit. After obtaining the four possible photometric models, we then determined which model best represented the data by analyzing the X^2 value, the residual images, and comparing the models to others found in literature.

DiskFit uses the same Bootstrap method for generating photometric uncertainties as with the kinematic branch. In the kinematic modeling we were able to produce 1000 Bootstrap iterations since the input used ~100 fibers or spatially resolved pixels (spaxels). However, the

high resolution HST images obtained for this research contain ~16 million pixels causing an incredibly time-intensive error determination. Due to the limited computation speed available, we generated 10 Bootstrap iterations for photometric uncertainties. While some previous photometric analyses with *DiskFit* for low resolution have used high number (~100) Bootstrap iterations for uncertainties, other studies show ~10 iterations are sufficient, especially useful for the high-resolution photometry case (Lewis & Spekkens 2018; Randriamampandry et al. 2016).

5. Results

This section will present the results from modeling NGC 3516, NGC 4151, and NGC 5548 with *DiskFit*. Within discussion of the modeling results for each galaxy, the first subsection will present kinematic results while the second subsection will show the photometric results. For all of these, a table of best-fit values for each model and their residual plots will be displayed. Through examination of the residuals and table values we are able to select the best-fit model and present a general decomposition of its structure and characteristics.

5.1 NGC 3516

5.1.1 Kinematics

As discussed in Section 2, NGC 3516 has a (R)SB(s)0^0 morphological classification and has a clear disk, bar, and bulge component (see top-left panel of Figure 1 for HST image). Thus, kinematically, we expect *DiskFit* to produce the best-fit model for NGC 3516 with a disk component and non-axisymmetric motion caused by the bar. Additionally, radial flows are possible from the AGN influence. Table 2 shows the output parameters for each of the five possible kinematic *DiskFit* models. At a glance, the reduced X^2 value of the K-D-B model is closer to one, suggesting it might be the best-fit. However, the reduced X^2 value is not the only goodness of fit test employed to determine the best-fit model.

	Disk (K-D)	Disk and Bar (K-D-B)	Disk, Bar, and Radial Flow (K-D-B-RF)	Disk and Radial Flow (K-D-RF)	Warped Disk (K-wD)
NGC 3516 Kinematic Models					
PA_{disk} (°)	225.91 ± 1.50	227.45 ± 1.22	237.03 ± 3.27	233.02 ± 6.72	222.71 ± 2.34
e_{disk}	0.21 ± 0.07	0.20 ± 0.01	0.21 ± 0.02	0.17 ± 0.04	0.13 ± 0.06
i_{disk}	37.73 ± 6.17	36.66 ± 1.15	37.54 ± 1.69	34.11 ± 4.16	29.08 ± 6.59
PA_{bar} (°) (disk)	...	109.53 ± 10.77	77.07 ± 7.24	...	...
PA_{Vmt} (°) (sky)	...	161.31	310.89	...	...
PA_{Vrt} (°) (sky)	...	243.33	226.72	...	...
m	0	1	1	0	0
r_{warp}	...	...	...	...	2.57 ± 0.05
e_{warp}	...	...	...	...	0.10
PA_{warp}	...	...	...	...	6.19 ± 4.16
V_{sys}	2648.59 ± 1.87	2619.08 ± 5.30	2673.72 ± 11.55	2651.98 ± 1.72	2648.53 ± 1.85
X^2	2.343912	1.426073	0.412983	1.872320	2.330095

Table 2: Kinematic parameter values for the full set of models output by *DiskFit*. The parameters are as follows: PA_{disk} is the position angle of the disk in the sky plane, in kinematics defined as degrees Eastwards from North to the receding side of the disk major axis; e_{disk} is the ellipticity of the disk, defined by $e_{disk} = 1 - b/a$; i_{disk} is the inclination of the disk ranging from face-on galaxies at 0° to edge-on galaxies at 90°; PA_{bar} (°) (disk) is the position angle of the bar given in the disk plane; PA_{Vmt} (°) (sky) is the position angle of the tangential component of the non-axisymmetric flow force (bar-like component) in the sky plane; PA_{Vrt} (°) (sky) is the position angle of the radial component of the non-axisymmetric flow force in the sky plane; m represents the harmonic order of the bar component; r_{warp} is the radius at which the warp transitions from flat to curved; e_{warp} is the change in ellipticity from r_{warp} to the outermost ring in the fit; PA_{warp} is the change in position angle from r_{warp} to the outermost ring in the fit; V_{sys} is the systematic recessional velocity associated with the whole galaxy. A reduced X^2 value is output by *DiskFit* to represent goodness of fit.

Since *DiskFit* outputs a model velocity field, we can subtract the velocities of the model from the data for each spaxel used in the minimization, to learn where inconsistencies are located and the size of the modeling error. The residual plots are shown in Figure 5, with lines plotted on top associated with the position angle of the disk and the tangential and radial components of the non-axisymmetric motion, caused by the bar. From Figure 5, it appears that large residuals tend not to be along the position angle lines.

While the reduced X^2 values suggest best representation by a K-D-B model, the bottom-left panel of Figure 5 contains the weakest residuals, suggesting inclusion of radial flows into our model for NGC 3516 may provide a better overall fit. These provide good evidence for the disk
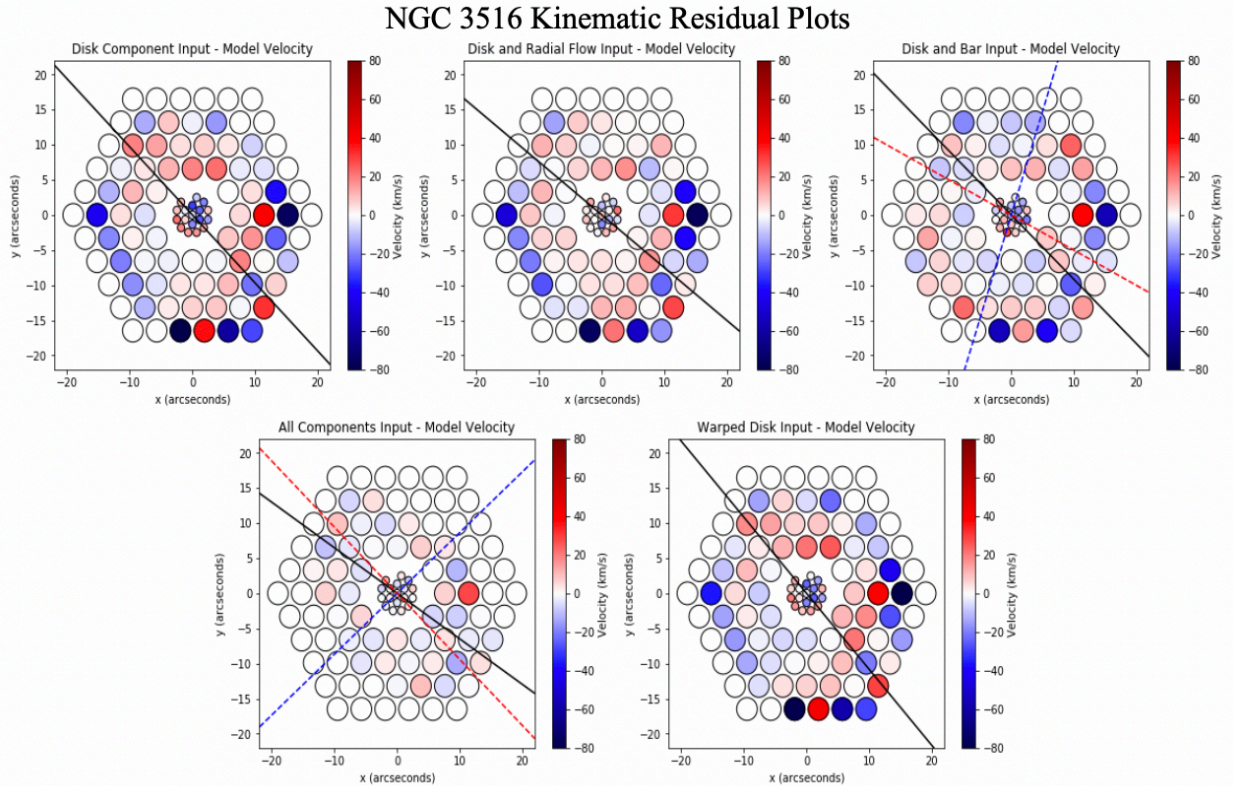
Figure 5: All panels display the residual Hexpak plot, computed by subtracting the model velocity from each input velocity in the velocity field. The solid black line denotes the position angle of the disk component in the sky plane. The dashed red and blue lines represent the position angles of the tangential and radial non-axisymmetric flow forces (or bar-like components) respectively, also in the sky plane. The top row from left to right shows: the K-D model; the K-D-RF model; the K-D-B model. The bottom row from left to right shows: the K-D-B-RF model and the K-wD model.

and bar components, but the addition of radial flow needs more evidence. The rotation curves of all five types of kinematic models are shown in in Section 6.1.2. This section will instead first present the input and output rotation curves for NGC 3516 alongside a comparison of velocities attributed to the non-circular motion and radial flows (shown in Figure 6). However, the trend of the input rotation curve is best followed by the model rotation curve for the K-D-B-RF model. While the offset between input and output rotation curves, seen in Figure 6, may seem large, examination of all output rotation curves show that the offset persists for all five possible kinematic models (see Section 6.1.2 for discussion). We note the rotation curves in Section 6.1.2 show the need to incorporate radial flows into the model for NGC 3516, despite the supposed overfit suggested by the reduced X^2 value.
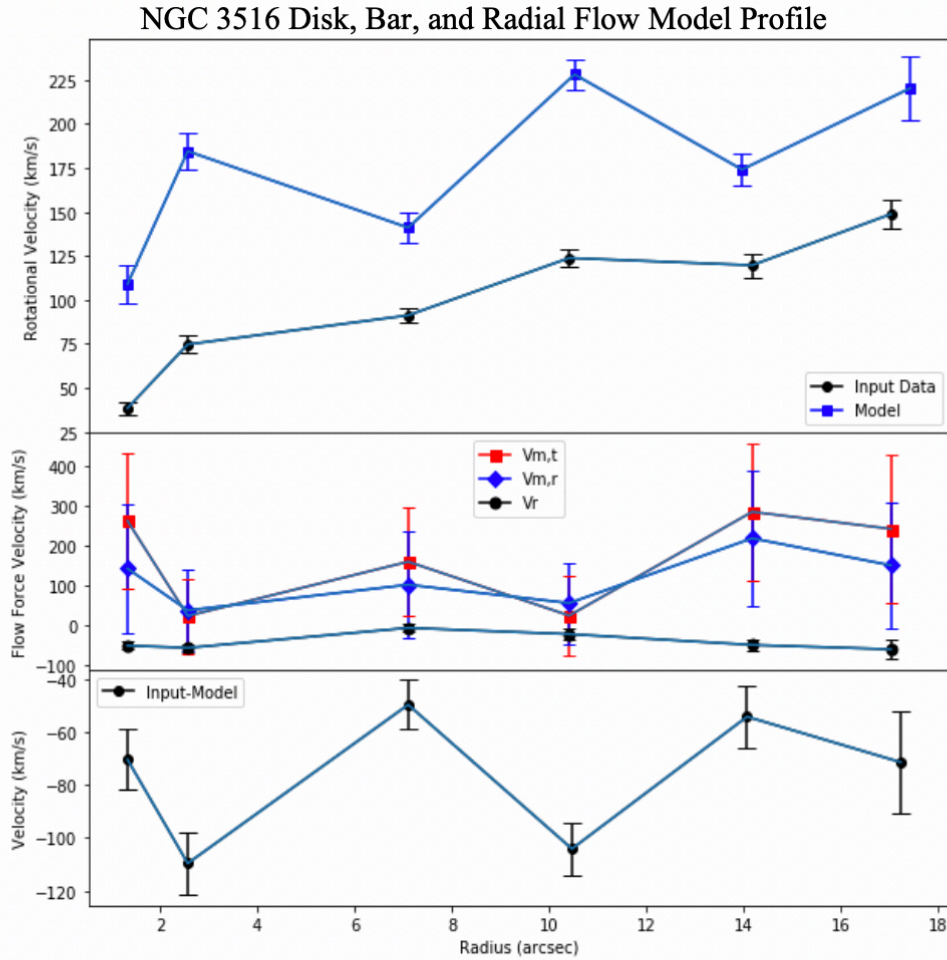
Figure 6: NGC 3516 rotation curves from the best-fit (K-D-B-RF) model. All three panels are on the same scale for radius on the *x*-axis. From top to bottom the panels show: input rotation curve from averaging a two spaxel wide pseudo-slit of velocities along the observed disk major axis against the output rotation curve calculated by *DiskFit*; the tangential and radial flow force components of the non-axisymmetry, and the radial flow force component, plotted against radius; the discrepancy between the input and output rotation curves calculated by subtracting the model rotation curve velocities from input.

5.1.2 Photometry

As before, the morphological classification and observations suggest a P-D-B-Blg model is best representative of NGC 3516. Thus, we expect *DiskFit* photometry to best decompose NGC 3516 into a P-D-B-Blg model. Table 3 presents the parameters from the four types of possible photometric models. *DiskFit* finds high X^2 values for the P-D and P-D-B, but it is much lower with the addition of a bulge component, suggesting significant evidence for a strong bulge. This strong evidence supporting a bulge lies in the nature of NGC 3516 being lenticular (see

NED classification in Table1), however, the size and brightness of the bulge may be overestimated due to the massive AGN influence. The photometric branch assumes the bulge is nearly spherical and central, while the disk and bar have different position angles and ellipticities from one another. It is possible *DiskFit* is having trouble deciding what amount of the large AGN intensity to attribute to each component and decides it is originating from the bulge. The P-D-B-Blg model has the lowest X^2 value, suggesting a confirmation of our observational expectations.

The next step to determining goodness of fit is interpreting the residual photometric images. *DiskFit* creates a model of the galaxy in the same dimensions as the input image and assigns each pixel value an intensity based on the physically motivated model and the minimization algorithm. It additionally provides a residual image, subtracting the intensity of corresponding pixels from each image to determine spatially where *DiskFit* fails and the size of the difference with each model created. Figure 7 shows the residual images from the four *DiskFit* models. All images are shown with the same color intensity scale.

Visual examination of the residuals confirms size and brightness of the bulge may be overestimated due to the AGN for NGC 3516. The addition of a bar to a P-D model is not as impactful as when it is added to the P-D-Blg model. The most representative model of NGC 3516 is the P-D-B-Blg model as it shows the smallest pattern leftover in the residual image. The residual image for the best-fit P-D-B-Blg model clearly leaves a four spiral arm pattern representative of *DiskFit* averaging over the perturbation caused by the bar.

5.2 NGC 4151

5.2.1 Kinematics

	Disk (P-D)	Disk and Bar (P-D-B)	Disk and Bulge (P-D-Blg)	Disk, Bar, and Bulge (P-D-B-Blg)
	NGC 3516 Photometric Models			
PA_{disk} (°)	190.40 ± 6.13	182.86 ± 5.13	197.67 ± 4.55	183.43 ± 0.55
e_{disk}	0.38 ± 0.02	0.48 ± 0.04	0.05 ± 0.17	0.59 ± 0.02
i_{disk}	51.37 ± 1.73	58.75 ± 2.51	18.19 ± 31.96	66.08 ± 1.22
PA_{bar} (°) (sky)	...	78.33 ± 1.22	...	57.25 ± 2.38
PA_{bar} (°) (disk)	...	-7.86	...	-16.52
e_{bar}	...	0.64 ± 0.01	...	0.26 ± 0.01
r_e (")	...	...	7.71 ± 2.50	4.45 ± 0.16
I_{bulge} (ADU)	...	...	441.34 ± 98.12	841.45 ± 52.31
n	...	...	3.40 ± 0.44	2.80 ± 0.05
e_{bulge}	...	...	0.14 ± 0.03	0.00 ± 0.00
Disk % light	100	88.75 ± 6.88	52.33 ± 4.25	52.25 ± 2.75
Bar % light	...	11.25 ± 7.53	...	14.80 ± 1.63
Bulge % light	...	...	47.67 ± 5.14	32.95 ± 0.47
X^2	28.152832	26.855446	6.934559	6.297995

Table 3: Photometric parameter values for the full set of models output by *DiskFit*. Parameters are defined as follows: PA_{disk} is the position angle of the disk in the sky plane, for photometry defined as degrees Eastwards from North to the nearest side of the disk major axis; e for the disk, bar or bulge, is the ellipticity of the that component defined by $e = 1 - b/a$ for each component individually; i_{disk} is the inclination of the disk ranging from face-on galaxies at 0° to edge-on galaxies at 90°; PA_{bar} (°) (sky) is the position angle of the bar given in the sky plane; PA_{bar} (°) (disk) is the position angle of the bar in the disk plane; r_e is the effective radius of the bulge; I_{bulge} is the intensity of the bulge given in ADU; n is the Sérsic index for the bulge component. *DiskFit* photometry outputs the percentage of light attributed to each component in the fit and a reduced X^2 value to represent goodness of fit.

As discussed in Section 2, NGC 4151 (see top-left panel of Figure 2 for HST image) is classified as (R')SAB(rs)ab indicating the kinematics will likely be represented by a disk. The weak bar classification of NGC 4151 will test the ability of *DiskFit* to quantify non-circular motion with kinematic data. *DiskFit* should identify some non-circular motion since it still has a bar component, but with a weaker contribution than that of a strongly barred galaxy, like NGC 3516. Additionally, radial flows are possible from the AGN influence. Table 4 gives the parameters from kinematic modeling of NGC 4151. Initial interpretation of the reduced X^2 values indicates *DiskFit* is overfitting all models, with every value less than one. The K-D-RF flow model has the closest reduced X^2 values to one, suggesting it is the best representative model.
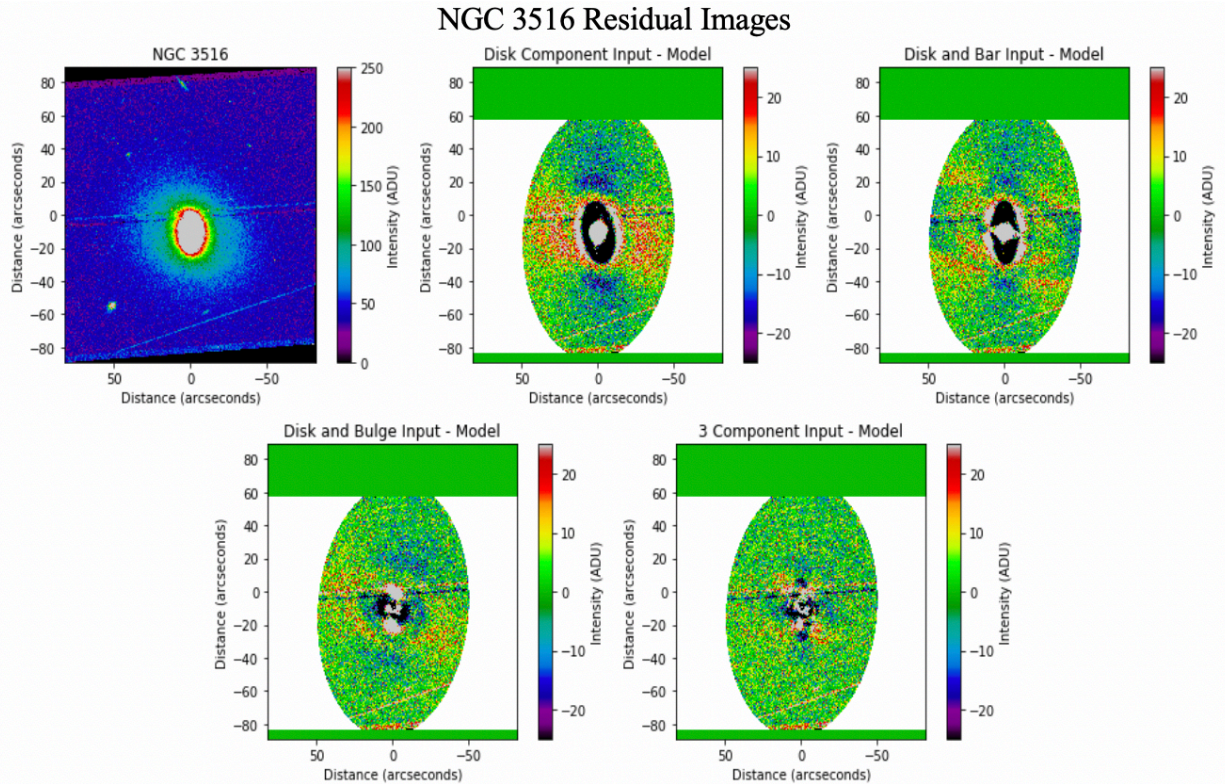
Figure 7: All panels show the residuals given by subtracting each model from the input image of NGC 3516 from HST WFC3. The top row from left to right shows: the HST image (from Be09), the P-D model, and the P-D-B model. The bottom row from left to right shows: the P-D-Blg model and the P-D-B-Blg model.

The residual images for four *DiskFit* models are shown in Figure 8. The K-D model is clearly failing in many areas and the addition of radial flow motion increases structure in the residuals, in contrast with our previous hypothesis from the reduced X^2 value that a K-D-RF model was best for NGC 4151. Addition of a bar component to the K-D model seems to be far more effective representing the input velocity map than adding the radial flow component. While the X^2 values for the K-D-B-RF model of NGC 4151 suggest overfitting of the input data, the residual plot in Figure 8 suggests this may still produce the best representation of the velocity map. The second best X^2 value comes from the K-wD model but the residuals show clear remaining structure, eliminating this from consideration as best-fit has; however, Table 4 does show a possible warp ~15" from its center, possibly correlated with the pseudo-ring structure observed in images of NGC 4151.

	Disk (K-D)	Disk and Bar (K-D-B)	Disk, Bar, and Radial Flow (K-D-B-RF)	Disk and Radial Flow (K-D-RF)	Warped Disk (K-wD)
	NGC 4151 Kinematic Models				
PA_{disk} (°)	20.54 ± 1.23	21.04 ± 0.96	23.99 ± 2.05	22.72 ± 3.20	20.12 ± 1.50
e_{disk}	0.20 ± 0.05	0.15 ± 0.05	0.16 ± 0.03	0.21 ± 0.05	0.20 ± 0.05
i_{disk}	37.21 ± 4.99	31.41 ± 5.24	33.10 ± 3.66	37.64 ± 4.83	36.51 ± 5.25
PA_{bar} (°) (disk)	...	30.08 ± 14.98	17.13 ± 13.05	...	...
PA_{Vmt} (°) (sky)	...	47.35	38.46	...	...
PA_{Vrt} (°) (sky)	...	-34.79	-45.82	...	...
m	0	1	1	0	0
r_{warp}	...	...	...	...	14.85
e_{warp}	...	...	...	...	0.10
PA_{warp}	...	...	...	...	2.54 ± 3.14
V_{sys}	1040.71 ± 0.78	1042.01 ± 1.70	1042.51 ± 1.43	1041.02 ± 0.89	1041.06 ± 0.89
X^2	0.422746	0.288983	0.251974	0.489878	0.475867

Table 4: Kinematic data for the full set of models of NGC 4151. Refer to Table 2 for table description.

The K-D-B-RF model produces values most aligned with those found in published literature and the most accurate model velocity field. The rotation curves for all kinematic models, presented in Section 6.1.2, show most consistency between a K-D-B-RF model and the input rotation curve. Accordingly, we suggest the K-D-B-RF model is best for NGC 4151. We present the rotation curve and strength of the flow forces from the bar and radial flows in Figure 9. The input and output rotation curves, as for NGC 3516, displays systematic offset in the velocity at each radius to be discussed in Section 6.1.2. The strength of the tangential and radial components both follow the same general trend with increasing distance from the center.

5.2.2 Photometry

While *DiskFit* kinematically detected the weak (AB) bar in NGC 4151, we now want to know if *DiskFit* photometry will be able to detect the weak bar. Additionally, NGC 4151 contains a weak (ab) bulge component. Due to the nature of *DiskFit* searching for a relatively spherical bulge, and a disk and bar component with different position angles and ellipticities, we suspect *DiskFit* will have more difficulties locating the weak bar and bulge components.
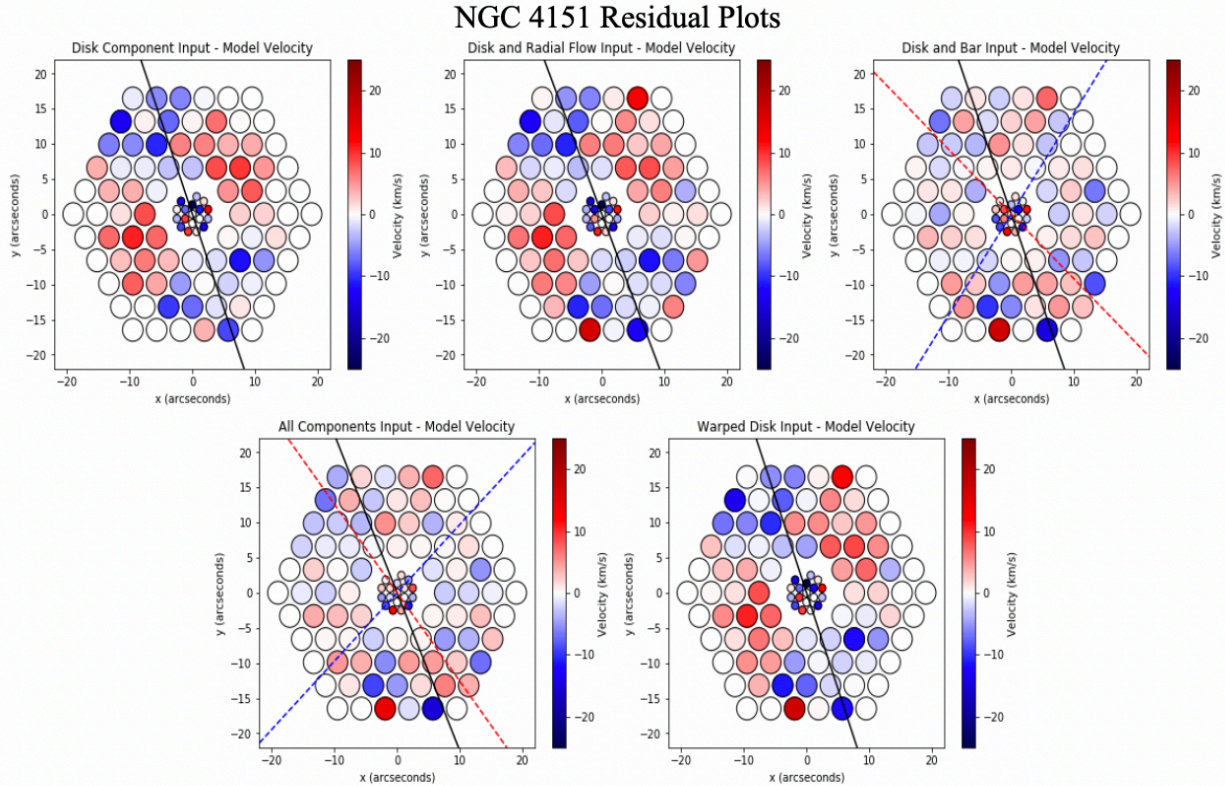
Figure 8: Hexpak residual plots for NGC 4151. Refer to Figure 5 for figure description.

Just as expected, there were modeling issues, and we failed to find a model to represent

NGC 4151 as a P-D-Blg galaxy or as a P-D-B-Blg model. The results for the P-D and the P-D-B

model can be found in Table 5. The X^2 values indicate the P-D model is better but knowing

NGC 4151 has a weak bar classification (see NED classification in Table 1), we must delve

deeper into the models and residuals given by *DiskFit*.

The full model decomposition output by *DiskFit* for the P-D model is presented in Figure

10, and for P-D-B model in Figure 11. A comparison between the residuals, shown in the right

panel of Figure 10, and the bottom-right panel of Figure 11, show the P-D model fails in

numerous areas in the outer regions of the model. The P-D-B model also clearly display a tightly

wound central spiral structure unable to be modeled by *DiskFit*. The large residual structure for

the P-D-B model suggests *DiskFit* is having trouble finding the bar we have found kinematically,
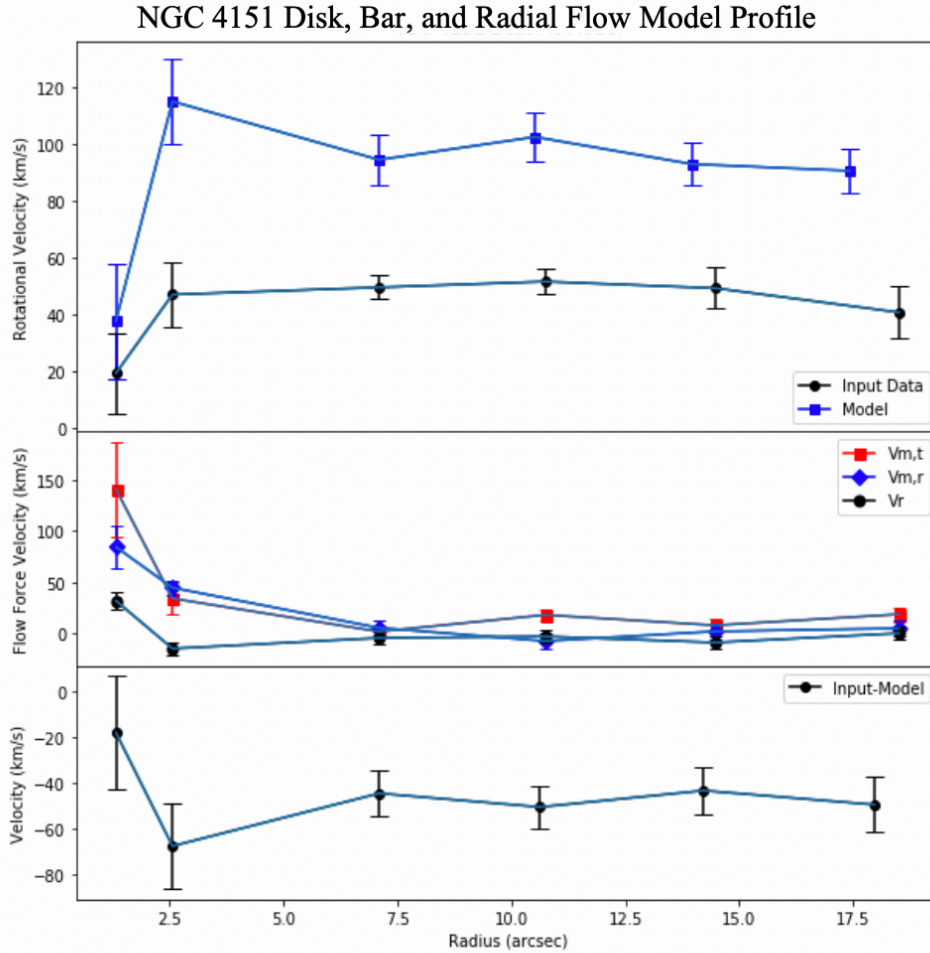
Figure 9: Best-fit (K-D-B-RF) kinematic model profile for NGC 4151. Refer to Figure 6 for figure description.

possibly because of its weak photometric presence. We conclude that it could be possible to

misclassify NGC 4151 as photometrically unbarred.

5.3 NGC 5548 Kinematics

As discussed in Section 2, the classification for NGC 5548 is (R')SA(s)0/a indicating it is

unbarred (see top-left panel of Figure 3 for HST image). Again, the AGN nature of NGC 5548

possibly suggests radial flows may be present in the stellar kinematics. While the two previous

galaxies had no expected warp, NGC 5548 is believed to contain a SMBH pair at its center as a

result of a major merger event one billion years ago, causing two large tidal features and ripples

or rings in the disk (Li et al. 2016). Consequently, *DiskFit* should find a reasonable fit to a K-wD

NGC 4151 Photometric Models		
	Disk (P-D)	Disk and Bar (P-D-B)
PA_{disk} (°)	111.58 ± 7.82	107.03 ± 14.10
e_{disk}	0.32 ± 0.02	0.26 ± 0.07
i_{disk}	46.93 ± 1.96	42.03 ± 6.20
PA_{bar} (°) (sky)	...	115.09 ± 12.95
PA_{bar} (°) (disk)	...	-79.21
e_{bar}	...	0.50 ± 0.09
r_e (pixels)	...	...
I_{bulge} (ADU)	...	...
n	...	...
e_{bulge}	...	...
Disk % light	100	59.73 ± 12.25
Bar % light	...	40.27 ± 16.48
Bulge % light	...	...
X^2	26.695366	352.677979

Table 5: Photometric P-D and P-D-B model parameters for NGC 4151. Refer to Table 3 for table description.

model. The model parameters from kinematic fits of NGC 5548 can be found in Table 6. The X^2 values imply a best representation from a K-D-B model while also indicating a failure to accurately model the warped disk of NGC 5548.

Comparison of the residual plots for each of the models allows for a more educated selection for the best-fit model; the residual plots for the NGC 5548 kinematic fits are shown in Figure 12. The warped nature of NGC 5548 is clearly not being well represented by the K-wD model employed by *DiskFit* as shown by Figure 12. The addition of a bar component to a K-D model seems more significant than the addition of a radial flow component based on the residuals. However, it appears the most representative velocity map is produced with three components. Despite slight overfitting indicated by the reduced X^2 values less than one, the presence of a radial flow in the two previous galaxies suggest it should be included here as well. Both the reduced X^2 values and the residual images of all five kinematic models suggest non-circular motion, or a bar component, for NGC 5548, potentially contradicting the unbarred classification of this galaxy. It is important to remember that *DiskFit* models bars as non-circular
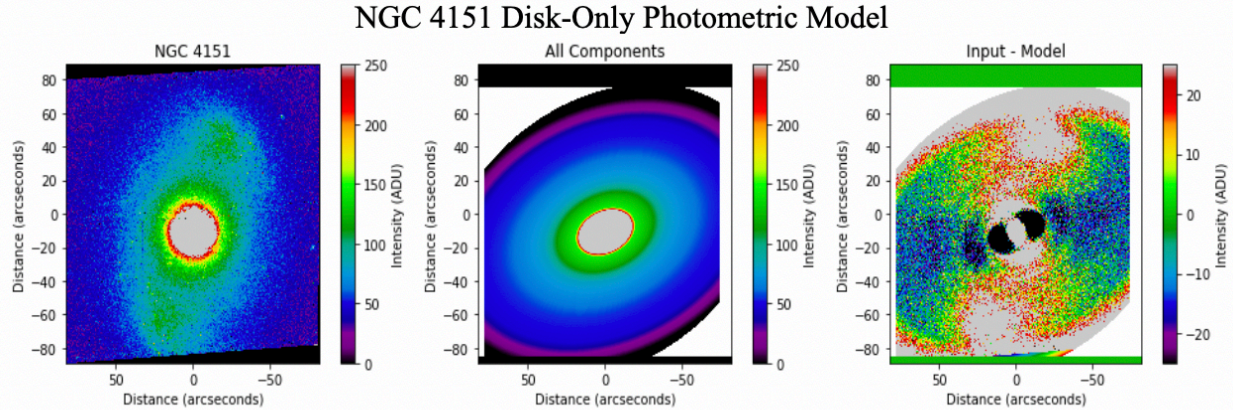
Figure 10: NGC 4151 P-D model. From left to right the images show: input HST image of NGC 4151; the P-D model; the residuals between the two preceeding images.

motions relative to normal disk rotation. Thus, the kinematic impact of the major merger event could be the cause of the non-circular motion detected.

A profile of the best-fit K-D-B-RF model is shown in Figure 13. The input and output rotation curves for NGC 5548 continue the trend of the velocity offset. The chaotic nature of the radial flows and the non-circular motions are particularly highlighted in the middle panel of Figure 13.

6. Analysis

DiskFit provides more information to enable the user to further dissect each of the models it presents. Section 6.1 and Section 6.2 will analyze the kinematic and photometric models produced by *DiskFit* respectively. A discussion about the agreement between the two branches of *DiskFit* modeling is located in Section 6.3. Observed relationships between the Gauss-Hermite moments from the *pPXF* fit to the line-of-sight velocity distribution and the input and model data are presented in Section 6.4.

6.1 Kinematic Model Analysis

6.1.1 Distinct Kinematic Structure

Kinematic modeling results for NGC 3516 modeling suggest a best fit from a K-D-B-RF model as presented in Section 5.1. The minimization process used by *DiskFit* attributes a
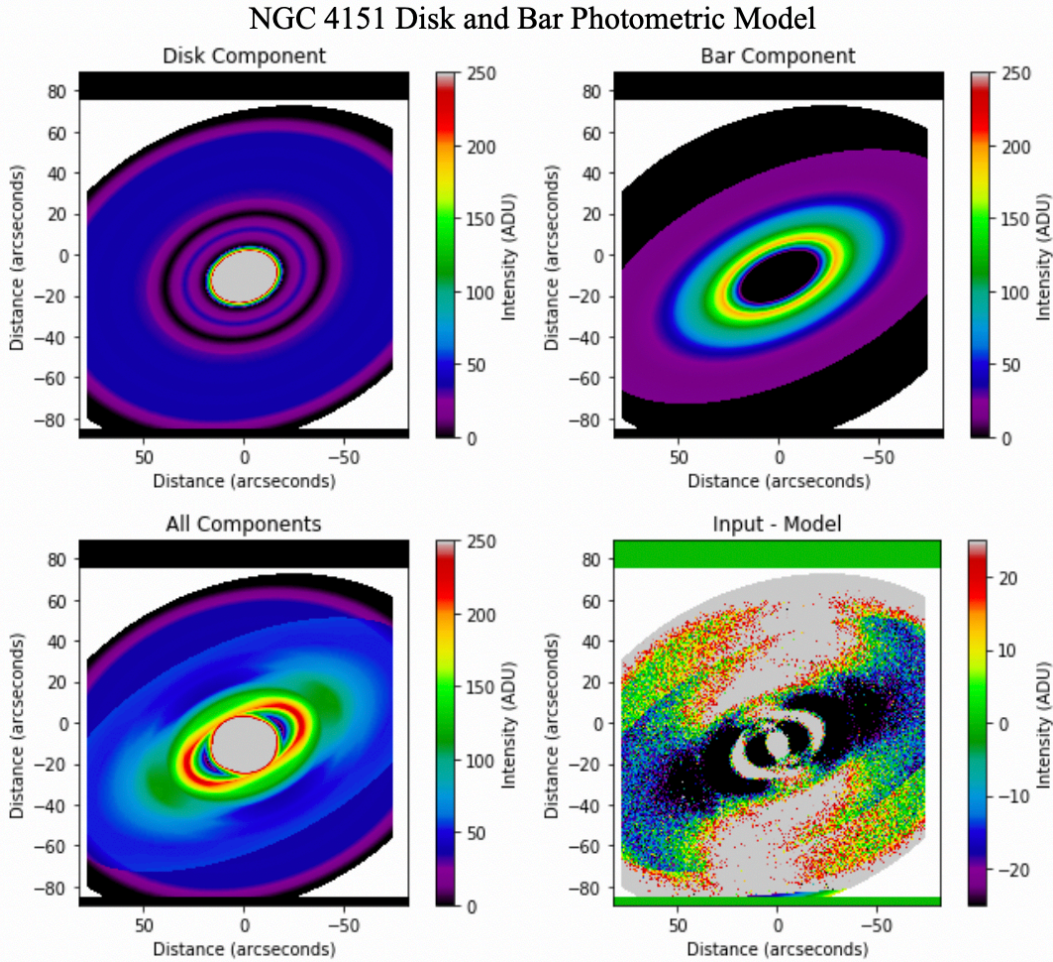
Figure 11: NGC 4151 P-D-B model. The top row shows the disk component and the bar component respectively. The bottom row shows the full P-D-B model (addition of both images from the top row) and residual image subracting model from the original image (top-left panel of Figure 2).

velocity due to each component added to the model, allowing us to produce models comparing

the shape and strength of each component. Plots separating the individual components of NGC

3516 are presented in Figure 14. The sum of the velocities from each spaxel in the disk (top-

right), the radial flow (bottom-left), and the tangential (bottom-middle) and radial (bottom-right)

components of the bar, in conjunction with the fit systemic velocity, found in Table 2, equals the

velocity attributed to each spaxel in the output model, as per Equation 2 in Section 4.1.

The model has a very strong rotational component caused by the disk, especially

compared to the strength of the radial flow. The bar is moderately strong in comparison to the

total rotational velocities, and the position angle of the disk and the tangential component of the

	Disk (K-D)	Disk and Bar (K-D-B)	Disk, Bar, and Radial Flow (K-D-B-RF)	Disk and Radial Flow (K-D-RF)	Warped Disk (K-wD)
PA_{disk} (°)	294.64 ± 1.84	296.42 ± 1.41	309.61 ± 8.34	305.38	298.89 ± 2.09
e_{disk}	0.07 ± 0.03	0.07 ± 0.01	0.08 ± 0.02	0.06 ± 0.01	0.07 ± 0.04
i_{disk}	21.92 ± 4.78	20.98 ± 2.33	23.20 ± 2.59	19.53 ± 0.99	20.98 ± 7.17
PA_{bar} (°) (disk)	…	74.01 ± 11.34	55.71 ± 19.99	…	…
PA_{Vmt} (°) (sky)	…	9.36	3.04	…	…
PA_{Vrt} (°) (sky)	…	281.44	277.54	…	…
m	0	1	1	0	0
r_{warp}	…	…	…	…	14.00 ± 2.16
e_{warp}	…	…	…	…	0.12
PA_{warp}	…	…	…	…	4.93
V_{sys}	5150.43 ± 2.23	5194.74 ± 13.69	5187.09 ± 8.23	5148.30 ± 2.16	5170.71
X^2	1.623497	1.022334	0.877307	1.441935	3.577744

Table 6: Kinematic data for the full set of models of NGC 5548. Refer to Table 2 for table description.

bar are nearly the same. According to kinematic models, the disk of NGC 3516 is ~30° inclined, giving HexPak a detailed view of its components from a nearly face-on perspective. The bar of NGC 3516 seems to display a X-shaped or S-shaped morphology and appears to buckle in the middle.

Observations of NGC 4151 support the best-fit to the K-D-B-RF *DiskFit* model. There is some evidence that NGC 4151 contains a "barlens", viewed as a big oval-shaped structure (Onken et al. 2014). Earlier research describes the bar as "fat" or possibly a misclassified central bulge (Mundell et al. 1999). Figure 15 displays the kinematically distinct substructure of NGC 4151. It reveals a very strong disk component. In comparison, the strength of the radial flow and bar are practically nonexistent. However, it appears the bar may be much stronger in the center with its magnitude decreasing outwards. The tangential bar component is more significant than the radial velocity component of the bar. As with NGC 3516, we see a near alignment between the position angles of the disk and the tangential component of the bar, meaning the disk and bar appear concentric and are generally positioned similarly. This is notable due to the known
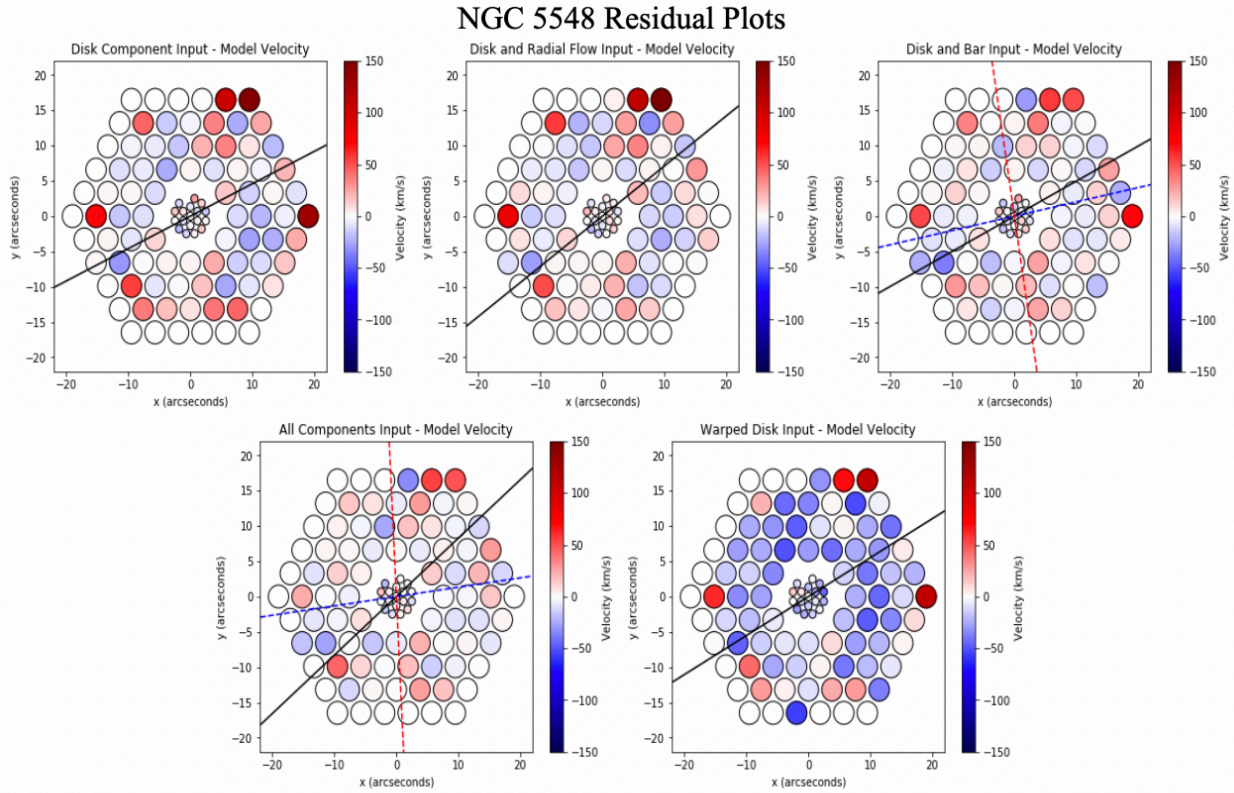
Figure 12: Hexpak residual plots for NGC 5548. Refer to Figure 5 for figure description.

degeneracy with modeling a bar component when the position angle of the bar is within ~10° of

either the disk major or minor axis (Barnes & Sellwood 2003; Holmes et al. 2015;

Randriamampandry et al. 2015; Sellwood & Sánchez 2010).

We have shown that the structure of NGC 5548 is much more complex than the other

galaxies in this sample (see Section 2 and Section 5.3). The disordered motion observed in the

velocity map of NGC 5548 confirms its messiness. While the classification and observations of

NGC 5548 do not include a bar, the *DiskFit* kinematic models presented in Section 5.3 finds

better agreement with input data when a bar is included. One possible explanation for the better

model fit with a bar component comes from recalling *DiskFit* models a bar component as

deviations from non-circular motion; it is conceivable that the detected non-circular motion is a

result of the warped nature of the disk. Furthermore, the kinematic effect of the major merger

event may result in non-circular motion or the warp features present in NGC 5548, which are not
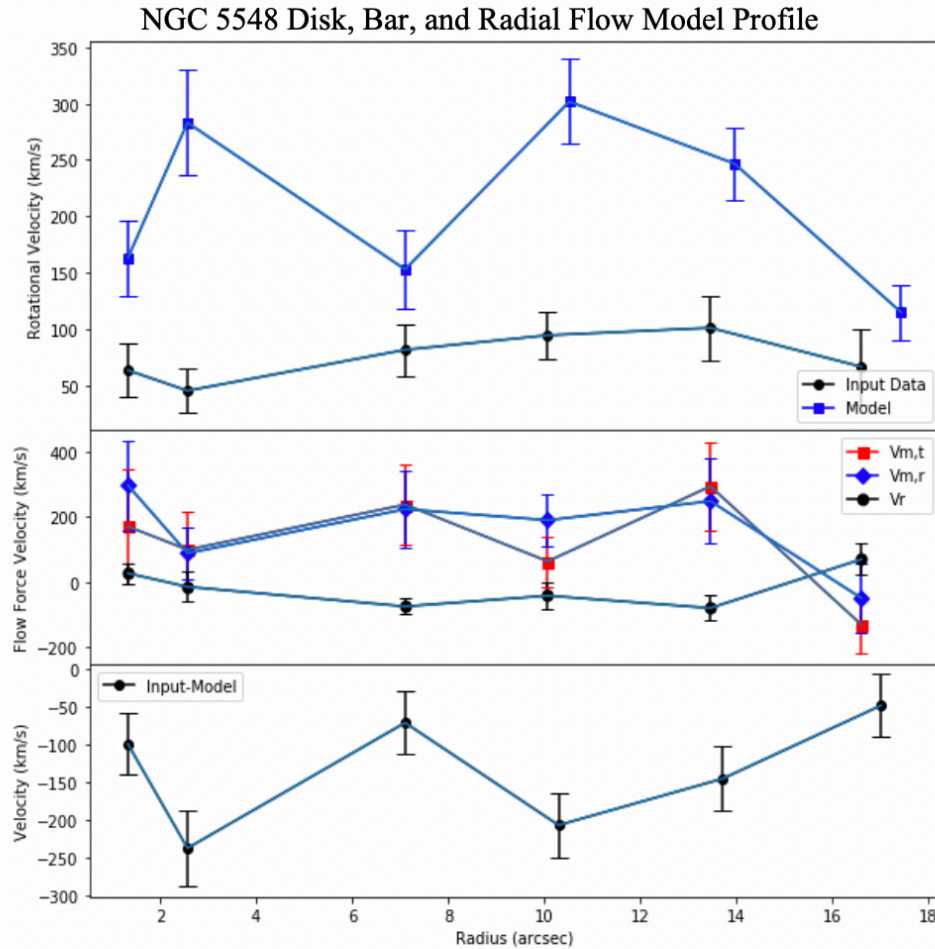
Figure 13: Best-fit (K-D-B-RF) kinematic model profile for NGC 5548. Refer to Figure 6 for figure description.

well represented by the warp assumptions made by *DiskFit*. The velocity maps for each component of NGC 5548 are displayed in Figure 16. Once again, we see a strong rotational disk component. *DiskFit* finds moderately strong contributions from radial flows and non-circular motion, potentially indicating a kinematic bar. The structure of the bar in Figure 16 for NGC 5548 is similar to an X-shaped or S-shaped morphology and appears to buckle in the middle, but with less strength than the bar in NGC 3516. However, the best-fitting K-D-B-RF model for NGC 5548 still contains large scale residuals and thus we cannot conclude anything certain about the shape or nature of the bar or noncircular motions in NGC 5548.
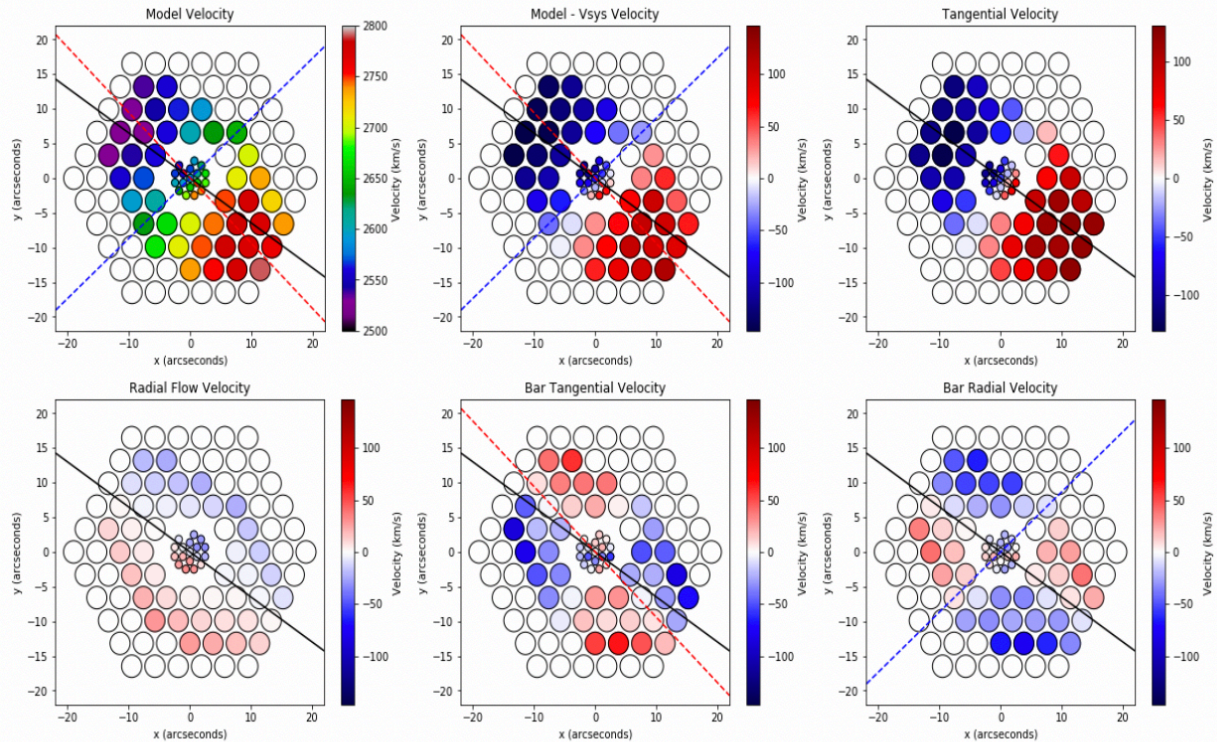
Figure 14: All panels display the best-fit (K-D-B-RF) model for NGC 3516. The solid black line denotes the position angle of the disk component in the sky plane. The dashed red and blue lines represent the position angles of the tangential and radial non-axisymmetric flow forces (or bar) respectively, also in the sky plane. From left to right the top row shows: the best-fit model of NGC 3516 produced by *DiskFit*; the systematic recessional velocity of the galaxy subtracted from the model velocity of each spaxel; the tangential velocity component only, representing the disk component rotation. The bottom row from left to right shows: the strength of the radial flow force; the strength of the tangential component of the bar; the strength of the radial component of the bar. Note: the sums of the tangential velocity of the disk, the radial flow force, and the tangential and radial components of the bar for each spaxel, and the systematic recessional velocity of NGC 3516, are equal to the model velocities (see Equations 1 and 2). See Figure A3 for an alternative graphic, smoothing the data values over the whole plot, rather than assigning one value to each spaxel.

Rather than assigning one value for the area of each spaxel, *Vorbin* is a program

developed to smooth plots with specific data values over the range of values using the signal and

noise of each spaxel. We include plots of the HexPak data using *Vorbin* in the appendix in

Figures A3, A4, and A4 for NGC 3516, NGC 4151, and NGC 5548 respectively.

6.1.2 Rotation Curve Offset Inquiry

The rotation curves presented in Figures 6, 9, and 13 all display the same issue of the

model velocity curve containing systematically higher values than the input data; this section
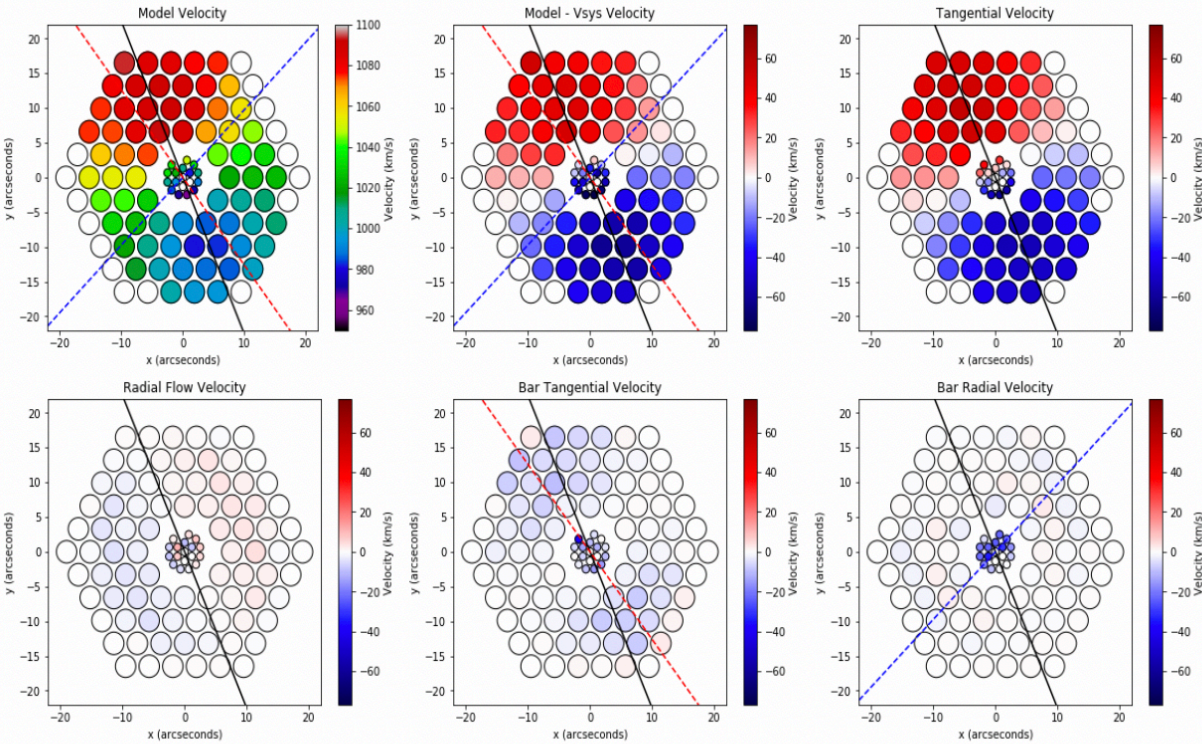
Figure 15: Best-fit (K-D-B-RF) model for NGC 4151. Refer to Figure 14 for figure description. See Figure A4 for an alternative graphic, smoothing the data values over the whole plot, rather than assigning one value to each spaxel.

will investigate why this offset occurring. Analysis of the rotation curves for all of the kinematic models for all of the galaxies show the same issue; the rotation curves output by *DiskFit* are systematically offset above than the input rotation curves. We wish to know whether this difference is real, in the sense that *DiskFit* is systematically over-estimating the recessional velocity at each point, or it is indicative of a fundamentally different method of calculating the rotation curve. Presumably, since it is a systematic overestimation issue for each model of all sample galaxies, *DiskFit* is overestimating the systemic recessional velocity for the galaxy.

Table 7 displays the median velocity value from the input velocity map, and the systemic recessional velocity computed by *DiskFit* in the minimization process. As mentioned throughout Section 5, for the set of best-fitting kinematic models for all three sample galaxies, all of the plots in Figure 17 support the conclusion that all of the sample galaxies have kinematically
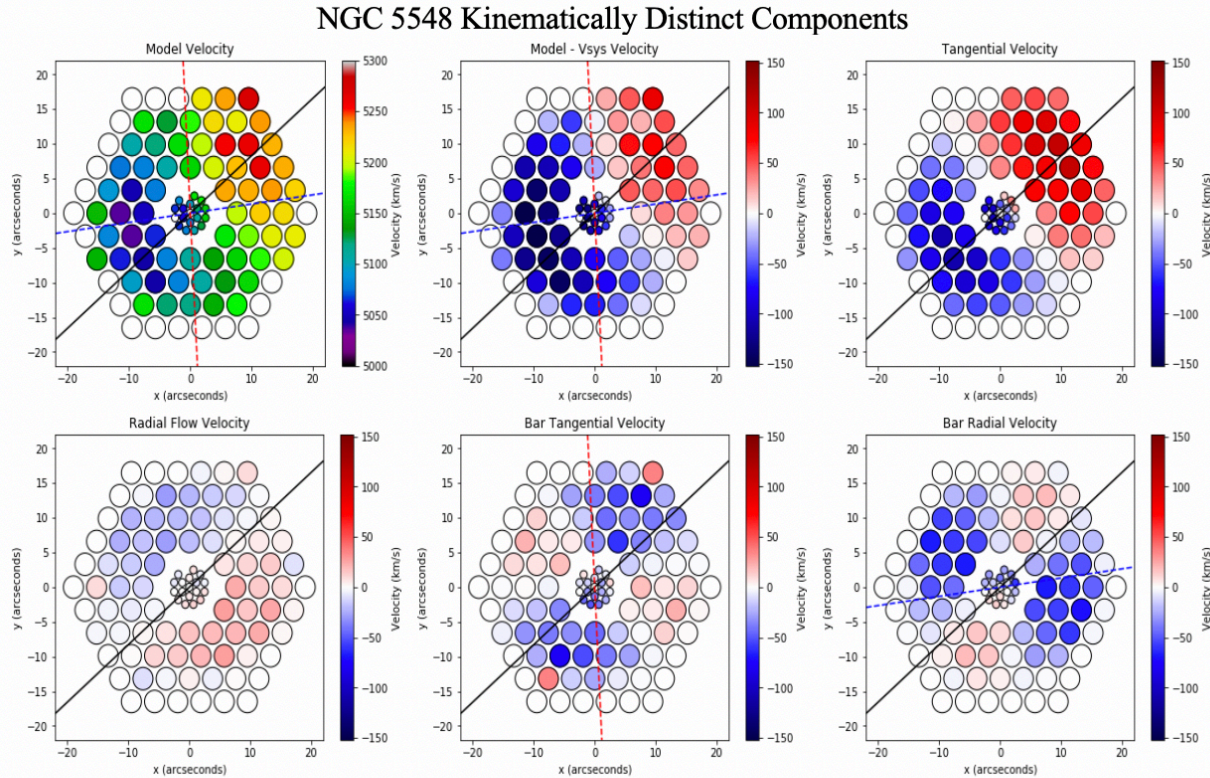
Figure 16: Best-fit (K-D-B-RF) model for NGC 5548. Refer to Figure 14 for figure description. See Figure A5 for an alternative graphic, smoothing the data values over the whole plot, rather than assigning one value to each spaxel.

distinct disk, bar (or other non-circular motion), and radial flow components. In all kinematic models, we see the recessional velocity computed by *DiskFit* is greater than the median value from the input data, confirming our recessional velocity overestimation hypothesis. Plots for the rotation curves for every kinematic model are shown in the left panels of Figure 17. One potential method to bring the rotation curves into alignment with the input rotation curve is to subtract a constant offset based on the difference between the input and model data. Initially we added just the difference (rather than the aforementioned multiple of the difference by two) between the velocities to bring the rotation curves into agreement, however this seemed to only roughly half the offset for all kinematic output rotation curves, possibly due to the effect of averaging two radii extending across the kinematic major axis. Instead, we chose to add two times the difference between the median input velocity and minimized output velocity from each

Kinematic Velocity Offsets			
Galaxy	Best-fit Model V_{sys}	Median V_{sys}	Median – Model
NGC 3516	2673.72	2630.32965	-43.39035
NGC 4151	1042.51	1035.004	-7.506
NGC 5548	5187.09	5152.2564	-34.8336

Table 7: Includes some values used to calculate rotation curves and offset rotation curves, for each galaxy. Median V_{sys} is the median recessional velocity from the input data from HexPak. Best-fit model V_{sys} is the systematic recessional velocity for the K-D-B-RF model output by *DiskFit*. Median – Model is the difference between the two. Note: when calculating all offset rotation curves, the V_{sys} from each model was used for subtraction from the median input velocity, rather than using the best-fit (K-D-B-RF) model V_{sys} for the recalculation of the rotation curves for different kinematic models of the same galaxy.

of the five possible kinematic models and all galaxies in the sample. Adding two times the difference between the velocities provided the best alignment between input and output rotation curves. The right column of Figure 17 shows the impact this has on bringing the output data into much better alignment with the input data.

While this brings the rotation curves into better agreement, it does not fully explain why the offset is present or if it possesses a physical meaning. Another possible cause of the issue with the output rotation curves from *DiskFit* could be a fundamental difference between the processes used to determine the rotational velocities at each radius, for the input and output data respectively. To investigate this issue, we homogenized the method for making the input and output rotation curves. For the input rotation curves we selected a two spaxel-wide slit across the kinematic major axis of the galaxy and used the average of the velocities with the same radius. The revised rotation curves we generated from the *DiskFit* output data used the same fibers as with the rotation curve for the input data. *DiskFit* does not describe the method used to calculate the rotation curve given in the output file in the documentation. Thus, the best way to compare results from input and output data is to homogenize the method used for calculation. Figure 18 presents the dramatic effect that homogenizing the method for creation of rotation curves has on bringing them into agreement. For all three sampled galaxies, the input and output rotation
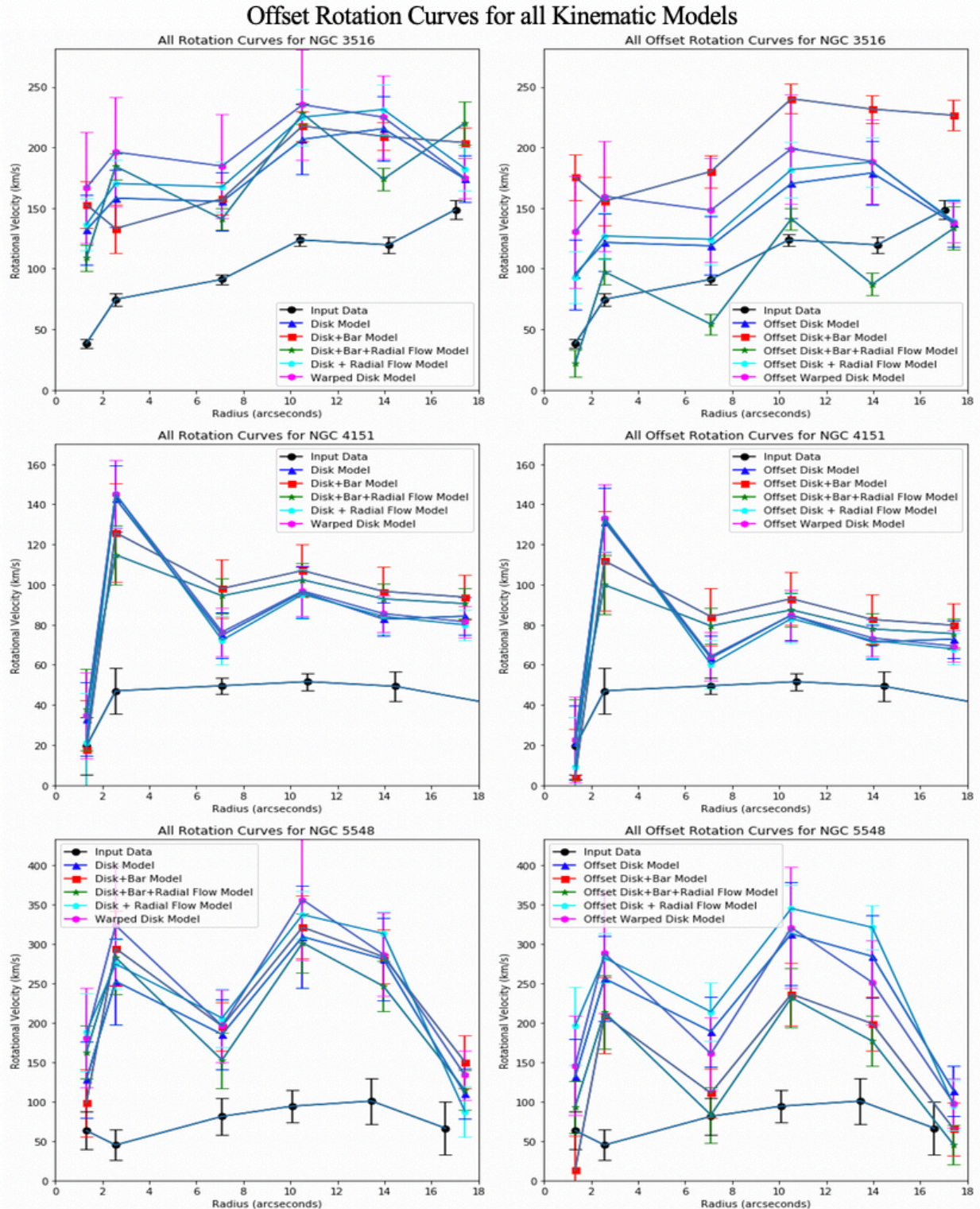
Figure 17: Rotation curves for all kinematic models. The rows, from top to bottom, are presented in the order of NGC 3516, NGC 4151, NGC 5548. Left column: input data curve alongside the curves for each of the possible kinematic *DiskFit* models. Right column: input data curve plotted against a revised version of the *DiskFit* output curve. Specifically, we added two times the difference between the median of the input velocities and the V_{sys} from each model to each point in the rotation curve.

curves show wonderful agreement. This highlights the importance of consistency in methods before comparing data. It is useful to note that the offset in rotational velocities shown Figures 6, 9, and 13 is *not* a physical difference but an artifact of the method *DiskFit* uses to produce the rotation curves.

6.2 Photometric Model Analysis

6.2.1 Distinct Photometric Structure

The best-fit model for NGC 3516 contains a disk, bar, and bulge component, which are all apparent in the HST image (see top-left panel of Figure 1). NGC 4151 has a disk and a weak bar classification, possibly a barlens, but the photometric model has trouble modeling a bar and fails to model a bulge completely. Included in the outputs from *DiskFit* are images of the modeled components individually. The contribution of each component, and other details of the model, are included in Figure 19. The limited photometric decompositons available for NGC 4151 were previously presented in Section 5.2.2.

Analysis of Figure 19 for NGC 3516 shows *DiskFit* is possibly not finding the correct disk position angle. Inspection of the HST image indicates the disk position angle to be ~45° but *DiskFit* converges on 183°. Many published papers report a degeneracy in the modeling employed by *DiskFit* when the bar is positioned within 10° from either the major or minor axis of the disk (Holmes et al. 2015; Lewis & Spekkens 2018; Randriamampandry et al. 2016; and references they contain). The best-fit kinematic model for NGC 3516 suggests the bar positioned is ~80° from the major axis of the disk, or ~10° from the disk minor axis, suggesting the discrepancy may be a result of this degeneracy. Other possible issues stem from large amounts of obscuring dust observed in NGC 3516, the intense AGN emission, and the large sprial arms or
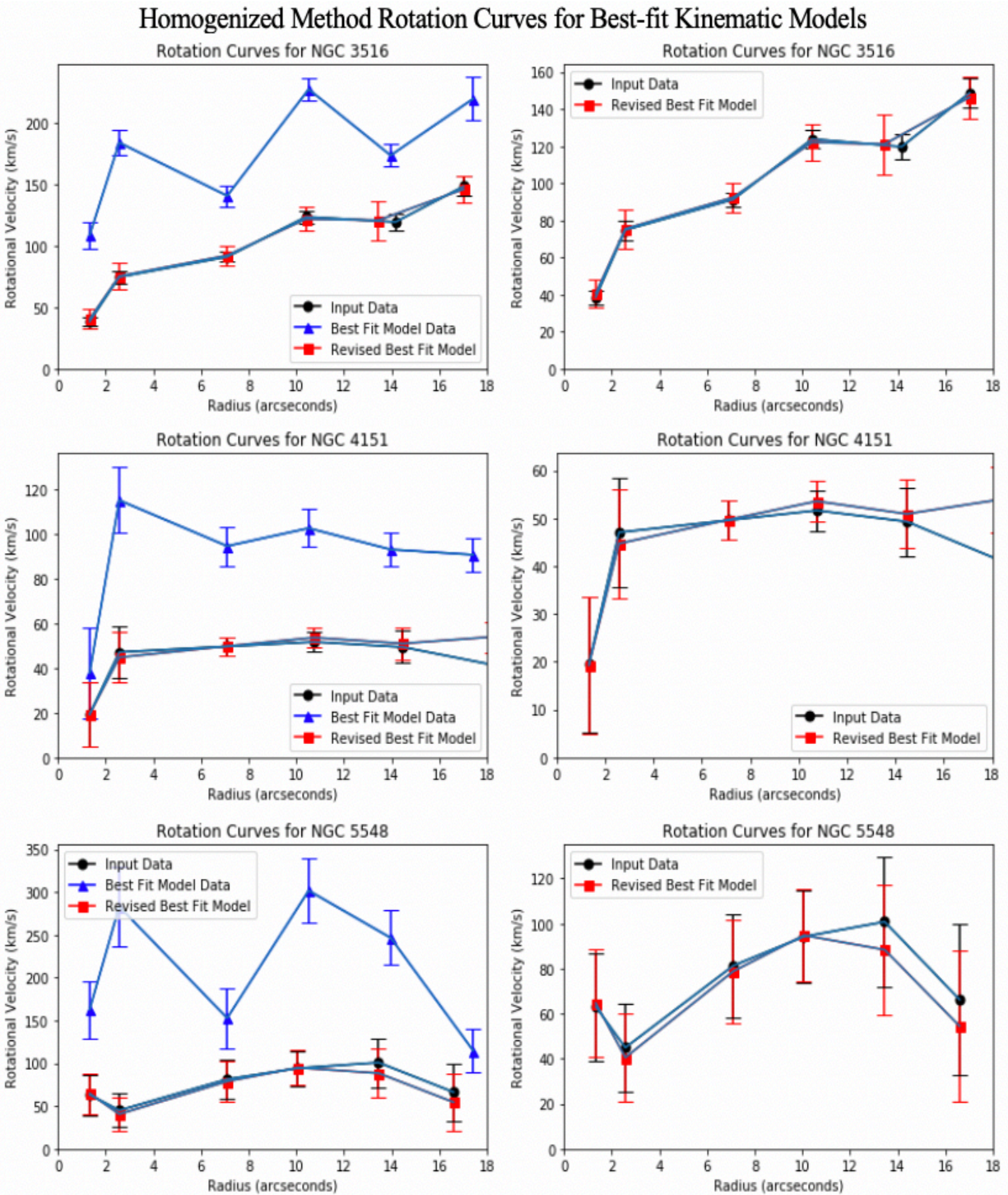
Figure 18: Rotation curves for best-fit kinematic models. The rows, from top to bottom, are presented in the order of NGC 3516, NGC 4151, NGC 5548. Left column: input data curve alongside the output and revised model output. Right column: input data curve plotted only against the revised model output. Output rotation curves were revised by homogenizing the method for their creation.

other non-axisymmetric features (Barbosa et al. 2006; Barnes & Sellwood 2003; Ferruit et al. 1998; Holmes et al. 2015).

6.2.2 Photometric Models at Different Fields of View

Considering the issues *DiskFit* had with globally fitting parameters for the disk, bar, and bulge components on such a large (~160"x160") field of view, specifically that the distinct photometric components output by *DiskFit* do not appear representative of its input HST image, or results published in literature (see Section 6.3), we decided to reduce the field of view used in the photometric modeling to ~41"x36", roughly the same as HexPak. Matching the field of view to HexPak eliminates field of view as a cause of difference between kinematic and photometric models. A table of best-fit values for the smaller field of view photometric models for NGC 3516 are presented in Table 8. Note that uncertainties for the non-best-fit models were not calculated due to the computation power available for this research. As with the large field of view, *DiskFit* finds the lowest X^2 value for a P-D-B-Blg model. The residual images (see Figure 20) of each of the models confirms the P-D-B-Blg model for the smaller field of view.

Images of each component, the complete model, and the residual of the best-fit P-D-B-Blg model for the reduced field of view is in Figure 21. The values contained in Table 8, for the smaller field of view present similarly to those in Table 3 for the full HST field of view. Riffel et al. (2017), hereafter R17, used *DiskFit* to study the inner 3" x 3" of a sample of AGN host galaxies and found agreement between small-scale kinematic modeling and large-scale photometric modeling. Agreement between photometric models for the two fields of view used for NGC 3516 further reinforce our estimates of the parameters of its components and selection of a P-D-B-Blg best-fit model. The agreement we find between modeling done at two fields of view is expected, based on conclusions from R17.
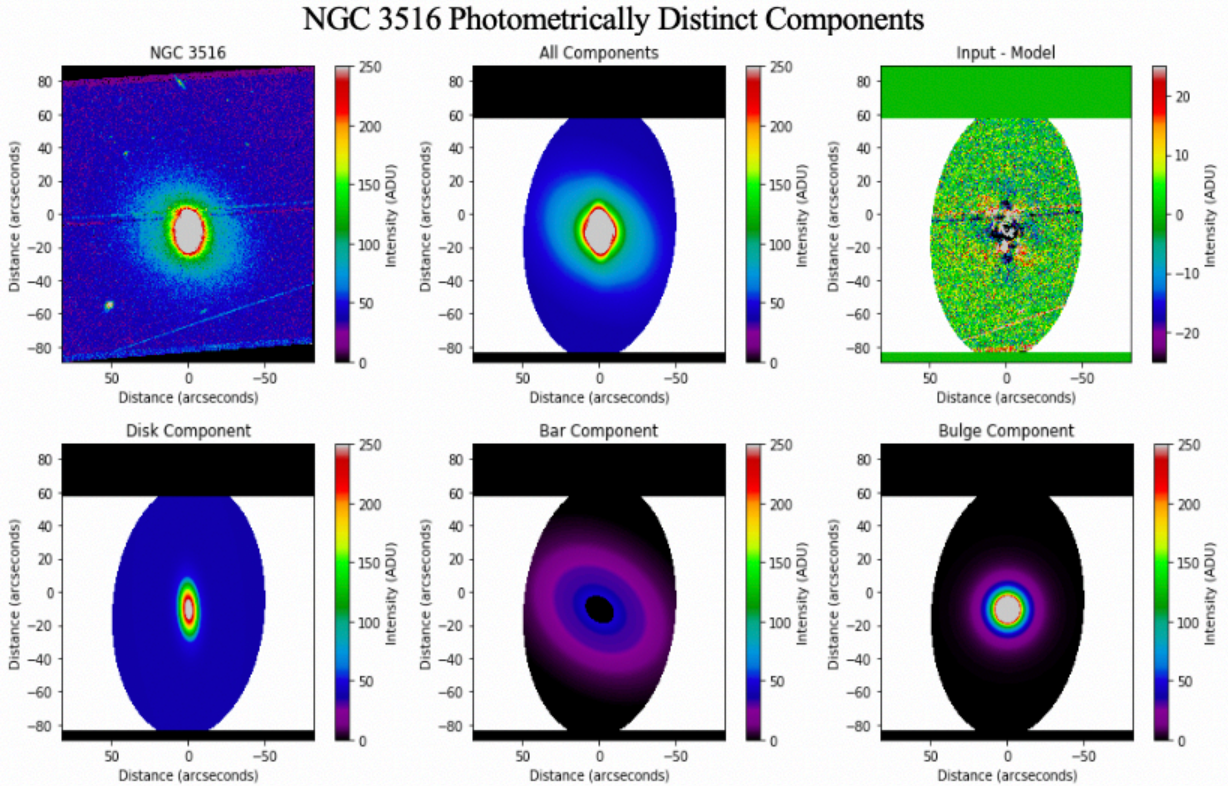
Figure 19: Best-fit (P-D-B-Blg) photometric model for NGC 3516. The top row from left to right shows: the HST WFC3 image of NGC 3516 (same as top left panel of Figure 1, but plotted with a different distance and color scale); the full P-D-B-Blg model; the model subtracted from the input HST image (residual image). The bottom row from left to right shows the individual contributions from the disk, bar, and bulge components respectively.

6.2.3 Bulge Region and Sérsic Index Analysis

Research by Lewis & Spekkens (2018) investigated the photometric analysis of *DiskFit* on 400 synthetic intermediate-inclination spiral galaxies containing Ferrers bars of various strengths. They showed that even when the Sérsic index is held fixed in *DiskFit*, at the true value, used to generate the light profile of the synthetic galaxy, the associated bulge parameters were not well recovered. Using a range of values to test the various capabilities of *DiskFit*, it was discovered that *DiskFit* photometry is unreliable in the bulge region. Since the analysis of Lewis & Spekkens used *DiskFit* on synthetic galaxies, they were able to absolutely determine that *DiskFit* does not perform well photometrically within the bulge. This directly impacts our ability to use *DiskFit* to accurately calculate r_e, which is essential in determinations of σ_*.

NGC 3516 Smaller Field of View Photometric Models				
	Disk (P-D)	Disk and Bar (P-D-B)	Disk and Bulge (P-D-Blg)	Disk, Bar, and Bulge (P-D-B-Blg)
PA_{disk} (°)	185.53	184.66	191.43	180.94 ± 1.14
e_{disk}	0.28	0.34	0.05	0.66 ± 0.01
i_{disk}	44.18	48.52	18.19	70.31 ± 0.42
PA_{bar} (°) (sky)	...	271.08	...	279.09 ± 50.72
PA_{bar} (°) (disk)	...	-2.38	...	-177.24
e_{bar}	...	0.79	...	0.42 ± 0.09
r_e (")	...	...	11.27	7.79 ± 0.63
I_{bulge} (ADU)	...	...	235.86	336.43 ± 36.06
n	...	...	4.20	3.98 ± 0.12
e_{bulge}	...	...	0.15	0.00 ± 0.01
Disk % light	100	96.16	9.38	9.74 ± 7.09
Bar % light	...	3.84	...	11.49 ± 3.82
Bulge % light	...	...	90.62	78.77 ± 3.41
X^2	72.608307	70.395256	24.856316	22.712332

Table 8: The full-set of photometric models using a ~41"x36" field of view. Refer to Table 3 for table description.

Figure 22 shows the radial intensity profiles for each component in NGC 3516 for two different fields of view. Analysis of both panels of Figure 22 shows the poor performance of *DiskFit* in the bulge region highlighted by how each component is attributed a very different light profile between different field of view modeling, specifically within the inner ~20" of the plot. Figure 23 shows the radial intensity plots for NGC 4151 for the two photometric models it was able to converge on (P-D and P-D-B models). These plots again show the inconsistency of the light profiles within the central region of the galaxy: *DiskFit* does not know which component to attribute the light to at each radius, especially in the bulge. Figure 22 and Figure 23 support the inaccuracy of the photometric modeling in the bulge region, found by Lewis & Spekkens (2018).

To further test the photometric decomposition, specifically within the bulge region, we held the Sérsic index at a fixed value, based on results determined by Be09. Using *Galfit*, NGC 3516 was determined to have both a bulge and an inner bulge (see Figure A6 for the *Galfit* models of the sample); as *DiskFit* can only fit a single bulge component, we used the average of
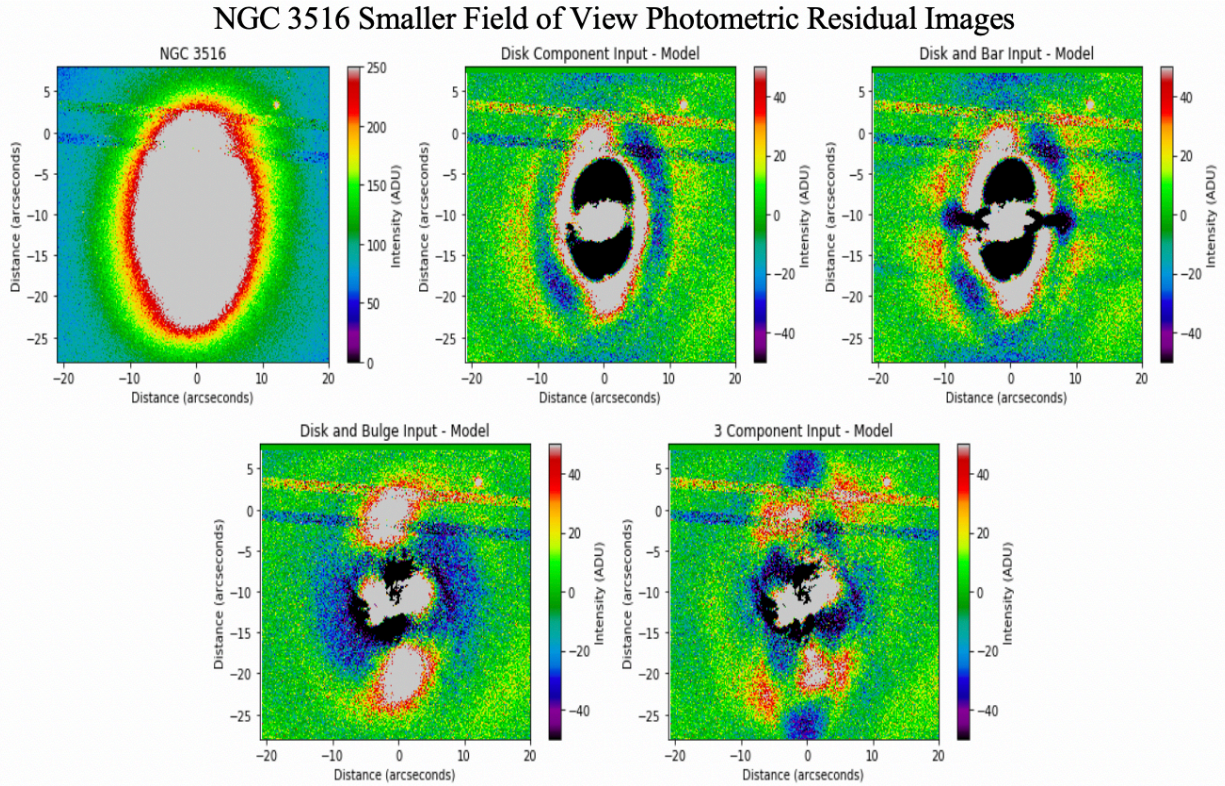
Figure 20: Residual photometric plots for NGC 3516 for a smaller field of view. Refer to Figure 7 for figure description.

the Sérsic indices from the two bulges. The X^2 value increases from ~6.3 to ~7.1 when modeling with all the same best-fit parameters and holding the Sérsic index at a fixed value. The increase of the X^2, coupled with worse agreement between the parameters presented in Table 3 and 8 and the output parameters of this fixed Sérsic n model, provide more evidence that the photometric modeling in the bulge region is not reliable.

6.3 Model Comparisons

6.3.1 Kinematic Models from Literature

DiskFit was used by R17 to model kinematics of the inner 3" x 3" region of NGC 3516 and NGC 5548. This research uses symmetrized velocity fields as inputs into *DiskFit* rather than immediately observed velocity fields as it supposes the observed velocity motion should be symmetric (see Section 8 for a discussion of possibly using symmetrized velocity fields in the future). R17 were specifically looking for disk rotation within their 16 AGN host galaxy sample,
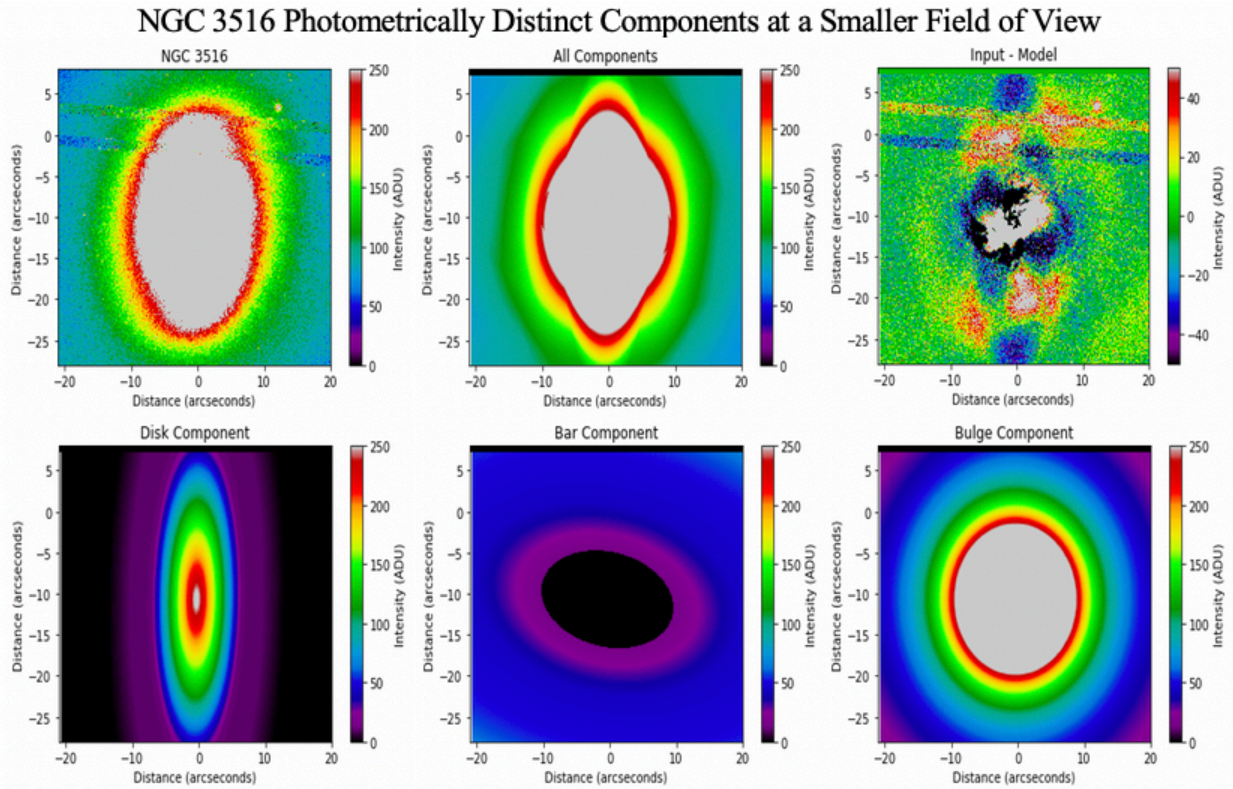
Figure 21: Best-fit (P-D-B-Blg) photometric model for NGC 3516 for a smaller (41" x 36") field of view. Refer to Figure 19 for figure description.

rather than attempting to determine best-fit models or account for non-circular motions. Even though R17 investigate only the inner 3" x 3" region as opposed to our ~41" x 36" field of view, the model velocity maps in R17, see Figures A7 and A8, for both NGC 3516 and NGC 5548 are similar to the maps presented in Figures 1, 3, 14, and 16, and the kinematic major axes show general alignment.

This study also presents values for disk ellipticity of NGC 3516 as 0.05±0.01 with disk inclination 18.2° and no other specific parameters provided. Our kinematics suggest the disk ellipticity is ~0.2 and photometry show disk ellipticity is ~0.06; however, Figure 1 clearly shows NGC 3516 is nearly face-on but photometry yields disk inclination ~60°, rather than the more reasonable ~30°, suggested by the kinematic modeling branch. The models presented in R17 indicate a much more circular disk component than our models presented in Table 9.
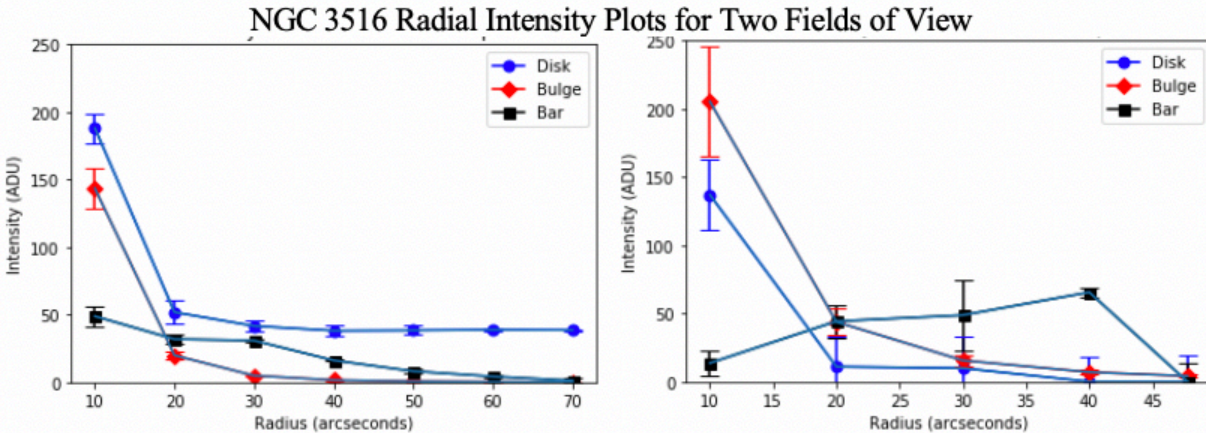
Figure 22: Radial intensity plots for best-fit (P-D-B-Blg) photometric model for NGC 3516. Left: output plot for the 164" x 179" field of view. Right: output plot for the 41" x 36" field of view.

Additionally, *DiskFit* finds a more face-on galaxy model in R17 compared to our model. R17 reports NGC 5548 model parameters include a disk ellipticity of 0.51 inclined to the plane at 60.9° whereas here we present a much more circular (eccentricity ~0.05) and face-on (inclination ~20°) disk. R17 suggests their kinematic modeling results and large-scale photometric results generally agree for the 16 galaxies in their sample. However, they note discrepancies specifically with NGC 3516 and NGC 5548. For NGC 5548, the model variations were attributed to it being too face-on, however, we find a more realistic disk inclination and find consistency for five variations with different component combinations. For NGC 3516, the model breakdown comes from potential alignment of the disk and bar major axes. This alignment is confirmed from the values presented in Table 9. Holmes et al. (2015) reports degeneration in the modeling abilities of *DiskFit*, for either branch of modeling, when the position angle of the bar is within ~10° from either the major or minor axis of the disk component, due to inability to decompose motions.

R17 further provides rotation curves for NGC 3516 and NGC 5548 (see figure A9). Rotation curves here were generated from a pseudo-slit across the input, non-symmetrized, velocity field. While we can only use these rotation curves to compare with the inner 3" of rotation curves presented here, the general trend and size of the two rotation curves seem to be in
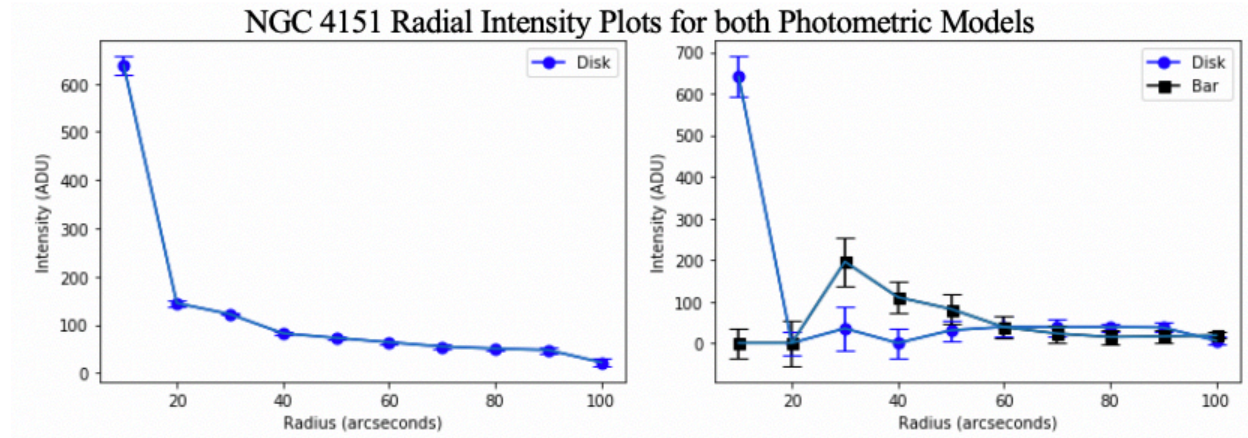
Figure 23: Radial intensity plots for two NGC 4151 models. Left: output plot the P-D model. Right: output plot for the P-D-B model.

good agreement. There does not appear to be any systematic difference in the rotation curves presented in R17 compared to those presented here. R17 does not provide details of the rotation curves immediately output by *DiskFit*.

The kinematic models pulled from literature for comparison include a rotation curve of NGC 3516 from Cherepashchuk et al. (2010) and Riffel et al. (2017) and for NGC 4151 from Mundell et al. (1999). The rotation curve for NGC 3516 shows dots for observed velocities and contains error bars from their calculations for the potential offset of non-circular motion (see Figure A10). The rotation curve for the K-D-B-RF model of NGC 3516 fits the trend of the curve presented by Cherepashchuk et al. (2010) very well in both shape and size of velocities. Mundell et al. (1999) present a rotation curve for NGC 4151, included in Figure A11 for comparison, obtained from observations of neutral hydrogen gas. As with NGC 3516 before, the best-fit K-D-B-RF model rotation curve for NGC 4151 (see Figure 9) is in good agreement with the neutral hydrogen rotation curve, included in Figure A11 for comparison.

Iannuzzi & Athanassoula (2015) simulated models of boxy/peanut bulges at various inclinations, orientations, strengths, and how they affect the observed kinematic

signatures, both with one and two-dimensional trends. They estimate 45% of disk galaxies contain a boxy/peanut bulge, containing similar light profile to a bar and much weaker strength. The structure of the bar for NGC 4151 from Figure 15 is similar to kinematic signatures of simulated boxy/peanut bulges (see images from simulations in Figure A12). Other research (Laurikainen et al. 2014) has shown that boxy/peanut bulges viewed at low inclinations (nearly face-on) cause the apparent barlens structure noted by Onken et al. (2014). This suggests we are seeing the kinematic signature of the barlens identified by classification for NGC 4151.

In general, the kinematics of all three sample galaxies seem to be well represented by *DiskFit* modeling, shown by agreement between data presented here and those published in literature. The agreement between these models comes from directly comparing model velocity maps and rotation curves.

6.3.2 Photometric Models from Literature

DiskFit photometric models for NGC 3516 and NGC 4151 photometry were compared to *Galfit* models from Be09. Table A2 summarizes the best-fit model parameters for these galaxies, and additionally NGC 5548, since this table contains values used as estimates for *DiskFit* inputs. At first glance it is surprising that *Galfit* did not find a best-fit model with a bar component considering it is strong photometric bar. Be09 justify the classifications of inner bulges as being possible bars or pseudo-bulges, because use of only photometric data does not detect, and inhibits analysis of, the non-circular motions and a physical distinction cannot be made. The inner-bulge components listed could be shown to be bars with the kinematic data employed here. *Galfit* allows for the addition of a point spread function (PSF) to account for the AGN emission and multiple concentric components, such as the three bulges used to model NGC 4151. In

contrast, *DiskFit* is only capable of modeling a single component of each type and has no PSF function, so these differences are a matter of the modeling program employed.

In the case of both NGC 3516 and NGC 4151, *DiskFit* found the Sérsic index for the bulge to be much larger than *Galfit*. The poor photometric performance of *DiskFit* in the bulge region is a potential explanation for this discrepancy. Bentz & Manne-Nicholas (2018) suggest that Sérsic index values greater than one typically indicate a bulge component, values less one than typically indicate a bar, and values between one and two could represent a pseudo-bulge, or potentially a boxy/peanut bulge. Most of the Sérsic index values for the components determined by *Galfit* imply pseudo-bulges. Confirmation of the barlens classification of NGC 4151 is evident when considering *Galfit* found indices of 4.29, 0.71, and 0.81 for the three bulge components respectively, and knowledge of the Sérsic index implication on typical morphological classification.

There is some scatter in the size of the measured ellipticities of each component determined by *DiskFit* and *Galfit*. These differences likely stem from the method by which each algorithm searches for distinct photometric components, and from differences in the minimization algorithms employed. Furthermore, we know *DiskFit* has trouble distinguishing components, for both kinematics and photometry, when the position angle of the bar is within ~10° from either the major or minor axis of the disk component (Barnes & Sellwood 2003; Holmes et al. 2015; Randriamampandry et al. 2015; Sellwood & Sánchez 2010). In the case of NGC 3516, the kinematic models indicate the bar is ~10° from the major axis of the disk, suggesting issues with NGC 3516 stem from this deficiency. The inner-bulge found for NGC 4151, from Be09, with Sersic index of 4.29 corresponds to an intermediate ellipticity of ~0.46 suggesting this inner-bulge is a bar. While this bar has an intermediate, possibly bar-like,

ellipticity, remembering bars have Sérsic index $n < 1$ and bugles typically contain $n < 1$ suggests this component has mixed bar and bulge classifications. This is possibly another indication of the barlens induced by a boxy/peanut bulge.

6.3.3 Agreement Between Kinematics and Photometry

Before directly comparing kinematic and photometric models with different fields of view, we compared photometric models at two fields of view. Analysis of this (see section 6.2.2) suggested our photometric models at both fields of view generally showed agreement with parameters. As the X^2 value of the smaller field of view is generally worse and a large field of view encompasses more of the data available for the galaxy, we suggest the larger field of view models are more robust. Table 9 and 10 contain the parameters associated with the best-fit models for *DiskFit* kinematics and photometry for NGC 3516 and NGC 4151 respectively.

Both Table 9 and 10 show general disagreement in comparable parameters, between the best-fitting kinematic and photometric models. In general, the most significant disagreement is in the position angles and ellipticities of the disk and bar components. *DiskFit* photometric modeling assumes the disk and bar differ noticeably in position angles and ellipticities, and thus there is a degeneracy when the position angle of the bar is close to that of the major or minor axis of the disk (Barnes & Sellwood 2003; Holmes et al. 2015; Randriamampandry et al. 2015; Sellwood & Sánchez 2010). Kinematic data from NGC 3516 and NGC 4151 both suggests a small offset between the position angle of the disk and bar components, which causes error in the photometric modeling. Since the kinematic modeling parameters show better agreement with results from literature than the photometric modeling counterpart, we suggest that the kinematic modeling is a more accurate and consistently reliable.

6.3.4 Gauss-Hermite Moment Trends

	Photometry		Kinematics
NGC 3516 All Best-fit Models	Large Field of View (164" x 179") (P-D-B-Blg)	Small Field of View (41" x 36") (P-D-B-Blg)	Small Field of View (41" x 36") (K-D-B-RF)
PA_{disk} (°)	183.43 ± 0.55	180.94 ± 1.14	237.03 ± 3.27
e_{disk}	0.59 ± 0.02	0.66 ± 0.01	0.21 ± 0.02
i_{disk}	66.08 ± 1.22	70.31 ± 0.42	37.54 ± 1.69
PA_{bar} (°) (sky)	57.25 ± 2.38	279.09 ± 50.72	...
PA_{bar} (°) (disk)	-16.52	-177.24	77.07 ± 7.24
PA_{Vmt} (°) (sky)	...	...	310.89
PA_{Vrt} (°) (sky)	...	...	226.72
e_{bar}	0.26 ± 0.01	0.42 ± 0.09	...
m	...	...	1
r_e (")	4.45 ± 0.16	7.79 ± 0.63	...
I_{bulge} (ADU)	841.45 ± 52.31	336.43 ± 36.06	...
n	2.80 ± 0.05	3.98 ± 0.12	...
e_{bulge}	0.00 ± 0.00	0.00 ± 0.01	...
Disk % light	52.25 ± 2.75	9.74 ± 7.09	...
Bar % light	14.80 ± 1.63	11.49 ± 3.82	...
Bulge % light	32.95 ± 0.47	78.77 ± 3.41	...
V_{sys}	...	...	2673.72 ± 11.55
X^2	6.297995	22.712332	0.412983

Table 9: Parameters for best-fit kinematic and photometric *DiskFit* models of NGC 3516. Refer to Tables 2 and 3 for a description of the model parameters in the left-most column.

Using a similar kinematic *DiskFit* modeling process, R17 found an inverse correlation between recessional velocity and h_3 (hereafter V-h_3 correlation) in their sample. This study also suggests that locations with high velocity dispersion show similar trends in the same location on h_4 maps. The first four Gauss-Hermite moments, in order, represent the recessional velocity, velocity dispersion, the asymmetric deviations from a Gaussian, h_3, and the symmetric deviations from a Gaussian, h_4. The third Gauss-Hermite moment, h_3, represents the amount of right or left skew in the observed spectrum compared to a Gaussian while the fourth Gauss-Hermite moment, h_4, represents a measure of how 'peaky' the observed spectrum is relative to a Gaussian.

Figures 1-3 show the HexPak plots of four Gauss-Hermite moments for the line-of-sight velocity distribution. NGC 3516 shows a strong V-h_3 correlation. This V-h_3 correlation is also identifiable for NGC 4151 but slightly weaker; NGC 5548 possibly has a weak V-h_3 correlation.

NGC 4151 All Best-fit Models		
	Photometry	Kinematics
	Large Field of View (164" x 179") (P-D-B)	Small Field of View (41" x 36") (K-D-B-RF)
PA_{disk} (°)	107.03 ±14.10	23.99 ± 2.05
e_{disk}	0.26 ± 0.07	0.16 ± 0.03
i_{disk}	42.03 ± 6.20	33.10 ± 3.66
PA_{bar} (°) (sky)	115.09 ± 12.95	...
PA_{bar} (°) (disk)	-79.21	17.13 ± 13.05
PA_{Vmt} (°) (sky)	...	38.46
PA_{Vrt} (°) (sky)	...	-45.82
e_{bar}	0.50 ±0.09	...
m	...	1
r_e (")	...	...
I_{bulge} (ADU)	...	...
n	...	...
e_{bulge}	...	...
Disk % light	59.73 ±12.25	...
Bar % light	40.27 ± 16.48	...
Bulge % light	...	...
V_{sys}	...	1042.51 ± 1.43
X^2	352.677979	0.251974

Table 10: Parameters for best-fit kinematic and photometric *DiskFit* models of NGC 4151. Refer to Tables 2 and 3 for a description of the model parameters in the left-most column.

Simulations of boxy/peanut bulges at various inclinations show this type of morphological component could be indicated by patterns in h_3 and h_4. Iannuzzi & Athanassoula (2015) use these simulations to show all boxy/peanut bulges display a V-h_3 correlation, and predict this correlation is more impactful in boxy/peanut bulges than for regular bars. These simulations also show an increase in this observed V-h_3 correlation, with increasing boxy/peanut bulge strength. Iannuzzi & Athanassoula (2015) also suggest both bars and boxy/peanut bulges show two negative minima for h_4 data along the kinematic major axis, however boxy/peanut bulges cause deeper minima. This paper concludes boxy/peanut bulges cause some features in h_3 and h_4 that cannot be explained by a normal bar or non-circular motion. Simulations of surface brightness and all smooth maps of all four Gauss-Hermite moments for boxy/peanut bulge galaxies at various inclinations from Iannuzzi & Athanassoula (2015) can be found in Figure A12. Additionally,

from this paper, one-dimensional major axis kinematic signatures of four different boxy/peanut

bulge simulations, for the four Gauss-Hermite moments, are located in Figure A13.

Figure 24 presents one-dimensional major axis trends for all Gauss-Hermite moments for

each sample galaxy. Section 6.1.2 details the process used to generate input rotation curves using

a two spaxel-wide slit across the observed kinematic major axis for the HexPak map. To obtain

one-dimensional major axis plots for NGC 3516, NGC 4151, and NGC 5548 we utilized the

same spaxels, and adapted the method for generating rotation curves to account for both positive

and negative radii. Positive radii were assigned to the receding side of the galaxy; but since

galaxy rotation should be symmetric, flipping the convention employed here would result in a

reflection about the y-axis.

The left panel of Figure 24 shows NGC 3516 contains a double minima structure for h_4,

possibly hinting at a boxy/peanut bulge classification. Be09 presents an inner bulge for NGC

3516 with a Sérsic index between one and two, suggesting this is a pseudo bulge, and a bulge

component with a Sérsic index less than one suggesting this is misclassified and represents bar

structure. The Sérsic index values for the two bulge components, coupled with the double

minima structure for h_4 data, may suggest a boxy/peanut bulge in NGC 3516. The middle panel

of Figure 24 shows NGC 4151 potentially contains double minima structure for h_4 data although

the structure is not as tight with those shown in Figure A13. *Galfit* models from Be09 find three

bulge components for NGC 4151; the innermost bulge has a Sérsic index greater than four while

the two outer bulges have Sérsic index less than one. The innermost bulge for NGC 4151 is

likely a more classical bulge than the two pseudo bulges that surround it. The indication of a

pseudo bulge from the Sérsic indices, the observation of a barlens in NGC 4151, and the double
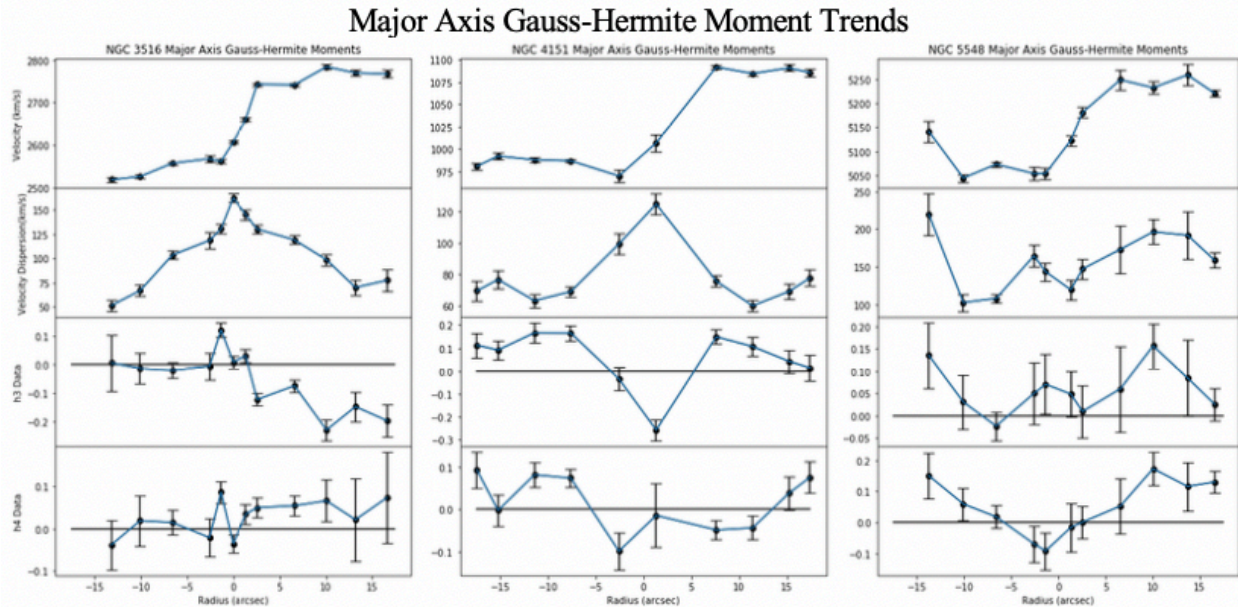
Figure 24: Gauss-Hermite moments along the disk major axis output by *DiskFit* for and each galaxy. From left to right the panels show: NGC 3516; NGC 4151; NGC 5548. From top to bottom each panel shows: recessional velocity; velocity dispersion; h_3 data; h_4 data.

minima structure for h_4 data provide sufficient evidence to confirm the barlens is likely attributed to the presence of boxy/peanut bulge.

7. Conclusions

In this paper we dissect the substructure within three nearly face-on, AGN host, disk galaxies with varying morphological classifications: NGC 3516, NGC 4151, NGC 5548. We use kinematic velocity maps from the HexPak IFU and photometric images from the HST WFC3 in *DiskFit* modeling in order to determine distinct structure in each galaxy.

Kinematically, all three sample galaxies were modeled best with disk, bar, and radial flow components, demonstrated goodness of model fit to data. Non-axisymmetric motion, or bar-like flow motion, was observed and analyzed for all three sample galaxies: NGC 3516 showed non-circular motion caused by its strong and photometrically observable bar component, NGC 4151 contained small non-circular motions related to its weak bar or barlens classification, and the motion present in NGC 5548 is expected to be due to observational evidence of a violent

merger. In all cases, the K-wD model produces unrealistic, and often nonphysical, parameters. Results from literature agree with the output model parameters for NGC 3516 and NGC 5548 presented in this paper.

Rotation curves from the output of *DiskFit* and results from literature obtained for these galaxies are similar and provide evidence for agreement between them. In general, the output rotation curves by *DiskFit* contain a systematic increase in velocity values than for a rotation curve obtained from a one-dimension slit across the disk major axis of rotation. Using the same rotation curve approach for input and output data, we show near perfect alignment between rotation curves. We conclude that this offset is not physical, but instead an artifact of the method used to calculate rotational velocities for each radius.

High resolution photometry images require large amounts of time and computer processing speed, possibly ruling out implementation of large photometric samples with *DiskFit* without an automated process or sufficient available computation power. Models of NGC 3516 presented show clear disk, bar, and bulge components which are confirmed by classifications and results in the literature. NGC 4151 contains a weak bar, likely attributed to a boxy/peanut bulge or a barlens, causing *DiskFit* to fail when searching for a photometrically weak bar.

Modeling photometry within two different fields of view for NGC 3516 shows scatter in model parameters determined by *DiskFit*. Detailed analysis of the models from both fields of view, and additional models created to test the Sérsic index value, shows *DiskFit* is not particularly reliable in the bulge region. Since *DiskFit* does not accurately determine the Sérsic index of the bulge component, it also insufficiently reports the bulge effective radius as well.

In both branches of DiskFit modeling there is degeneracy when the bar position angle is within ~10° of either the major or minor axis of the disk. Models of NGC 3516 and NGC 4151

show the disk and bar are close to the zone of degeneracy. Comparison of both types of models with results from the literature show more consistency in kinematic modeling than photometric modeling. Accordingly, we suggest DiskFit kinematic modeling is more reliable than its photometric counterpart, at least for this sample of galaxies.

The barlens structure observed in NGC 4151 is likely produced by a boxy/peanut bulge. The kinematic maps for the non-circular motions are similar to signatures of boxy/peanut bulges from simulations. Other evidence for this morphological structure in NGC 4151 (found in Figure 1) is an inverse correlation between recessional velocity and h_3, and 2) the negative double minimum for h_4, observed on a one-dimensional cut along the kinematic major axis. NGC 3516 does not seem to contain a typical bulge component, based on its low Sérsic index, strong inverse V-h_3 correlation, and the presence of a negative double h_4 minimum. However, lack of observational evidence for a boxy/peanut bulge suggest these features may rather be indicative of some other special morphology related to the bar or bulge of NGC 3516.

8. Future Work

As mentioned in the Introduction, accurate determinations of r_e are critical for measurements of bulge stellar velocity dispersion σ_*. Also, the calibration of the M_{BH}-σ_* relation is fundamental in current determinations of the scale factor f for reverberation mapping. There is a need to understand the effects of the bar or other morphological components on measured σ_*; the specific geometry of the components may also effect σ_*.

Rotating disk models theoretically should be symmetric and symmetrizing the input velocity fields could be useful, if accurate. Rather than immediately providing velocity fields into *DiskFit*, R17 first symmetrized the data before using the velocity map as an input. Since IFS typically suffers issues with signal to noise ratio, causing error in data, symmetrizing the input

velocity maps could reduce error in the input and allow *DiskFit* to produce a better model. Further inquiry into the benefits and drawbacks of symmetrized velocity maps is necessary to better understand the nature of symmetric and non-axisymmetric motion within a galaxy.

      DiskFit is a great tool for analyzing two types of data with the same algorithm but proves to be incredibly time-intensive, especially for high resolution modeling. In order to best probe galaxy morphology, and its effect on σ_*, larger sample sizes should be employed. To prevent time-wasting from repetitive selection of best-fit models, it would be best to create an automated process to parse through the increase in data more efficiently.

      Using an automated system with a large sample size (selected with a large variety of morphological classifications, geometries, and strengths) will help determine how these physical components induce trends with the Gauss-Hermite moments, specifically velocity dispersion. Furthermore, a separation of bulge kinematics would be incredibly useful, however, it is unclear if *DiskFit* will be able to determine the motion of stars within this region in the context of the modeling system it already employs for kinematics.

References

"A Code for Modeling Asymmetries in Disk Galaxies." 2019. *DiskFit*. Queen's University. Accessed June 3. https://www.physics.queensu.ca/Astro/people/Kristine_Spekkens/diskfit/.

Arribas, S., E. Mediavilla, B. Garcia-Lorenzo, and C. Del Burgo. 1997. "Stellar and Ionized-Gas Kinematics of the Seyfert 1 Galaxy NGC 3516." *The Astrophysical Journal* 490 (1): 227–37. doi:10.1086/304849.

Barbosa, F. K. B., T. Storchi-Bergmann, R. Cid Fernandes, Cláudia Winge, and H. Schmitt. 2006. "Gemini/GMOS Integral Field Unit Stellar Kinematics of the Nuclear Region of Six Nearby Active Galaxies." *Monthly Notices of the Royal Astronomical Society* 371 (1): 170–84. doi:10.1111/j.1365-2966.2006.10690.x.

Barnes, Eric I., and J. A. Sellwood. 2003. "Uncertainties in Spiral Galaxy Projection Parameters." *The Astronomical Journal* 125 (3): 1164–76. doi:10.1086/346142.

Batiste, Merida, Misty C. Bentz, Emily R. Manne-Nicholas, Christopher A. Onken, and Matthew A. Bershady. 2017. "The BRAVE Program. I. Improved Bulge Stellar Velocity Dispersion Estimates for a Sample of Active Galaxies." *The Astrophysical Journal* Volume 835, Issue 2, article id. 271, 11 pp. doi:10.3847/1538-4357/835/2/271.

Batiste, Merida, Misty C. Bentz, Sandra I. Raimundo, Marianne Vestergaard, and Christopher A. Onken. 2017. "Recalibration of TheMBH–σ⋆Relation for AGN." *The Astrophysical* Volume 838, Issue 1, article id. L10, 6 pp. doi:10.3847/2041-8213/aa6571.

Begeman, K. G. 1987. "HI Rotation Curves of Spiral Galaxies." *Ph.D. thesis, Kapteyn Institute*.

Bentz, Misty C. 2016. "AGN Reverberation Mapping." *Astronomy at High Angular Resolution Astrophysics and Space Science Library* 439 (August): 249–66. doi:10.1007/978-3-319-39739-9_13.

Bentz, Misty C., Bradley M. Peterson, Hagai Netzer, Richard W. Pogge, and Marianne Vestergaard. 2009. "THE RADIUS-LUMINOSITY RELATIONSHIP FOR ACTIVE GALACTIC NUCLEI: THE EFFECT OF HOST-GALAXY STARLIGHT ON LUMINOSITY MEASUREMENTS. II. THE FULL SAMPLE OF REVERBERATION-MAPPED AGNs." *The Astrophysical Journal* 697 (1): 160–81. doi:10.1088/0004-637x/697/1/160.

Bentz, Misty C., Kelly D. Denney, Catherine J. Grier, Aaron J. Barth, Bradley M. Peterson, Marianne Vestergaard, Vardha N. Bennert, et al. 2013. "The Low-Luminosity End Of The Radius-Luminosity Relationship For Active Galactic Nuclei." *The Astrophysical Journal* Volume 767, Issue 2, article id. 149, 27 pp. doi:10.1088/0004-637x/767/2/149.

Bentz, Misty C., and Emily Manne-Nicholas. 2018. "Black Hole–Galaxy Scaling Relationships for Active Galactic Nuclei with Reverberation Masses." *The Astrophysical Journal* Volume 864, Issue 2, article id. 146, 19 pp. doi:10.3847/1538-4357/aad808.

Cappellari, Michele. 2020. "Michele Cappellari Python and IDL Programs." *Michele Cappellari*. Accessed March 6. https://www-astro.physics.ox.ac.uk/~mxc/software/.

Cappellari, M., and Y. Copin. 2003. "Adaptive Spatial Binning of Integral-Field Spectroscopic Data Using Voronoi Tessellations." *Monthly Notices of the Royal Astronomical Society* 342 (2): 345–54. doi:10.1046/j.1365-8711.2003.06541.x.

Cappellari, Michele. 2017. "Improving the Full Spectrum Fitting Method: Accurate Convolution with Gauss–Hermite Functions." *Monthly Notices of the Royal Astronomical Society*466 (1): 798–811. doi:10.1093/mnras/stw3020.

Cherepashchuk, A. M., V. L. Afanas'Ev, A. V. Zasov, and I. Yu. Katkov. 2010. "Kinematics of Disk Galaxies with Known Masses of Their Supermassive Black Holes. Observations." *Astronomy Reports* 54 (7): 578–89. doi:10.1134/s1063772910070024.

Díaz-García, S., H. Salo, E. Laurikainen, and M. Herrera-Endoqui. 2016. "Characterization of Galactic Bars from 3.6μm S4G Imaging." *Astronomy & Astrophysics* Volume 587, article id. 160, 40 pp. doi:10.1051/0004-6361/201526161.

Dullo, Bililign T., Mario Chamorro-Cazorla, Armando Gil De Paz, África Castillo-Morales, Jesús Gallego, Esperanza Carrasco, Jorge Iglesias-Páramo, et al. 2019. "High-Resolution MEGARA Integral-Field Unit Spectroscopy and Structural Analysis of a Fast-Rotating, Disky Bulge in NGC 7025." *The Astrophysical Journal* Volume 871, Issue 1, article id. 9, 12 pp. doi:10.3847/1538-4357/aaf424.

Event Horizon Telescope Collaboration et al. 2019. "First M87 Event Horizon Telescope Results. I. The Shadow of the Supermassive Black Hole." *The Astrophysical Journal Letters* Volume 875, Issue 1, article id. L1, 17 pp.

Fanidakis, N., C. M. Baugh, A. J. Benson, R. G. Bower, S. Cole, C. Done, and C. S. Frenk. 2011. "Grand Unification of AGN Activity in the ΛCDM Cosmology." *Monthly Notices of the Royal Astronomical Society*410 (1): 53–74. doi:10.1111/j.1365-2966.2010.17427.x.

Fathi, Kambiz, Glenn Van De Ven, Reynier Peletier, Eric Emsellem, Jesús Falcón–Barroso, Michele Cappellari, and Tim De Zeeuw. 2007. "Two-Dimensional Kinematics Of A Bar And Central Disk In Ngc5448." *ISLAND UNIVERSES Astrophysics and Space Science Proceedings*, 125–28. doi:10.1007/978-1-4020-5573-7_19.

Ferrarese, Laura, and Holland Ford. 2005. "Supermassive Black Holes in Galactic Nuclei: Past, Present and Future Research." *Space Science Reviews* 116: 3-4. doi:10.1007/s11214-005-3947-6.

Ferruit, Pierre, Andrew S. Wilson, and John S. Mulchaey. 1998. "Hubble Space TelescopeWFPC2 Imaging of the Seyfert Galaxy NGC 3516." *The Astrophysical Journal* 509 (2): 646–52. doi:10.1086/306536.

Heckman, Timothy M., and Philip N. Best. 2014. "The Coevolution of Galaxies and Supermassive Black Holes: Insights from Surveys of the Contemporary Universe." *Annual Review of Astronomy and Astrophysics*52 (1): 589–660. doi:10.1146/annurev-astro-081913-035722.

Holmes, L., K. Spekkens, S. F. Sánchez, C. J. Walcher, R. García-Benito, D. Mast, C. Cortijo-Ferrero, et al. 2015. "The Incidence of Bar-like Kinematic Flows in CALIFA Galaxies." *Monthly Notices of the Royal Astronomical Society* 451 (4): 4397–4411. doi:10.1093/mnras/stv1254.

Hubble Space Telescope. 2019. "Hubble's Instruments: WFC3 - Wide Field Camera 3." *Hubble Space Telescope*. ESA/Hubble. Accessed October 12. https://www.spacetelescope.org/about/general/instruments/wfc3/.

Iannuzzi, Francesca, and E. Athanassoula. 2015. "2D Kinematic Signatures of Boxy/Peanut Bulges." *Monthly Notices of the Royal Astronomical Society* 450 (3): 2514–38. doi:10.1093/mnras/stv764.

Kuzio De Naray, Rachel, Cameron A. Arsenault, Kristine Spekkens, J. A. Sellwood, Michael Mcdonald, Joshua D. Simon, and Peter Teuben. 2012. "Searching for Non-Axisymmetries in NGC 6503: a Weak End-on Bar." *Monthly Notices of the Royal Astronomical Society* 427 (3): 2523–36. doi:10.1111/j.1365-2966.2012.22126.x.

Lansbury, G. B., J. R. Lucey, and R. J. Smith. 2014. "Barred S0 Galaxies in the Coma Cluster." *Monthly Notices of the Royal Astronomical Society* 439 (2): 1749–64. doi:10.1093/mnras/stu049.

Laurikainen, E., H. Salo, E. Athanassoula, A. Bosma, and M. Herrera-Endoqui. 2014. "Milky Way Mass Galaxies with X-Shaped Bulges Are Not Rare in the Local Universe." *Monthly Notices of the Royal Astronomical Society: Letters* 444 (1). doi:10.1093/mnrasl/slu118.

Lewis, C, and K Spekkens. 2018. "Non-Parametric Decompositions of Disc Galaxies in S4G Using Diskfit." *Monthly Notices of the Royal Astronomical Society* 478 (4): 5689–5701. doi:10.1093/mnras/sty1836.

Li, Yan-Rong, Jian-Min Wang, Luis C. Ho, Kai-Xing Lu, Jie Qiu, Pu Du, Chen Hu, et al. 2016. "Spectroscopic Indication Of A Centi-Parsec Supermassive Black Hole Binary In The Galactic Center Of Ngc 5548." *The Astrophysical Journal* Volume 822, Issue 1, article id. 4, 21 pp. doi:10.3847/0004-637x/822/1/4.

Marel, Roeland P. Van Der, and Marijn Franx. 1993. "A New Method for the Identification of Non-Gaussian Line Profiles in Elliptical Galaxies." *The Astrophysical Journal* 407 (April): 525. doi:10.1086/172534.

Mundell, C. G., A. Pedlar, D. L. Shone, and A. Robinson. 1999. "Gas Dynamics in the Barred Seyfert Galaxy NGC 4151 -- II. High-Resolution HI Study." *Monthly Notices of the Royal Astronomical Society* 304 (3): 481–94. doi:10.1046/j.1365-8711.1999.02331.x.

"NASA/IPAC Extragalactic Database." 2020. NASA/IPAC. Accessed March 6. https://ned.ipac.caltech.edu/.

Onken, Christopher A., Monica Valluri, Jonathan S. Brown, Peter J. Mcgregor, Bradley M. Peterson, Misty C. Bentz, Laura Ferrarese, et al. 2014. "The Black Hole Mass Of Ngc 4151. Ii. Stellar Dynamical Measurement From Near-Infrared Integral Field Spectroscopy." *The Astrophysical Journal* Volume 791, Issue 1, article id. 37, 20 pp. doi:10.1088/0004-637x/791/1/37.

Pedlar, A., P. Howley, D. J. Axon, and S. W. Unger. 1992. "A Neutral Hydrogen Study of NGC 4151." *Monthly Notices of the Royal Astronomical Society* 259 (2): 369–80. doi:10.1093/mnras/259.2.369.

Peng, Chien. 2020. "Galfit Home Page." Accessed March 6. https://users.obs.carnegiescience.edu/peng/work/galfit/galfit.html.

Peters, Wesley, and Kuzio De Naray, Rachel. 2017. "Photometric and Kinematic DiskFit Models of Four Nearby Spiral Galaxies." *Monthly Notices of the Royal Astronomical Society* 469 (3): 3541–63. doi:10.1093/mnras/stx821.

Randriamampandry, T. H., F. Combes, C. Carignan, and N. Deg. 2015. "Estimating Non-Circular Motions in Barred Galaxies Using NumericalN-Body Simulations." *Monthly Notices of the Royal Astronomical Society* 454 (4): 3743–59. doi:10.1093/mnras/stv2147.

Randriamampandry, T. H., N. Deg, C. Carignan, F. Combes, and K. Spekkens. 2016. "Exploring the GalMer Database: Bar Properties and Non-Circular Motions." *Astronomy & Astrophysics* Volume 594, article id. 86, 10 pp. doi:10.1051/0004-6361/201629081.

Randriamampandry, T. H., N. Deg, C. Carignan, and L. M. Widrow. 2018. "Simulating Non-Axisymmetric Flows in Disk Galaxies." *Astronomy & Astrophysics* Volume 618, article id. 106, 16 pp. doi:10.1051/0004-6361/201833509.

Reese, A. S., T. B. Williams, J. A. Sellwood, Eric I. Barnes, and Brian A. Powell. 2007. "Photometric Decomposition of Barred Galaxies." *The Astronomical Journal* 133 (6): 2846–58. doi:10.1086/516826.

Reid, M. J., and A. Brunthaler. 2004. "The Proper Motion of Sagittarius A*. II. The Mass of Sagittarius A*." *The Astrophysical Journal* 616 (2): 872–84. doi:10.1086/424960.

Riffel, Rogemar A., Thaisa Storchi-Bergmann, Rogerio Riffel, Luis G. Dahmer-Hahn, Marlon R. Diniz, Astor J. Schönell, and Natacha Z. Dametto. 2017. "Gemini NIFS Survey of Feeding and Feedback Processes in Nearby Active Galaxies – I. Stellar Kinematics." *Monthly Notices of the Royal Astronomical Society* 470 (1): 992–1016. doi:10.1093/mnras/stx1308.

Schönell, Astor J, Thaisa Storchi-Bergmann, Rogemar A Riffel, Rogério Riffel, Marina Bianchin, Luis G Dahmer-Hahn, Marlon R Diniz, and Natacha Z Dametto. 2019. "Gemini NIFS Survey of Feeding and Feedback in Nearby Active Galaxies – III. Ionized versus Warm Molecular Gas Masses and Distributions." *Monthly Notices of the Royal Astronomical Society* 485 (2): 2054–70. doi:10.1093/mnras/stz523.

Sellwood, J. A., and Ricardo Zánmar Sánchez. 2010. "Quantifying Non-Circular Streaming Motions in Disc Galaxies." *Monthly Notices of the Royal Astronomical Society* 404 (4): 1733–44. doi:10.1111/j.1365-2966.2010.16430.x.

Spekkens, Kristine, and J. A. Sellwood. 2007. "Modeling Noncircular Motions in Disk Galaxies: Application to NGC 2976." *The Astrophysical Journal* 664 (1): 204–14. doi:10.1086/518471.

Vaucouleurs, G. De. 1963. "Revised Classification of 1500 Bright Galaxies." *The Astrophysical Journal Supplement Series* vol. 8, p.31 doi:10.1086/190084.

"WIYN IFUs / HexPak & GradPak." 2019. *Matthew A. Bershady, WIYN Instrumentation / HexPak and GradPak IFUs*. University of Wisconsin. Accessed September 12. http://www.astro.wisc.edu/~mab/research/hexpak_gradpak/.

Appendix

Table of Abbreviations

Abbreviation	Definition
SMBH	Supermassive Black Hole
AGN	Active Galactic Nuclei
IFS	Integral Field Spectroscopy
IFU	Integral Field Unit
V	Recessional Velocity
σ	Velocity Dispersion
h_3	Third Gauss-Hermite moment: asymmetric skew
h_4	Fourth Gauss-Hermite moment: symmetric skew
M_{BH}	Supermassive Black Hole mass
σ_*	Bulge Stellar Velocity Dispersion
M_{BH}-σ_*	Relationship between supermassive black hole mass and bulge stellar velocity dispersion
V-h_3	Anti-correlation between recessional velocity and the third Gauss-Hermite moment in 2D kinematics
K-D	*DiskFit* Kinematic Disk only Model
K-D-B	*DiskFit* Kinematic Disk and Bar Model
K-D-RF	*DiskFit* Kinematic Disk and Radial Flow Model
K-D-B-RF	*DiskFit* Kinematic Disk, Bar, and Radial Flow Model
K-wD	*DiskFit* Kinematic Warped Disk Model
P-D	*DiskFit* Photometric Disk only Model
P-D-B	*DiskFit* Photometric Disk and Bar Model
P-D-Blg	*DiskFit* Photometric Disk and Bulge Model
P-D-B-Blg	*DiskFit* Photometric Disk, Bar, and Bulge Model
Ba17a	Batiste et al. February 2017
Ba17b	Batiste et al. March 2017
Be09	Bentz et al. 2009
R17	Riffel et al. 2017

Table A1: Abbreviations used throughout this paper.

Galfit Morphological Decomposition of the Sample from Literature

Galaxy	Component	Magnitude	R_e (arcsec)	n	e
NGC 3516	PSF	15.2	...	...	...
	Inner Bulge	13.4	2.01	1.24	0.23
	Bulge	13	9.22	0.96	0.4
	Disk	14.4	22.99	1	0.48
NGC 4151	PSF	14.5	...	...	...
	Inner Bulge	14.4	0.98	4.29	0.46
	Inner Bulge	14	1.96	0.71	0.04
	Bulge	12	10.22	0.81	0.05
	Disk	13	52.8	1	0.31
NGC 5548	PSF	16.7	...	...	...
	Inner Bulge	14.7	3.25	4.36	0.86
	Bulge	13.8	8.12	1.39	0.9
	Disk	15.6	31.71	1	0.85

Table A2: Values obtained from Table 4 of Bentz et al. (2009) using *Galfit* to model NGC 3516, NGC 4151, and NGC 5548, photometrically. The variable, *n*, represents the Sérsic light profile, and *e* denotes the eccentricity of each component, calculated by $e = 1 – b/a$ (Bentz et al. 2009).

DiskFit Example Kinematic Input File

```
NGC 3516, Kinematic input, with text format velocity field
vels                                                              # 2 vels/phot switch
F  F                                          # 3 VELS: I/O toggles: FITS I/O, vels in m/s
'NGC3516/KIN/NGC3516_good_vel.txt'                        # 4 file name with input data
None                                              # 5 VELS + FITS:file name for velocity uncerts
None                                        # 6 FITS region to fit: (xlow,ylow) & (xrange,yrange)
None                                  # 7 FITS sampling: regrad, regpa, regeps, istepout, pixscale
'NGC3516/KIN/IN_PROG/NGC3516_Output228.out'              # 8 file name for output parameters
T T F                                              #9 Disk toggles: fit for PA, eps & cen
227.03  .48                                   #10 initial guess for disk PA and eps=(1-b/a)
0.17 -0.97                                                #11 initial guess for disk center
T T 104.05 1                 #12 VELS: non-circ. flow + flow PA fit toggle, initial flow PA, order m
T T                                   #13 VELS: inner interpolation + radial flows fit toggles
T 2648.966 10 50           #14 VELS: toggle to fit Vsys, initial guess Vsys, delta_ISM, & vely errtol
T T T T 2.57 0.08 8.47   #15 VELS: warp toggles - warp, fit radius, ellip & pa, initial rw, welm & wphim
0                          #16 Seeing/beam smearing: If non-zero, seeing/beam FWHM for correction.
-0.001 -0.001                              #17 Model component smoothing lambda_1 & lambda_2
T 2 1000 1                                 #18 Uncertainties: toggle, seed, nunc, junc
F                                                    #19 Verbose toggle
0 17.42                                    #20 Min, max radii for bar/noncirc flow fit
1.33                                                          #21 Ring radii
2.57
7.10
10.52
13.96
17.42
```

Figure A1: Example *DiskFit* input file for the best-fit (K-D-B-RF) kinematic model for NGC 3516. The structure and requirements for each parameter in the input file are found in the *DiskFit* documentation.[6]

___

[6] https://www.physics.queensu.ca/Astro/people/Kristine_Spekkens/diskfit/1_2_2/DiskFit122.pdf.

DiskFit Example Kinematic Output File

Minimization output, vels
Input files:
ngc3516/kin/ngc3516.inp
NGC3516/KIN/NGC3516_good_vel.txt

Output model and (data-model) residuals files:
NGC3516/KIN/IN_PROG/NGC3516_Output189.mod

Disk toggles: PA: T   eps: T   center: T non-axi: T   phib: T
vels toggles: interp0: T radial: T   Vsys: T   warp: F   rw: F   welm: F wphim: F

Input values
disk PA, phi_d^prime (deg):   227.03
disk eps: 0.48
x,y center (data units):   0.17   -0.97
Non-axisymm phib (deg):   104.05
Harmonic order m: 1
Vsys (km/s):   2648.97
Delta_ISM (km/s):   10.00

No seeing correction applied
No model component smoothing applied
Uncertainties estimated via bootstrap: seed: 2 nunc: 1000 junc: 1.00

Best-fitting values
disk PA, phi_d^prime (deg):   237.03 +/- 3.27
disk eps: 0.21 +/- 0.02
disk incl (deg):   37.54 +/- 1.69
Non-axisymm phib (disk plane, deg):   77.07 +/- 7.24, 310.89, 226.72
Vsys (km/s):   2673.72 +/- 11.55

Minimization Details
points Dn used in fit: 60
iterations in minimization: 11
Minimum chi^2 found: 0.412983
Degrees of freedom in fit: 30

Fitted velocity components   (radii in data units, velocities in km/s):

r	npts	Vt	eVt	Vr	eVr	Vm,t	eVm,t	Vm,r	eVm,r
1.33	5.12	108.92	10.94	-49.46	10.82	261.99	169.66	142.83	161.00
2.57	10.86	184.39	10.61	-55.14	10.40	24.51	93.03	38.48	101.15
7.10	9.12	141.00	8.51	-5.43	10.21	159.80	133.77	102.30	133.88
10.52	13.92	227.94	8.66	-20.87	13.50	25.36	99.38	56.48	101.48
13.96	15.08	173.97	9.29	-47.80	12.66	284.27	170.15	218.21	170.43
17.42	4.92	220.13	17.68	-58.71	22.82	241.75	186.38	150.82	158.50

Figure A2: Example *DiskFit* output file for the best-fit (K-D-B-RF) kinematic model for NGC 3516. The structure and requirements for each parameter in the input file are found in the *DiskFit* documentation.[7]

---

[7] https://www.physics.queensu.ca/Astro/people/Kristine_Spekkens/diskfit/1_2_2/DiskFit122.pdf.

Figure A3: Smooth kinematic plots for NGC 3516 using *Vorbin* (Cappellari & Copin 2003). In each of the plots, the solid black line denotes the position angle of the disk component, in the sky plane. The dashed red and blue lines represent the position angles of the tangential and radial non-axisymmetric flow forces (or bar) respectively, also in the sky plane. The dots represent the positions of the center of each HexPak fiber. The top row from left to right shows: the observed velocity field data from NGC 3516 smoothed; the best-fit (K-D-B-RF) kinematic model; the best-fit model with the best-fit systemic recessional velocity subtracted from each point. The middle row from left to right shows: the tangential velocity from the disk component only; the tangential velocity of the bar component; the radial velocity of the bar component. The bottom row from left to right shows: the radial velocity componentl the residual image, the model subtracted from the input velocity field.

Figure A4: Smooth kinematic plots for NGC 4151 using *Vorbin* (Cappellari & Copin 2003). Refer to Figure A3 for figure desctiption.

Smoothed *Vorbin* plots for NGC 5548 Kinematics
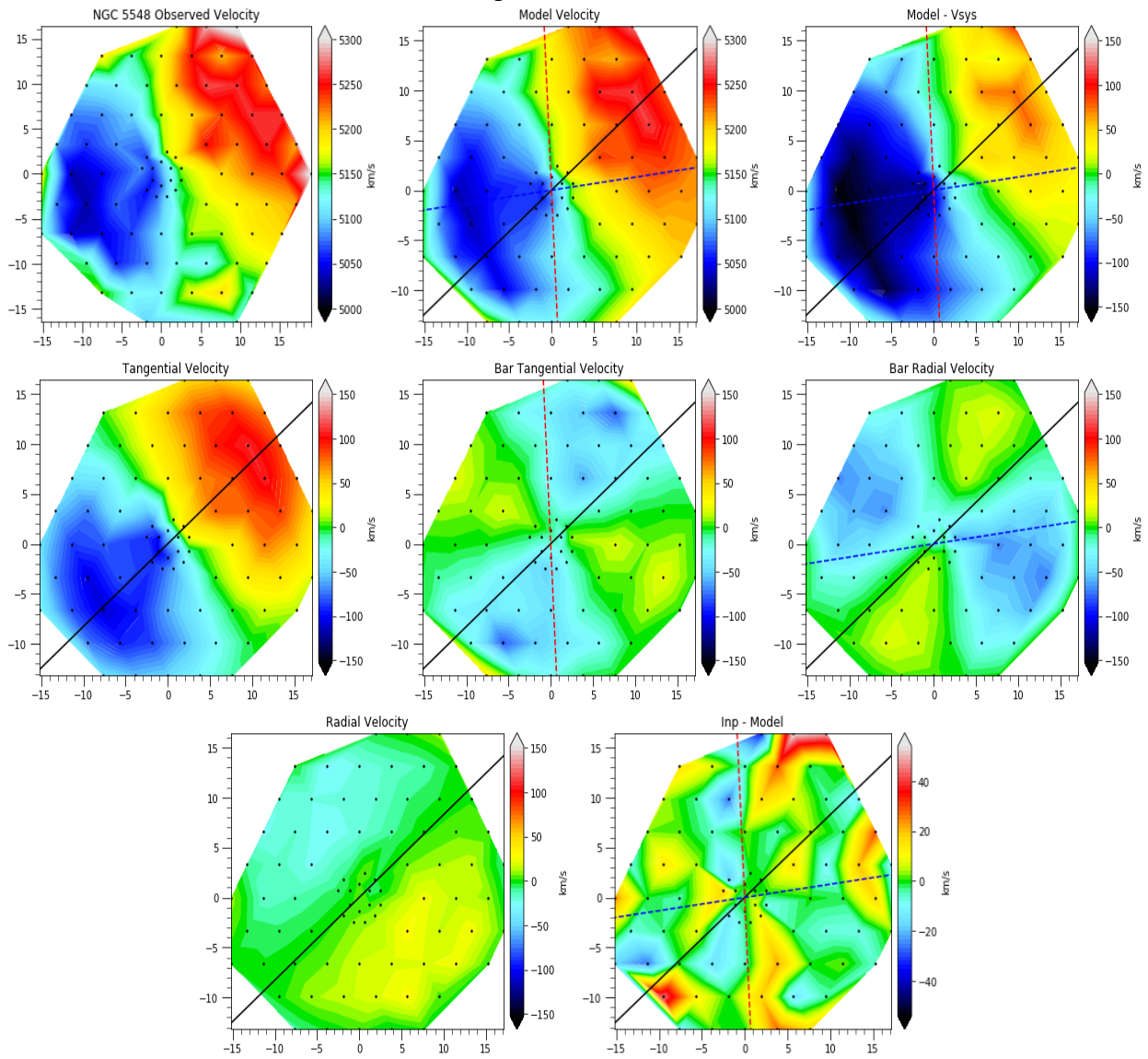
Figure A5: Smooth kinematic plots for NGC 5548 using *Vorbin* (Cappellari & Copin 2003). Refer to Figure A3 for figure desctiption.

Galfit Models of the Sample from Literature
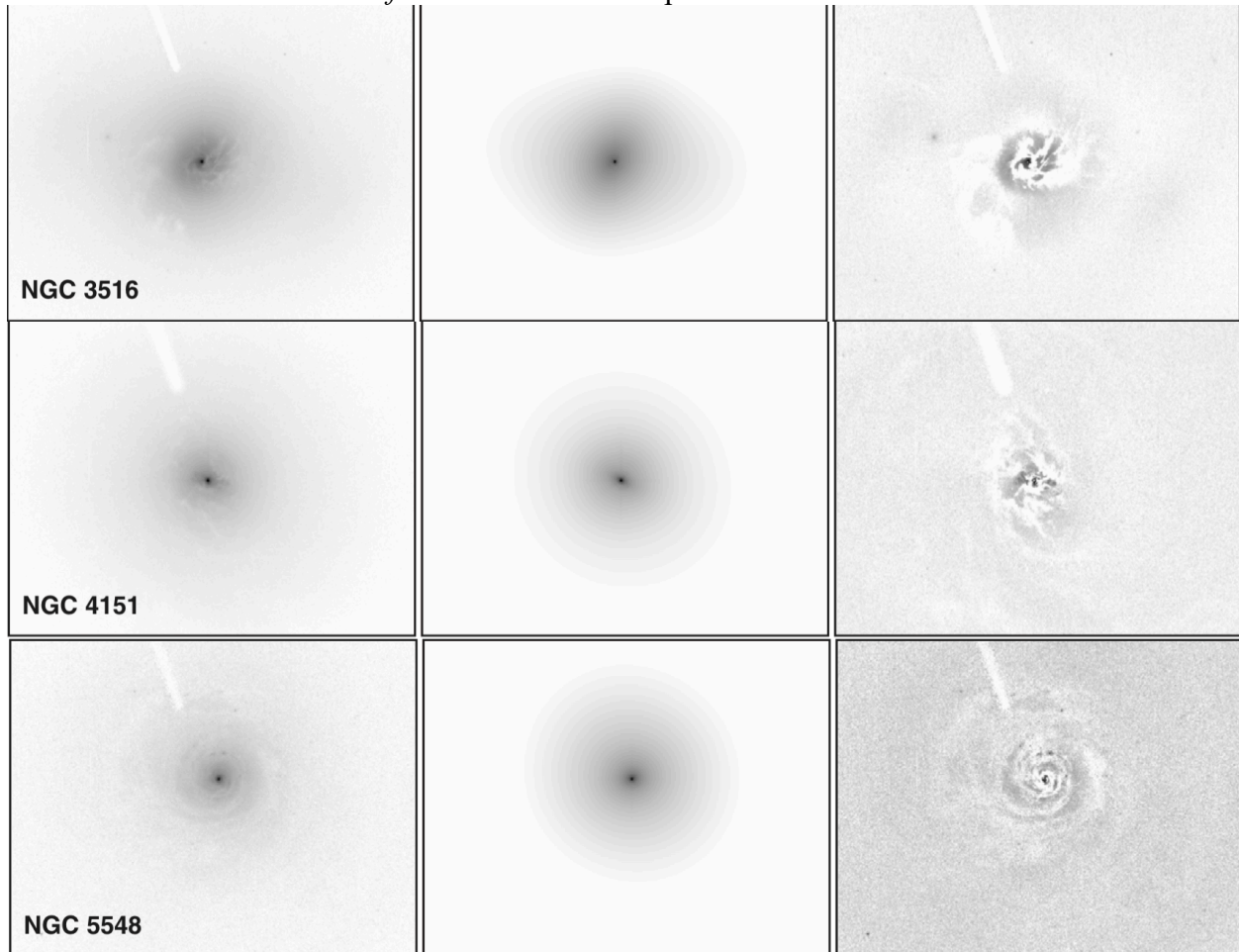
Figure A6: Images obtained from Figure 3 of Bentz et al. (2009) using *Galfit* to model NGC 3516, NGC 4151, and NGC 5548. Each row from top to bottom is dedicated to NGC 3516, NGC 4151, and NGC 5548 respectively. Each row from left to right shows: the HST image of the galaxy; the produced *Galfit* model; the residuals of the model subtracted from the input. See Table A2 for parameters associated with each galaxy presented.

NGC 3516 Kinematic *DiskFit* Results from Literature
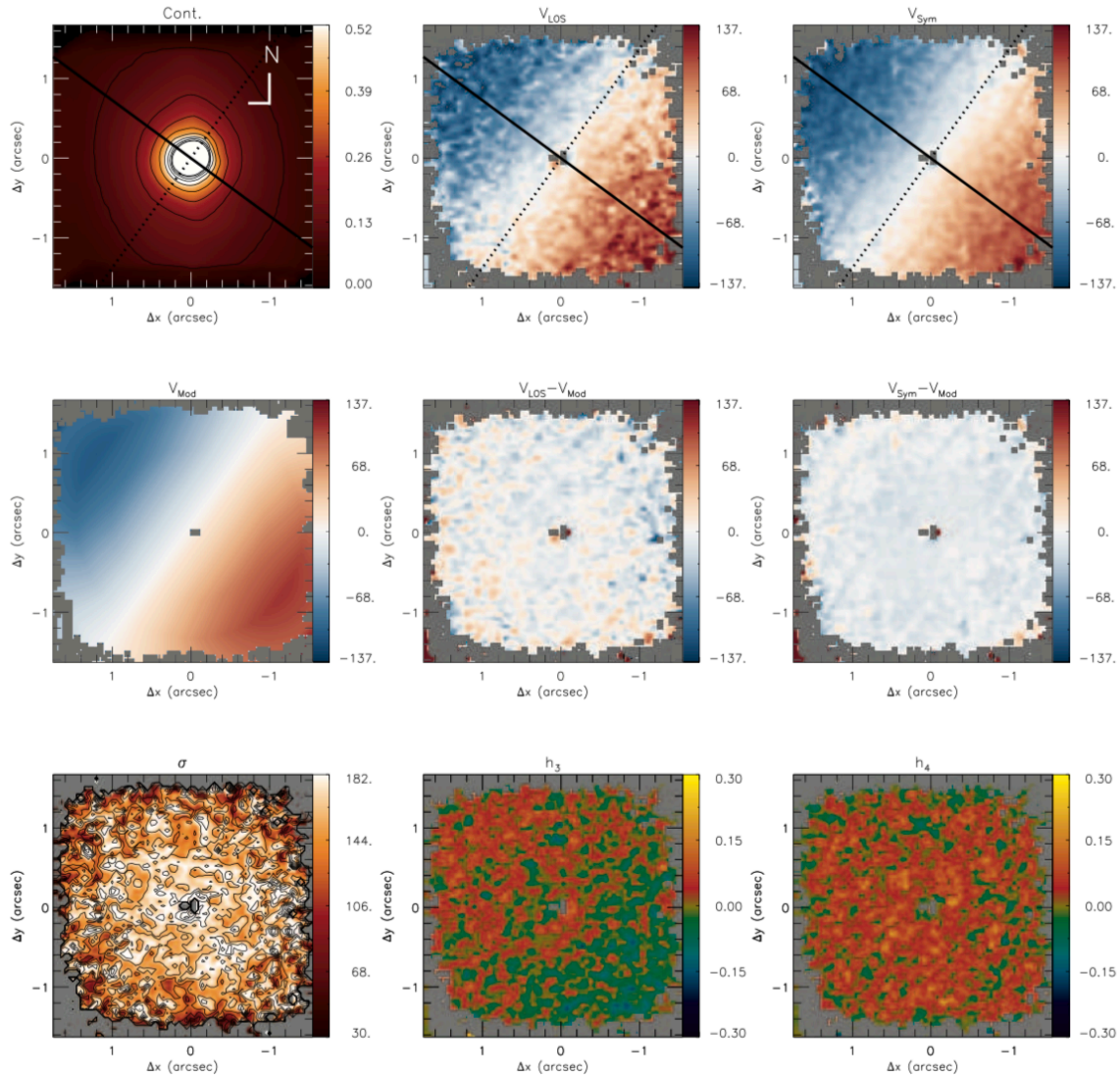
Figure A7: Inner 3" x 3" plots of NGC 3516 obtained from Figure 5 of Riffel et al. (2017). The top row from left to right shows: the image of NGC 3516 in the K-band; velocity field of the line of sight; symmetrized line of sight velocity field. The middle row from left to right shows: the output *DiskFit* model from inputting the symmetrized velocity field; the residuals between the original velocity field and the model; the residuals between the symmetrized velocity field and the model. The bottom row from left to right shows the second (velocity dispersion), third, and fourth Gauss-Hermite moments respectively.

NGC 5548 Kinematic *DiskFit* Results from Literature
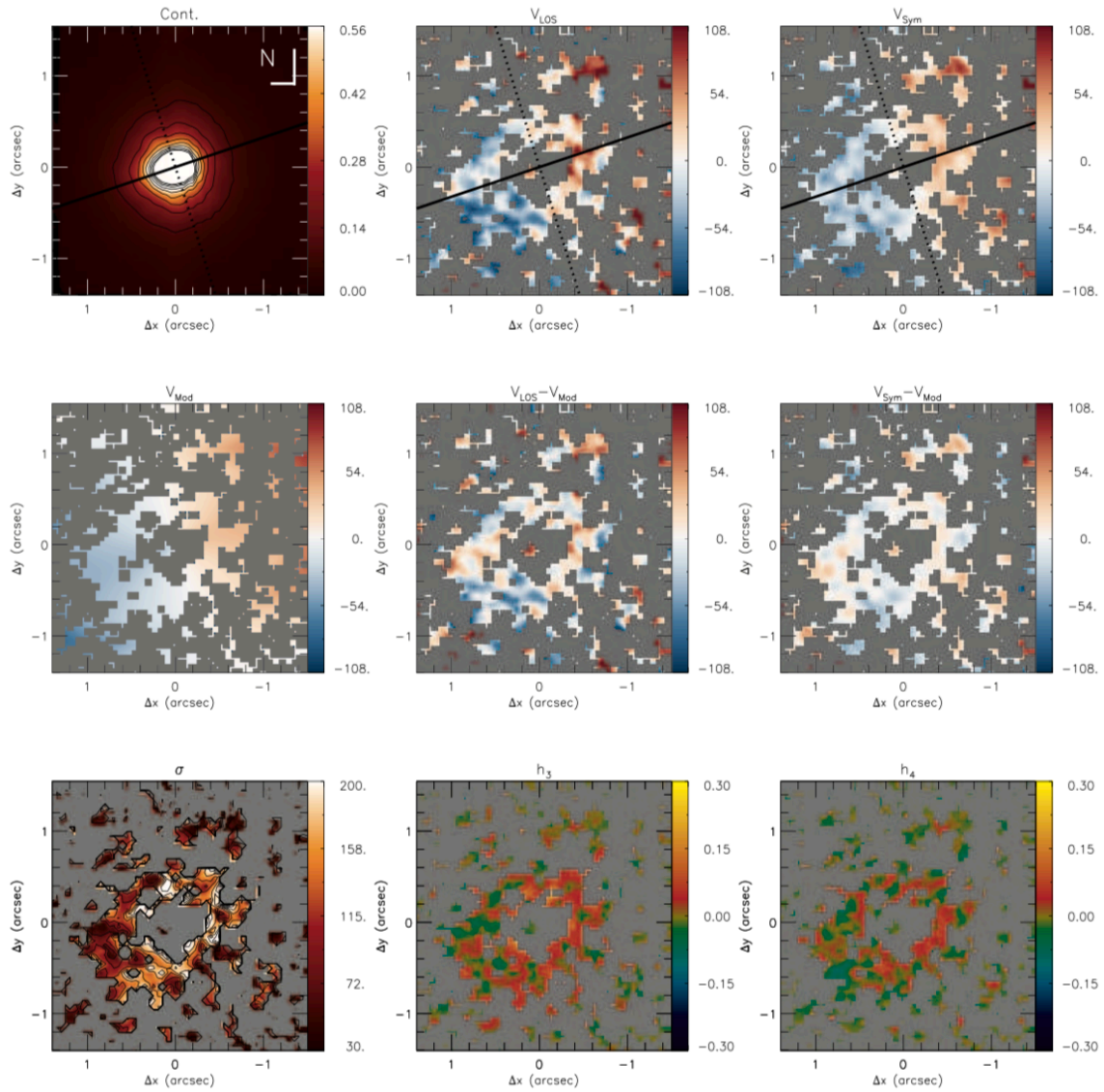
Figure A8: Inner 3" x 3" plots of NGC 5548 obtained from Figure 9 of Riffel et al. (2017). Refer to Figure A7 for figure desctiption.

Inner 3" x 3" Rotation Curves for NGC 3516 and NGC 5548 from Literature
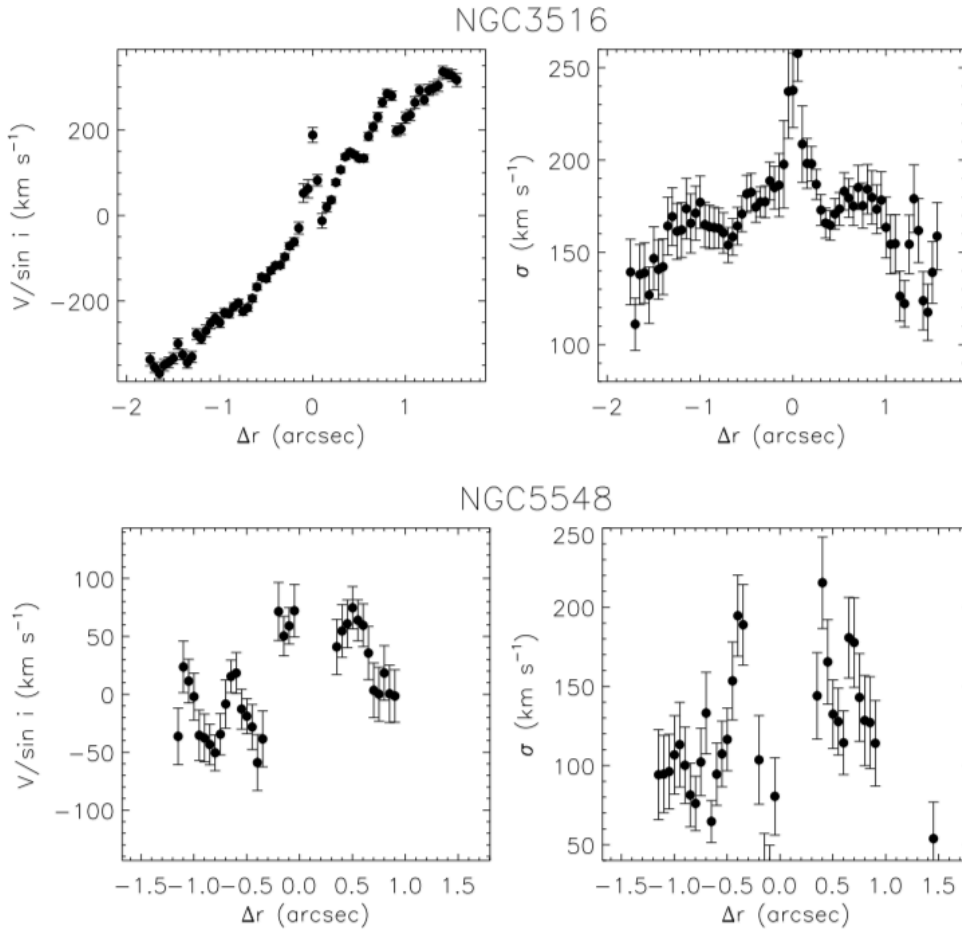
Figure A9: Figures obtained from Figure B1 of Riffel et al. (2017). The top row, for NGC 3516, from left to right shows: the full velocity rotation curve for the inner 3"; the velocity dispersion radial curve. The bottom row is the same as the top row for NGC 5548. Velocity rotation curves from one-dimensional cuts along the major axis of the observed velocity field and velocity dispersion curves come from the velocity dispersion along the same axis. Major axis for these galaxies can be seen in Figure A7 and Figure A8 for NGC 3516 and NGC 5548 respectively.

Figure A10: Rotation curve for the inner 50" of NGC 3516 obtained from Figure 7 of Cherepashchuk et al. (2010). The dots represent the velocity found at each point from while the error bars account for the expected velocity of the non-axisymmetric flow forces.

NGC 4151 Rotation Curve from Literature
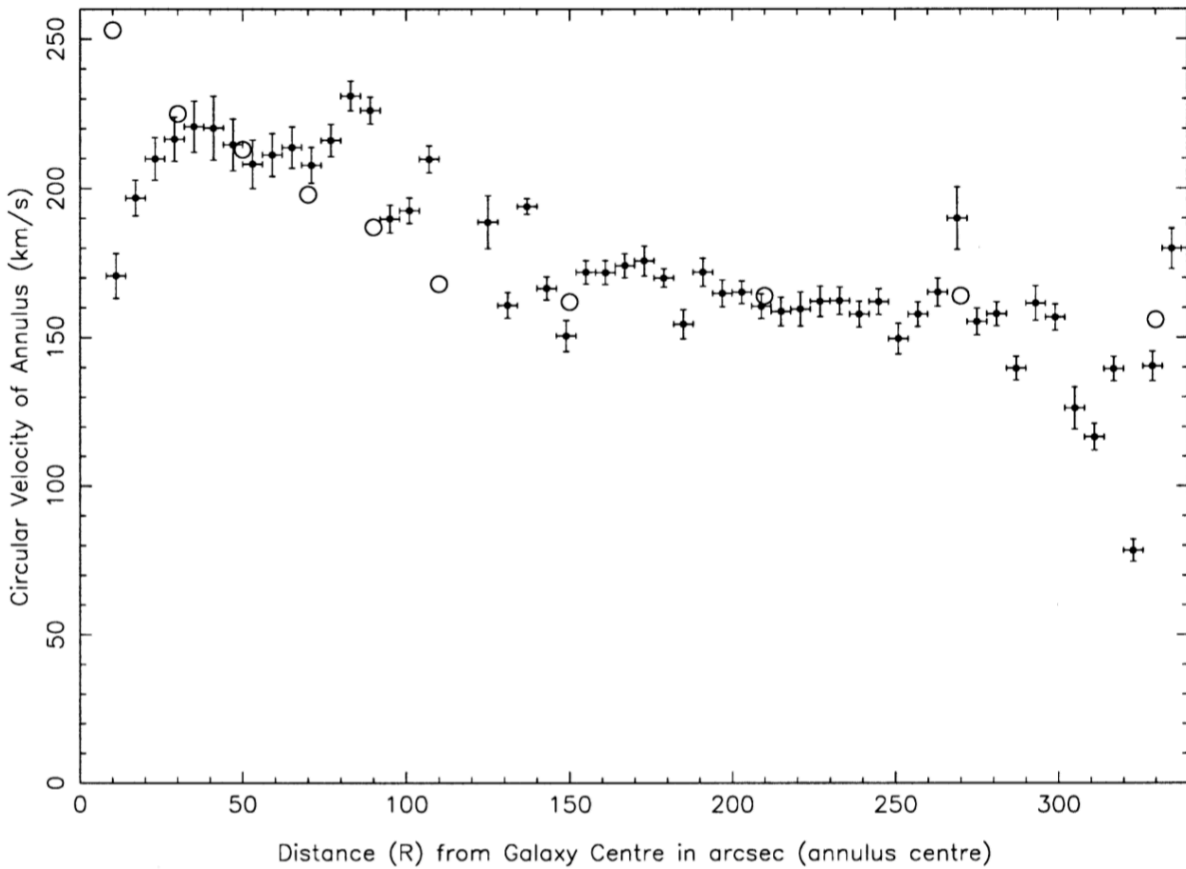
Figure A11: Rotation curve for the inner 340" of NGC 4151 obtained from Figure 8(a) of Mundell et al. (1999). The solid dots with error bars represent the velocity found at each point, while the open circles represent the rotation curve obtained from Pedlar et al. (1992).

Kinematic Signatures of Face-on Boxy/Peanut Bulges from Literature
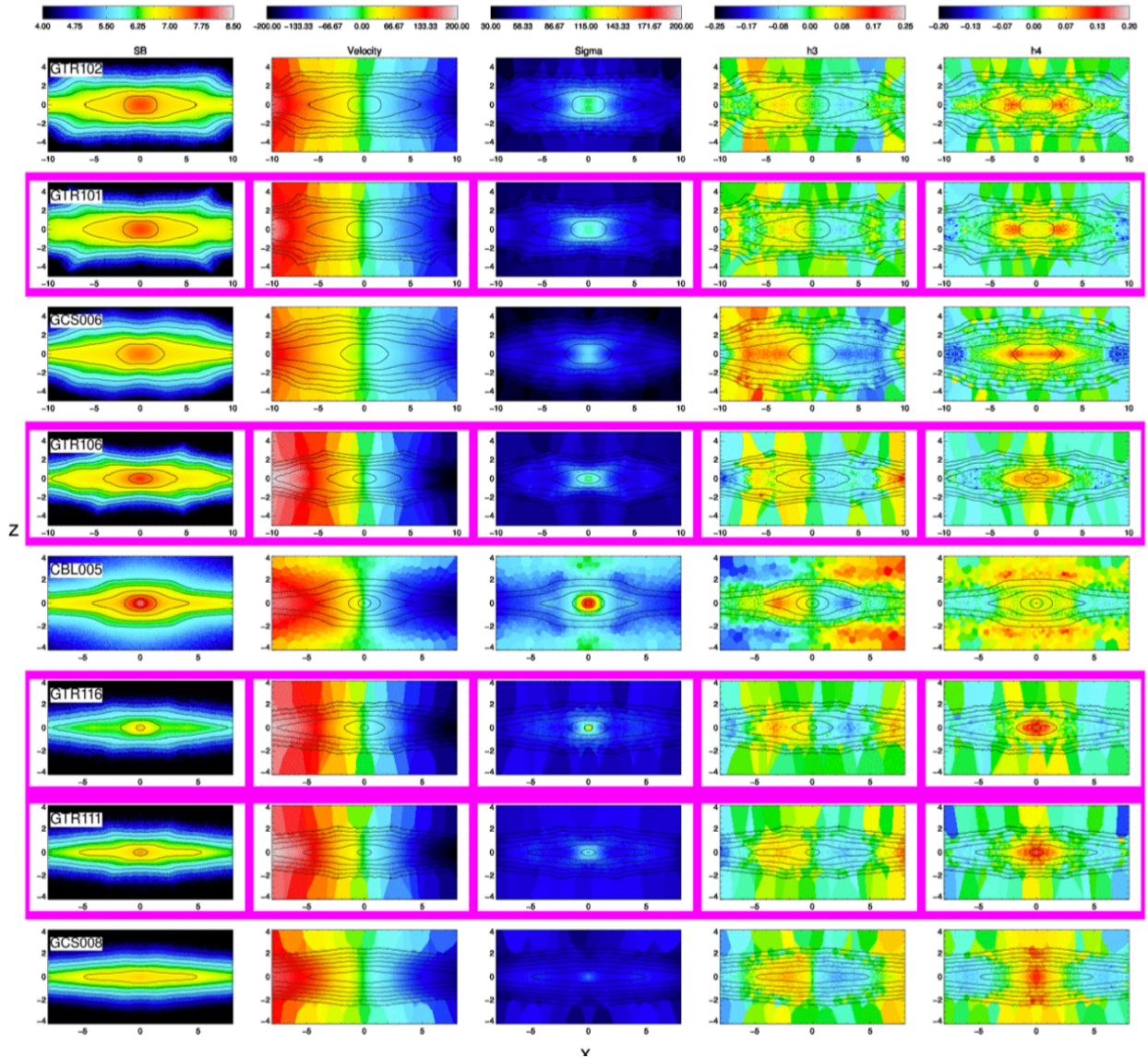
Figure A12: Images obtained from Figure 10 of Iannuzzi & Athanassoula (2015) simulating the kinematic side-on signature of a boxy/peanut bulge viewed in a face-on (disk inclinition i_{disk} = 0°) viewed from a side-on angle (where the long-edge of the boxy/peanut bulge can be viewed). The strength of the boxy/peanut bulge decreases with each row downwards, with the strongest component at the top. From left to right the columns show maps of: surface brightness; velocity; velocity dispersion; the third Gauss-Hermite moment h_3; the fourth Gauss-Hermite moment h_4.
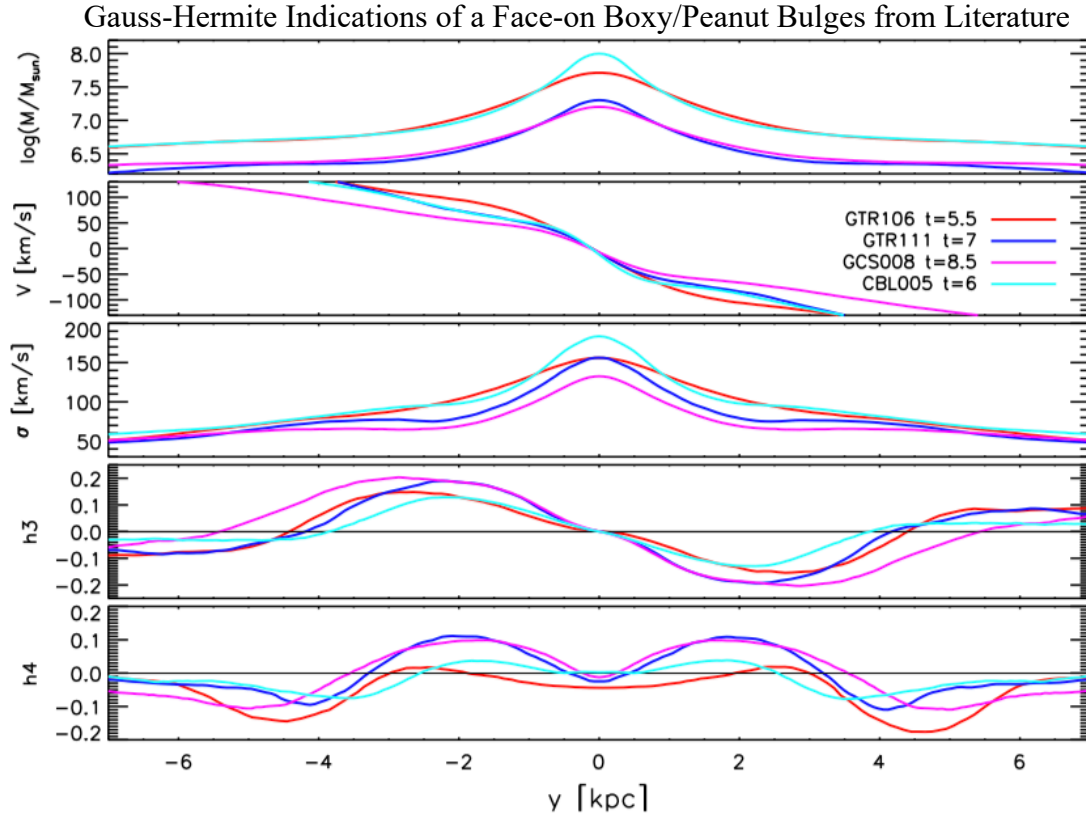
Figure A13: Images obtained from Figure 18 of Iannuzzi & Athanassoula (2015) simulating the kinematic end-on signature of a boxy/peanut bulge viewed in a face-on (disk inclinition $i_{disk} = 0°$) orientation. Each of the colored lines represents a different simulation of galaxy kinematics containing a boxy/peanut bulge. The panels from top to bottom show a function of the galaxy magnitude then the first four Gauss-Hermite moments in order.